Locomotion et écoulement dans les fluides complexes confinés

Levan Jibuti

UNIVERSITÉ DE GRENOBLE

THÈSE

Pour obtenir le grade de

DOCTEUR DE L'UNIVERSITÉ DE GRENOBLE

Spécialité : **Physique des sciences du vivant**

Arrêté ministérial : 7 Août 2006

Présentée par

Levan Jibuti

Thèse dirigée par **Philippe Peyla**
et codirigée par **Salima Rafaï**

préparée au sein du **Laboratoire interdisciplinaire de Physique**
dans **Ecole Doctorale de Physique**

Locomotion et écoulements dans les fluides complexes confinés

Thèse soutenue publiquement le **21 Octobre 2011**,
devant le jury composé de :

M. Emmanuel Maitre
Maître de Conférences, Université Joseph Fourier, Président
M. Christian Wagner
Professeur, Université de Saarbruck, Allemagne, Rapporteur
M. Walter Zimmermann
Professeur, Université de Bayreuth, Allemagne, Rapporteur
M. Philippe Peyla
Professeur, Université Joseph Fourier, Directeur de thèse
Melle Salima Rafaï
Chargé de Recherche, CNRS, Co-Directeur de thèse
Melle Astrid Decoene
Maître de Conférences, Université de Paris Sud XI, Invitée

Locomotion and Flow in Complex and Confined Fluids

Levan Jibuti

PhD Thesis

Grenoble, October 21^{th} 2011

PhD Thesis supervised by Prof. Philippe Peyla and Dr Salima Rafaï
prepared at Laboratoire Interdisciplinaire de Physique
Université Joseph Fourier - CNRS
Grenoble, France

Contents

List of Figures

Abstract

This work is dedicated to the study of dynamics and rheology of the complex fluids. We use three dimensional numerical simulations. The systems we study here are: suspensions of biological active micro-swimmers, suspensions of rigid spherical particles in presence of an external field and the dynamics of sheared confined spherical particles.

Micro-swimmers are the microscopic objects that propel themselves through a fluid and they are ubiquitous in nature. A common example of micro-swimmers is the *Chlamydomonas*. One of the main goal of this thesis is to understand the effect of self-motility of these micro-organisms on the global macroscopic properties of the fluid, such as the effective viscosity to explain experimental observations. We elaborated different models for *Chlamydomonas* suspensions and conducted numerical simulations using the 3D version of the Fluid Particle Dynamics method (explained in this thesis). The results of our numerical simulations has been shown and discussed in light of the experimental observations. One of the proposed models incorporates all experimentally observed phenomena and is extendable for other types of micro-swimmer suspensions.

This thesis is also dealing with the effects of confinement on the dynamics of sheared spherical particles. We found that in confined geometry, angular velocity of sheared particles decreases compared to the one imposed by the shear flow. The angular velocity of the particles decreases also when the particle are close to a single wall and the translational velocity of the particles changes so that the difference between velocity of the particle and the velocity of the wall decreases.

Another objective of this work is to study suspensions with tunable effective viscosity. We conducted a numerical investigation of sheared spherical particle suspensions in presence of an external torque. We showed that the change of particle angular velocity with an external torque is sufficient to strongly change the effective viscosity of the suspension. Based on numerical simulations, a semi-empirical formula has been proposed for the effective viscosity of spherical particles suspensions valid up to 40% concentration. We also showed that a modified second Faxén law can be equivalently established for large concentrations.

Résumé

Cette thèse est consacrée à l'étude de la dynamique et de la rhéologie des fluides complexes. Nous utilisons une méthode de simulation numérique à trois dimensions. Les systèmes que nous étudions ici sont des suspensions de micro-nageurs actifs, des suspensions de particules sphériques rigides en présence d'un champ externe auquel elles sont sensibles et de la dynamique de suspensions de particules sphériques et confinées en cisaillement.

Les Micro-nageurs sont les objets microscopiques qui se propulsent dans un fluide et ils sont omniprésents dans la nature. Un exemple commun de micro-nageurs est la micro-algue *Chlamydomonas*. Un des buts principaux de cette thèse est de comprendre l'effet de la motilité de ces micro-organismes sur les propriétés macroscopiques globales de la suspension, telles que la viscosité effective pour expliquer les observations expérimentales. Nous avons élaboré différents modèles de suspensions de *Chlamydomonas* et effectué des simulations numériques utilisant la version 3D de la dynamique des particules fluides (FPD) (méthode expliquée dans cette thèse). Les résultats de nos simulations numériques ont été présentés et discutés à la lumière des observations expérimentales. Un des modèles proposés intègre tous les phénomènes observés expérimentalement et sont applicables à d'autres types de suspensions de micro-nageurs.

Cette thèse consacre également un chapitre sur les effets du confinement sur la dynamique de cisaillement des suspensions diluées de particules sphériques. Nous avons constaté que dans la géométrie confinée, la vitesse angulaire des particules diminue par rapport à celle imposée par l'écoulement de cisaillement. La vitesse angulaire des particules diminue également lorsque la particule est proche d'une paroi unique et la vitesse de translation de la particule par rapport à la vitesse de la paroi diminue.

Un autre objectif de cette thèse est d'étudier les suspensions à viscosité effective ajustable. Nous avons mené une étude numérique sur des suspensions de particules sphériques en présence d'un couple externe. Nous avons montré que le changement de vitesse angulaire des particules due à l'application d'un couple externe est suffisante pour modifier fortement la viscosité de la suspension. Basée sur des simulations numériques, une formule semi-empirique a été proposée pour la viscosité des suspensions de particules sphériques valables jusqu'à 40% de concentration. Nous avons également montré que la 2ème loi de Faxén peut être étendue par une expression empirique pour de grandes concentrations.

Chapter 1

Introduction

1.1 Background

Complex fluids are common and can be found almost everywhere in our life. Complex fluids include: emulsions, suspensions, biofluids, gels, foams, polymers, solutions, liquid crystals, colloidal crystals etc. Typical examples of complex fluids are: blood, cosmetic or pharmaceutical creams, foods (milk, yogurt, chocolate, mayonnaise etc). Usually complex fluids are also non-Newtonian fluids which means they do not obey the (Newtonian) linear relationship between applied stress (σ) and ($\dot{\gamma}$) shear rate. Non-Newtonian fluids reveal diverse and interesting behavior which is applicable both in science and technology. One of the most important aim of studying the complex fluids is to understand the mechanism (forces and interactions) acting on an intermediate length scale which defines the fluid behavior. This would give an opportunity to design and control new material with the desired properties. Such materials can be useful in engineering (automobiles) or in medicine for example.

Complex fluids are substances with an intermediate length scale which plays a key role in determining the properties of the substances. An intermediate length scales existing between molecular and macroscopic length scales can be represented by organized atoms and molecules forming larger structures, colloids, microscopic rigid particles or even alive micro-organisms [1]. The science which establishes relationships between properties of the fluid and its structure at intermediate length scale is the rheology. More generally the rheology is the study of deformation and flow of matter in response

of an applied stress. The common rheological properties which are used to characterize the non-Newtonian fluids include: effective viscosity (shear viscosity η_{eff}, vortex viscosity η^R_{eff}); stress σ (shear stress, normal stress, normal stress difference); relaxation time τ; viscoelastic modulus etc.

The non-Newtonian fluids can reveal shear thinning or shear thickening behavior or/and viscoelastic effects (for example the Weissenberg effect [2]). The shear thinning is the tendency of a fluid to reduce its viscosity when the applied shear rate increases [3]. The shear thickening behavior is observed when the viscosity of the fluid increases with the shear rate [4, 5].

Complex fluids can be studied using analytical approaches, numerical simulations or experiments. In this work, we use numerical simulations and compare our results to experimental observations and analytical approaches.

1.2 Research objectives

In this thesis, we analyze properties (such as effective viscosity) of suspensions with active particles. These active particles can be natural micro-swimmers, but also field-sensitive particles or confined particles. Their activity (swimming, rotation) have a consequence on the macroscopic properties of the suspensions: it changes its effective viscosity. A link between micro and macro properties of the fluid is established.

In recent years there has been considerable interest in the physics of swimming microorganisms. Such micro-swimmers are widespread in nature. For example: bacteria and spermatozoa in biofluids, micro-algae etc. The physics of these micro-organisms is interesting both: at microscopic length scales as individual swimmers [6] and at a larger length scales as component parts of complex systems (or "active fluids"). Despite the fact that micro-swimmers are simple organisms, the way they move through the fluid is more complicated than the way we swim. Since at the length scale where they live ($Re \ll 1$, where Re denotes the Reynold's number) inertia is negligible and micro-swimmers need to deform or propel themselves in a (non-reciprocal) way which is not invariant under time reversal symmetry [7, 8]. Besides the particularities of such swimming mechanism a fluid containing a large number of those organisms drastically changes its rheological properties. For example micro-swimmers change the fluids viscosity of the suspension

to which they belong [9, 10].

One of the main objectives of this thesis is a numerical modelization of the micro-swimmer suspensions (namely suspensions of *Chlamydomonas*) to establish a relationship between mechanisms of individual cells motion and the macroscopic properties of the fluid like the effective viscosity. Consistently with the experiments performed in our team, *Chlamydomonas reinhardtii* has been chosen as a model system in order to understand the effect of their motility on the global macroscopic parameters of the suspension.

The next aim of the thesis is to study more fundamental issues of fluid mechanics at small Reynolds numbers, like influence of finite geometry on the dynamics of rigid particles in the shear (Couette) flow. Despite that in many microfluidic devices or capillaries in biological systems, the size of suspended objects are comparable with one or more dimensions of the channels, there are small number of works dealing with the effects of confinement on flow fields and mechanics of confined suspended objects.

Another objective of the present work is the numerical investigation of suspensions with a tunable effective viscosity. In electro rheological (ER) fluids for example where particles are sensitive to an electrical field one can modify the rotation of the particles using the external field. As a result, viscosity of suspensions can be adjusted. Such fluids with controllable viscosity has technological applications in many kinds of industrial devices such as active dampers, clutches or brakes [11, 12]. For example, depending on road conditions, viscosity of the damping fluid needs to be adjusted in automobile dampers [13]. The contribution of an external torque to the effective viscosity of suspensions was theoretically studied in dilute regime by Brenner in 1970 [14]. Our goal in this work is to investigate this contribution on a wider range of concentrations and to establish relationship between the applied torque and the rheological properties of these suspensions.

1.3 Thesis outline

The present work is organized as follow.

Chapter 3 is dedicated to the numerical method, The Fluid Particle Dynamics (FPD). The main idea of the method as well as its positive and negative aspects

are described. The theory behind the FPD method and some details of numerical discretization techniques are introduced. New contributions, number of changes and possible extensions made in the FPD method are listed. Since the FPD method is relatively new in order to verify and illustrate it, we present some problems solved using the FPD method in comparison to well-known analytical results. Among them are: Stokes flow past sphere; a spherical particle in the shear flow; collision between two spheres and Jeffery's orbit for ellipsoidal particles in a shear flow. Afterwards, everywhere is this work the FPD method is used to solve several different problems.

Chapter 4 describes the effects of confinement on the dynamics of a single spherical particle in a shear flow. Two major effects are considered: decrease of the rotational velocity of the sphere in the shear flow due to particle-wall interactions and change of the translational velocity of the sheared particle in vicinity of the wall. Flow field are shown and result are compared with previous numerical and analytical predictions.

Chapter 5 numerically investigates the contribution of an external torque applied to a field-sensitive particle suspensions to the effective viscosity. The relationship between the torque applied to each particle and the effective viscosity of the fluid is established beyond the dilute regime and the semi-empirical formula is derived for the effective viscosity. Also an empirical second Faxén law is established and is valid up to 40% concentration.

Chapter 6 is dealing with the models and numerical simulations of *Chlamydomonas* micro-swimmer suspensions. After some general review of micro-swimmers and their specific low Reynolds number constrains, the main experimental observations of green algae suspension are summarized. Then several different models are considered in order to figure out the effects of motility of micro-swimmers into the global rheological properties of the fluid. The last section of chapter 6 describes the model which converges in anisotropic distribution of force dipoles by taking into account the *Chlamydomonas* swimming features in the shear flow and incorporates all experimentally observed phenomena.

In chapter 7, we conclude by briefly summarizing the main results and contribution of this work. We also present some future perspectives.

Chapter 2

Introduction en Français

2.1 Contexte

Les fluides complexes sont très courants dans notre environnement de tous les jours. Les fluides complexes incluent: les émulsions, les suspensions, les biofluides, les gels, les mousses, les polymères, les solutions, les cristaux liquides, les cristaux colloïdaux, etc. Parmi ces fluides on trouve: le sang, les crèmes cosmétiques ou pharmaceutiques, les aliments (lait, yaourt, chocolat, mayonnaise, etc). Habituellement les fluides complexes sont aussi des fluides non-newtoniens, ce qui signifie qu'ils n'obéissent pas à la relation (newtonienne) linéaire entre la contrainte appliquée (σ) et ($\dot{\gamma}$) le taux de cisaillement. Les fluides non-newtoniens présentent des comportements assez diversifiés, étonnants et intéressants, et qui est applicable à la fois en sciences et en technologie. Un des objectifs les plus importants de l'étude des fluides complexes est de comprendre le mécanisme (les forces et les interactions) agissant sur une échelle de longueur intermédiaire, qui définit le comportement de ces fluides. Cela donnerait une occasion de concevoir et de contrôler de nouveaux matériaux avec les propriétés souhaitées. Ce type de matériaux commencent à être utilisé dans l'ingénierie (automobile) ou en médecine par exemple.

Les fluides complexes sont des substances ayant une échelle de longueur intermédiaire, qui joue un rôle clé dans la détermination des propriétés de ces substances. Ces échelles de longueur intermédiaires existent entre les échelles de longueurs moléculaires et les échelles de longueurs macroscopiques. Elles proviennent par exemple des atomes et des molécules formant de grandes structures organisées, des colloïdes, des particules

microscopiques rigides ou même des micro-organismes vivants [1]. La science qui établit des relations entre les propriétés du fluide et de sa structure à l'échelle de longueur intermédiaire est la rhéologie. Plus généralement la rhéologie est l'étude de la déformation et de l'écoulement de la matière, en réponse à une contrainte appliquée. Les propriétés rhéologiques communes qui sont utilisées pour caractériser les fluides non-newtoniens comprennent: la viscosité effective (viscosité de cisaillement η_{eff}, la viscosité tourbillonnaire η^R_{eff}); le stress σ (contrainte de cisaillement, contrainte normale, différence de contraintes normales); le temps de relaxation τ; le module viscoélastique etc.

Les fluides non-newtoniens peuvent présenter un comportement rhéofluidifiant ou rhéo-épaississement sous cisaillement ainsi que des effets viscoélastiques (par exemple l'effet Weissenberg [2]). La fluidification est la tendance d'un fluide à réduire sa viscosité lorsqu'on lui applique un taux de cisaillement croissant [3]. Au contraire, le comportement rhéo-épaississant sous cisaillement est observé lorsque la viscosité du fluide augmente avec le taux de cisaillement [4, 5].

Les fluides complexes peuvent être étudiés en utilisant des approches analytiques, des simulations numériques ou des expériences. Dans ce travail, nous utilisons des simulations numériques et nous comparons nos résultats quand cela est possible à des observations expérimentales et des appoches analytiques.

2.2 Objectifs de la recherche

Dans cette thèse, nous analysons les propriétés telles que la viscosité effective des suspensions avec des particules actives. Ces particules actives peuvent être des micro-nageurs naturels, mais aussi des particules sensibles à des champ externes ou des particules confinées. Cette perturbation active a une conséquence sur les propriétés macroscopiques des suspensions: elle change sa viscosité effective. Notre étude nous a ainsi permis d'établir un lien entre les propriétés microscopiques et macroscopiques du fluide.

Ces dernières années il y a eu un intérêt considérable dans la physique des micro-nageurs. Ces micro-nageurs sont très répandues dans la nature. Par exemple: les bactéries et les spermatozoïdes dans les biofluides, les micro-algues, etc. La physique de ces micro-organismes est intéressante à la fois à des échelles de longueur microscopique pour décrire les nageurs individuels [6] et à une échelle de longueur plus grande en tant

que composants de systèmes complexes (ou «liquides actifs»). Malgré le fait que les micro-nageurs soient des organismes simples, la façon dont ils se déplacent à travers le fluide est plus compliquée que la façon dont nous nageons à notre échelle. Comme à l'échelle de longueur où ils vivent ($Re \ll 1$, où Re représente le nombre de Reynolds) l'inertie est négligeable et les micro-nageurs ont besoin de déformer ou de se propulser d'une façon non réciproque qui n'est pas invariante sous une symétrie d'inversion du temps [7, 8]. Outre les particularités du mécanisme de nage un fluide contenant un grand nombre de ces organismes change radicalement ses propriétés rhéologiques. Par exemple, les micro-nageurs changent la viscosité des fluides de la suspension à laquelle ils appartiennent [9, 10].

Un des principaux objectifs de cette thèse est une modélisation numérique des suspensions de micro-nageurs (à savoir des suspensions de *Chlamydomonas*) pour établir une relation entre les mécanismes microscopiques des mouvements de chaque cellule individuelle et les propriétés macroscopiques du fluide comme la viscosité effective. En cohérence avec les expériences réalisées dans notre équipe, les micro-algues *Chlamydomonas reinhardtii* ont été choisies comme système modèle pour comprendre l'effet de leur motilité sur les paramètres globaux macroscopiques de la suspension.

L'autre objectif de la thèse est d'étudier des questions plus fondamentales de la mécanique des fluides à un petit nombre de Reynolds, comme l'influence du confinment sur la dynamique des particules rigides dans un cisaillement de Couette. En effet l'interaction entre parois et particules est très important dans de nombreux dispositifs microfluidiques ou capillaires où la taille typique des systèmes biologiques ou des objets en suspension est comparable à une ou plusieurs dimensions des canaux, le nombre de publications est encore faible mais en pleine expansion concernant le traitement de ces effets de confinement sur des champs d'écoulement et de la mécanique des objets suspendus.

Un autre objectif de ce travail est l'étude numérique de suspensions avec une viscosité ajustable. Ces fluides sont constitués par des suspensions sensibles à des champs extérieurs (électriques ou magnétiques). Par exemple, dans les fluides électro rhéologiques (ER) où les particules sont sensibles aux champs électriques externes, on peut modifier la rotation des particules en utilisant un champ externe. Ainsi la viscosité de ces suspensions peut être ajustée en jouant sur l'orientation et l'intensité du champ appliqué.

Ces fluides à viscosité contrôlable ont des applications technologiques dans de nombreux types de systèmes industriels tels que les amortisseurs actifs, les embrayages ou les freins [11, 12]. Par exemple, selon les conditions routières, la viscosité du fluide peut être ajustée dans les amortisseurs automobiles [13]. La contribution d'un couple externe à la viscosité effective de suspensions de particules polaires a été étudié théoriquement en régime dilué par Brenner en 1970 [14]. Notre but ici est d'étendre notre compréhension sur une plus large gamme de concentrations et d'établir une relation entre le couple appliqué et les propriétés rhéologiques de ces suspensions.

2.3 Organisation du manuscrit

Le présent ouvrage est organisé comme suit.

Le chapitre 3 est consacré à la méthode numérique que nous utilisons, la dynamique des particules fluides (FPD). L'idée principale de la méthode ainsi que ses aspects positifs et négatifs sont décrits. La théorie sousjacente de la méthode FPD et certains détails des techniques de discrétisation numériques sont introduits. Nos nouvelles contributions, le nombre de modifications et d'extensions possibles de cette méthode sont répertoriés. Puisque la méthode FPD est relativement nouvelle dans le but de vérifier sa fiabilité et de l'illustrer, nous présentons quelques problèmes résolus en utilisant cette méthode en comparaison avec des résultats analytiques biens connus. Parmi eux, on peut citer l'écoulement de Stokes autour d'une sphère immobile; l'écoulement autour d'une particule sphérique dans un cisaillement de Couette; les collisions entre deux sphères et enfin l'orbite de Jeffery de particules ellipsoïdales dans un écoulement de cisaillement. Cette méthode FPD sera utilisée dans l'ensemble de ce travail pour résoudre plusieurs problèmes différents.

Le chapitre 4 décrit l'effet du confinement sur la dynamique d'une seule particule sphérique en suspension dans un écoulement de cisaillement. Deux effets majeurs sont considérés: la diminution de la vitesse de rotation de la sphère dans le flux de cisaillement due aux interactions particule-paroi et le changement de la vitesse de translation de la particule dans le voisinage de la paroi. Les champs d'écoulement sont présentés et les résultats sont comparés avec de précédentes prédictions numériques et analytiques.

Le chapitre 5 est consacré à l'étude numérique de la contribution d'un couple externe

appliqué sur une suspension de particules sensibles à un chmap extérieur. Ce champ exerce un couple sur ces particules qui augmente ou diminue la vitesse angulaire de chaque particule. La relation entre le couple appliqué sur chaque particule et la viscosité effective du fluide est établi au-delà du régime dilué et une formule semi-empirique est dérivée pour la viscosité effective. Une loi empirique du type seconde loi de Faxèn est établie et est valable jusqu'à 40% de concentration.

Le chapitre 6 traite des modèles et des simulations numériques associées aux suspensions de *Chlamydomonas*. Après une revue générale des micro-nageurs à faible nombre de Reynolds, les principales observations expérimentales effectuées sur des suspensions d'algues vertes sont résumées. Puis, plusieurs modèles différents sont pris en compte afin de comprendre les effets de la motilité des micro-nageurs sur les propriétés globales rhéologiques du fluide. La dernière section du chapitre 6 décrit le modèle qui convergent vers une distribution anisotrope des particules en prenant en compte la nage spécifiques des *Chlamydomonas* en fonction du taux de cisaillement et intègre tous les phénomènes observés expérimentalement.

Au chapitre 7, nous concluons en résumant brièvement les principaux résultats de ce travail. Nous présentons également une liste de quelques perspectives d'avenir qui nous semble intéressantes et facilement accessibles avec notre méthode numérique.

Chapter 3

Fluid Particle Dynamics

In this chapter, we describe the Fluid Particle Dynamics (FPD) which is the simulation method of colloidal (or non-colloidal) suspensions. The FPD method allows to avoid the difficulties which arise from solid-fluid boundary conditions by treating a colloid as a fluid particle. We describe the FPD method, introduce the theory behind it and considered the main features of the method. Number of changes and possible extensions made in the FPD method has been listed. Finally, we show some canonical problems solved using the FPD method in comparison to well known exact analytical solutions. Among them: Stokes flow past a sphere, a spherical particle in the shear flow and Jeffery's orbit for ellipsoidal particles in a shear flow. We also treat the collision between two spheres.

Dans ce chapitre, nous décrivons la méthode numérique de dynamique des particules fluides (FPD) qui est une méthode de simulation de suspensions colloïdales ou non colloïdales. La méthode FPD permet d'éviter les difficultés liées aux conditions aux limites particule solide-fluide en traitant une particule comme une particule fluide. Nous décrivons la méthode FPD en introduisant la théorie sousjacente. Nous examinons les principales caractéristiques de la méthode. Nous discutons des nombreux changements et des extensions qui ont été faites sur le code de cette méthode. Enfin, nous montrons quelques problèmes canoniques résolus en utilisant la méthode FPD en comparaison avec des solutions analytiques exactes bien connues . Parmi eux, l'écoulement de Stokes autour d'une sphère immobile, une particule sphérique dans un écoulement de cisaillement et les orbites de Jeffery pour des particules ellipsoïdales dans un cisaillement de Couette plan. Enfin nous simulons une collision entre deux sphères.

3.1 Introduction

The Fluid Particle Dynamics method (FPD) is used to simulate a suspension of colloidal or non-colloidal particles at low Reynolds number. This system presents a wide range of problems concerning suspensions like rheological behaviors under shear flow, their confinement [15, 16, 17, 18, 19, 20], suspension under an external field [14, 21, 22, 23],

the kinetics of colloidal aggregation [24, 25, 26, 27], phase separation [28, 29, 30, 31, 32], gel formation [33, 34], crystallization [35, 36, 37, 38, 39] etc. This method was originally developed by Tanaka and Araki in two dimensions [40], then extended to three dimensions by Peyla [15, 16]. In other simulation methods such as: Stokesian Dynamics [41] or Lattice Boltzmann methods [42] colloidal suspensions are treated as a mixture of solid particles and a simple liquid as it is in reality. Unlike those methods, within the FPD method, colloidal suspensions are treated as a mixture of viscous fluid particles in a less viscous simple Newtonian liquid. The method is based on a hybrid model which uses the lattice simulation for the continuous fields (velocity, pressure and viscosity) and an off-lattice simulation for the suspended particles. The main advantage of the FPD method is that it allows us to avoid explicitly tracking solid-fluid boundary of a colloidal particle and thus avoid applying the boundary conditions at the moving surface of the particles. This kind of methods is also known as "penalty method" [43]. The method also automatically implies the finite size of the colloids unlike the Brownian Dynamics method [44] where the particles are treated as point-like particles. An important point is that the FPD method provides a proper handling of the hydrodynamic interactions between particles in a suspension which play a key role in many problems concerning suspensions. The FPD method is not suitable to study a deformable or elastic particles such as vesicles or red blood cells. However, the method is convenient to study collective effects in the suspensions, confinement as well as dynamics of single objects (movement, rotation, diffusion etc.). Spherical or ellipsoidal objects are treated in this work.

3.2 Theory of the FPD method

The motion of incompressible fluid is described by the Navier-Stokes equation and the incompressibility condition:

$$\rho\Big(\frac{\partial \mathbf{v}}{\partial t} + \mathbf{v}\cdot\nabla\mathbf{v}\Big) = \nabla\sigma + \mathbf{f}, \tag{3.1}$$

$$\nabla\mathbf{v} = 0, \tag{3.2}$$

where $\mathbf{v}$ is the velocity field of the fluid, ρ is the fluid density which is assumed to be

the same for the particles and the solvent. $\mathbf{f}$ represents the external and internal force field (for example exerted by a swimmer) per unit volume acting on the fluid. The stress tensor $\boldsymbol{\sigma}$ is given by the Newtonian law:

$$\sigma_{i,j} = -p\delta_{i,j} + \eta(\partial_i v_j + \partial_j v_i), \tag{3.3}$$

where η is the viscosity of the fluid and p the pressure field. Derivation of the Navier-Stokes equation (3.1) and the incompressibility condition (3.2) starts from application of Newton's Laws.

Within the FPD method, one can apply the Navier-Stokes equation on a colloidal suspension without suffering from constructing solid-fluid boundary condition on moving boundary. The problem is circumvented as following: the particles in suspension are defined as a high viscosity region in comparison to the solvent viscosity. Therefore, the flow field is defined in the entire domain and not only outside the particles. Then the colloidal suspension is treated as a mixture of viscous fluid particles (with the particle viscosity η_p) and less-viscous liquid (with the solvent viscosity η). When the viscosity contrast tends to infinity ($\eta_p/\eta \to \infty$), fluid particles can be regarded as solid ones. This ratio η_p/η defines the accuracy of the approximation. In our simulations, we usually use fixed high viscosity contrast, such as $\eta_p/\eta = 100$ to avoid any recirculation of the fluid inside the particles (see figure 3.14). The particle number n which is off-lattice centered is located at $\mathbf{r}_n$ and is represented by the auxiliary field:

$$\varphi_n(\mathbf{r}) = \frac{1}{2}\left[1 + tanh\Big(\frac{a - |\mathbf{r} - \mathbf{r}_n|}{\xi}\Big)\right], \tag{3.4}$$

ξ represents the fluid-particle interface thickness where viscosity decays form the particle viscosity η_p to the solvent viscosity η, and a is the size of the particles. So, the effective radius of the beads is $R_{eff} \simeq a + 2\xi$. The figure 3.1 shows the viscosity profiles around the single particle with $a = 3\delta$, $\xi = 0.5\delta$ where $\delta = 1$ is the mesh size, $\eta = 1$ and $\eta_p = 100$. In that way, the difficulty associated with the sharp interface between each moving spheres and the fluid is circumvented by introducing a diffuse interface. Then using the auxiliary field (3.4) the spatial distribution of the viscosity field for N spherical

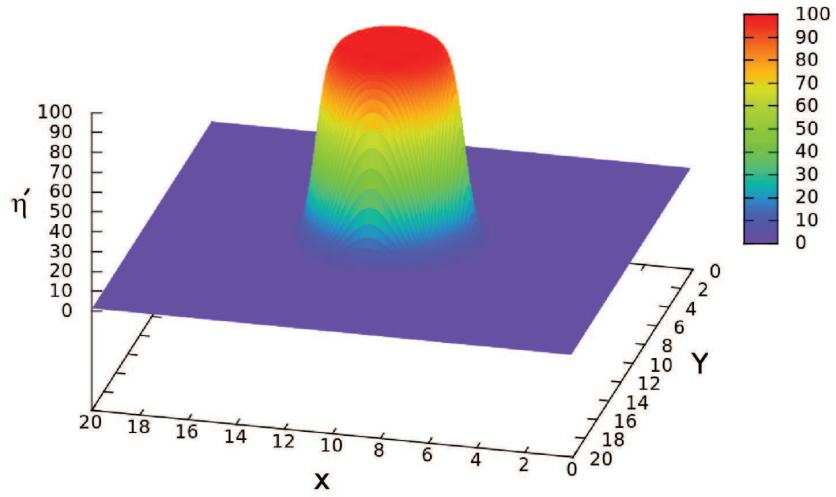

Figure 3.1: The viscosity field around a single particle. $\eta = 1$ and $\eta_p = 100$.

particles is defined as:

$$\eta^{'}(\mathbf{r}) = \eta + (\eta_p - \eta) \sum_{n=1}^{N} \varphi_n(\mathbf{r}). \tag{3.5}$$

This ensures that far enough from a particle the local viscosity is $\eta' = \eta$ (the solvent viscosity) and inside the particle viscosity is $\eta' = \eta_p$ (the particle viscosity).

Using equations (3.3) and (3.5) Navier-Stokes equation (3.1) with the incompressibility condition can be rewritten as follows:

$$\rho(\partial_t + \mathbf{v}\cdot\nabla)\mathbf{v} = -\nabla p + \nabla[\eta(\mathbf{r})(\nabla\mathbf{v} + (\nabla\mathbf{v})^T)] + \mathbf{f} \tag{3.6}$$

$$\nabla \cdot \mathbf{v} = 0. \tag{3.7}$$

FPD equations (3.6) and (3.7) are used to simulate dynamics of the fluid/particles systems. They are solved numerically using the Projection Method, on the three dimensional MAC-grid [45].

Note that despite the fact that we are concerned about low Reynolds number fluid mechanics we solve numerically the Navier-Stokes equation (3.1) and not the Stokes

equation. Therefore, our code is able to handle small but finite Reynolds numbers. Usually, we work with Reynolds number $R < 1$, therefore inertial effects are indeed negligible.

3.3 The Projection Method

To solve numerically time-dependent Navier-Stokes equation under incompressibility condition an explicit finite-difference scheme, so called "Projection Method" was originally and independently proposed by Corim (1968) and Team (1969) [46, 47]. The explicit version of the method was proposed by Fortin et. al. (1971) [48]. The method can be divided schematically into three main steps. At the first step, after discretization in time of (3.6) one calculates intermediate "wrong" velocity field $\mathbf{v}^*$ with

$$\frac{\mathbf{v}^* - \mathbf{v}^n}{\delta t} + (\mathbf{v}\cdot\nabla)\mathbf{v} = \frac{\nabla[\eta(\mathbf{r})(\nabla\mathbf{v} + (\nabla\mathbf{v})^T)]}{\rho} + \frac{\mathbf{f}}{\rho}, \tag{3.8}$$

Where δt is the time step. Note that the pressure term is omitted in (3.8).

$$\mathbf{v}^* = \mathbf{v}^n + \delta t \left\{ \frac{\nabla[\eta(\mathbf{r})(\nabla\mathbf{v} + (\nabla\mathbf{v})^T)]}{\rho} + \frac{\mathbf{f}}{\rho} - (\mathbf{v}\cdot\nabla)\mathbf{v} \right\}. \tag{3.9}$$

To calculate the divergence free velocity field $\mathbf{v}^{n+1}$ (the "real" velocity) at time step $n+1$ we start from

$$\frac{\mathbf{v}^{n+1} - \mathbf{v}^*}{\delta t} + \frac{\nabla p}{\rho} = 0. \tag{3.10}$$

Note that if we combine equations (3.8) and (3.10) the $\mathbf{v}^*$ will cancel and we obtain equation (3.6) discretized in time.

By Taking divergence of (3.10) and using (3.7) i.e. incompressibility condition for the new velocity field ($\nabla \cdot v^{n+1} = 0$) one obtains

$$\nabla\cdot\left(\frac{\nabla p}{\rho}\right) = \frac{\nabla\cdot\mathbf{v}^*}{\delta t}. \tag{3.11}$$

or

$$\Delta p = \nabla\cdot\mathbf{v}^*\frac{\rho}{\delta t}. \tag{3.12}$$

We solve numerically the Poisson's equation (3.12) to find the pressure field p by using intermediate velocity field $\mathbf{v}^*$, this is the second step of the Projection Method. To solve equation (3.12), we use two different methods discussed below in section 3.5.

At the last step one uses equation (3.10) to obtain new velocity field $\mathbf{v}^{n+1}$ at time step $n+1$ using velocity field $\mathbf{v}^*$ and pressure field p,

$$\mathbf{v}^{n+1} = \mathbf{v}^* - \frac{\delta t}{\rho}\nabla p. \tag{3.13}$$

3.4 MAC grid and discretization

Equations (3.9), (3.12) and (3.13) are solved numerically on a three-dimensional special grid so called "Marker And Cells grid" (MAC grid) [45, 46, 49]. On the MAC grid scalar values such as pressure $p_{i,j,k}$ and viscosity $\eta_{i,j,k}$ as well as stress tensor $\sigma_{i,j,k}$ are defined at the center of the (i,j,k) cell while velocity $\mathbf{v} = (u,v,w)$ components: $u_{i\pm\frac{1}{2},j,k}$, $v_{i,j\pm\frac{1}{2},k}$ and $w_{i,j,k\pm\frac{1}{2}}$ are defined at the corresponding faces of the (i,j,k) cell as shown in figure 3.2. For the components of equation (3.9) one finds:

$$u^* = u^n + \delta t\left\{\frac{(2\eta u_x)_x + (\eta(u_y+v_x))_y + (\eta(u_z+w_x))_z}{\rho} + \frac{f_x}{\rho} - (\mathbf{v}\cdot\nabla)u\right\}, \tag{3.14}$$

$$v^* = v^n + \delta t\left\{\frac{(\eta(u_y+v_x))_x + (2\eta v_y)_y + (\eta(v_z+w_y))_z}{\rho} + \frac{f_y}{\rho} - (\mathbf{v}\cdot\nabla)v\right\}, \tag{3.15}$$

$$w^* = w^n + \delta t\left\{\frac{(\eta(u_z+w_x))_x + (\eta(v_z+w_y))_y + (2\eta w_z)_z}{\rho} + \frac{f_z}{\rho} - (\mathbf{v}\cdot\nabla)w\right\}. \tag{3.16}$$

To calculate the velocity components (u^*, v^*, w^*) and then update velocity components (u, v, w) equations (3.14), (3.15) and (3.16) are written on appropriate cell faces. Note that we consider field $\eta(\mathbf{r})$ which will be useful in our numerical method. Discretization of the first viscous term $(2\eta u_x)_x$ in the equation (3.14) at the point $\mathbf{x}_{i+1/2,j,k}$ where u_x denotes the partial derivation of the velocity

$$u_x = \frac{\partial u}{\partial x}$$

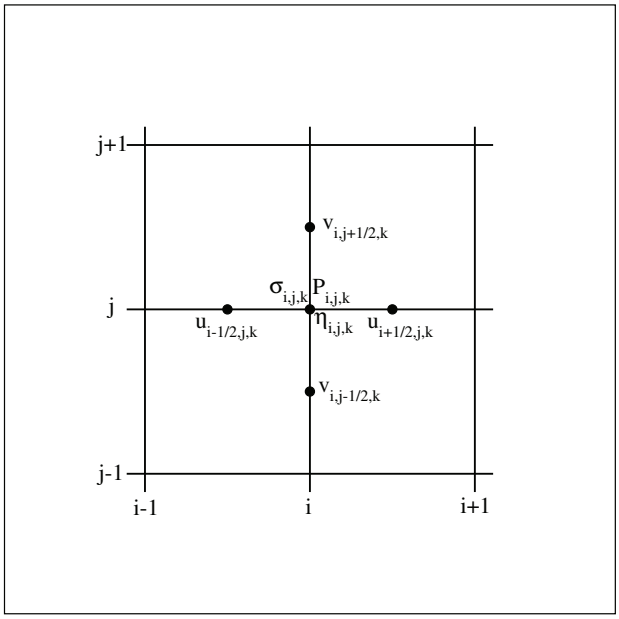

Figure 3.2: The MAC mesh.

using the central differencing gives:

$$(2\eta u_x)_x = \frac{2\eta_{i+1,j,k}(u_x)_{i+1,j,k} - 2\eta_{i,j,k}(u_x)_{i,j,k}}{dx}, \tag{3.17}$$

where

$$(u_x)_{i,j,k} = \frac{u_{i+1/2,j,k} - u_{i-1/2,j,k}}{dx}, \tag{3.18}$$

and finally

$$(2\eta u_x)_x = \frac{2}{dx}\left\{\eta_{i+1,j,k}\frac{u_{i+3/2,j,k} - u_{i+1/2,j,k}}{dx} - \eta_{i,j,k}\frac{u_{i+1/2,j,k} - u_{i-1/2,j,k}}{dx}\right\}. \tag{3.19}$$

For the second viscous term in the equation (3.14) at the same point $\mathbf{x}_{i+1/2,j,k}$ one finds:

$$(\eta(u_y + v_x))_y = \frac{\eta_{i+1/2,j+1/2,k}(u_y + v_x)_{i+1/2,j+1/2,k} - \eta_{i+1/2,j-1/2,k}(u_y + v_x)_{i+1/2,j-1/2,k}}{dy}. \tag{3.20}$$

Where

$$(u_y)_{i+1/2,j+1/2,k} = \frac{u_{i+1/2,j+1,k} - u_{i+1/2,j,k}}{dy}, \tag{3.21}$$

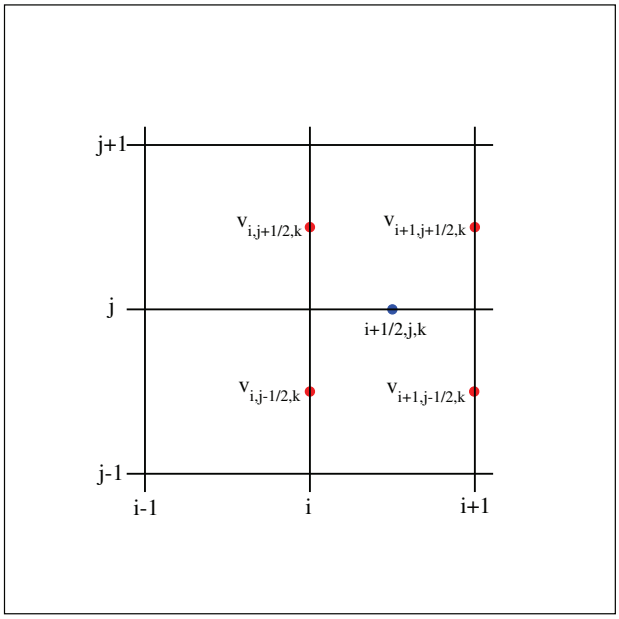

Figure 3.3: The XY cross section of the MAC mesh.

$$(u_y)_{i+1/2,j-1/2,k} = \frac{u_{i+1/2,j,k} - u_{i+1/2,j-1,k}}{dy}, \tag{3.22}$$

and

$$(v_x)_{i+1/2,j\pm1/2,k} = \frac{v_{i+1,j\pm1/2,k} - v_{i,j\pm1/2,k}}{dx}. \tag{3.23}$$

The viscosity η is defined at the center of cells (on the grid points). But by simply averaging it can be defined everywhere:

$$\eta_{i+1/2,j\pm1/2,k} = \frac{\eta_{i,j,k} + \eta_{i+1/2,j,k} + \eta_{i,j\pm1/2,k} + \eta_{i+1/2,j\pm1/2,k}}{4}. \tag{3.24}$$

In the same way the third viscous term in the equation (3.14) will be discretized as follows:

$$(\eta(u_z + w_x))_z = \frac{\eta_{i+1/2,j,k+1/2}(u_z + w_x)_{i+1/2,j,k+1/2} - \eta_{i+1/2,j,k-1/2}(u_z + w_x)_{i+1/2,j,k-1/2}}{dz}, \tag{3.25}$$

where

$$(u_z)_{i+1/2,j,k+1/2} = \frac{u_{i+1/2,j,k+1} - u_{i+1/2,j,k}}{dz}, \tag{3.26}$$

$$(u_z)_{i+1/2,j,k-1/2} = \frac{u_{i+1/2,j,k} - u_{i+1/2,j,k-1}}{dz}, \tag{3.27}$$

and

$$(w_x)_{i+1/2,j,k\pm1/2} = \frac{w_{i+1,j,k\pm1/2} - w_{i,j,k\pm1/2}}{dx}. \tag{3.28}$$

In a similar manner the viscous terms of equations (3.15) and (3.16) can be discretized as well.

Discretization of the convective terms in equations (3.14-3.16) for example $(\mathbf{v}\cdot\nabla)u$ at the point $\mathbf{x}_{i+1/2,j,k}$ where only the first component of velocity $u_{i+1/2,j,k}$ is defined requires averaging for other velocity components. In figure 3.3 it is shown the xy cross section of the MAC mesh. The velocities on the red points are used to calculate the velocity component $v_{i+1/2,j,k}$ at the point $\mathbf{x}_{i+1/2,j,k}$ (blue point).

$$v_{i+1/2,j,k} = \frac{v_{i,j-1/2,k} + v_{i,j+1/2,k} + v_{i+1,j-1/2,k} + v_{i+1,j+1/2,k}}{4}, \tag{3.29}$$

and

$$w_{i+1/2,j,k} = \frac{w_{i,j,k-1/2} + w_{i,j,k+1/2} + w_{i+1,j,k-1/2} + w_{i+1,j,k+1/2}}{4}. \tag{3.30}$$

In equation 3.9 to handle the advective term $(\mathbf{v}\cdot\nabla)\mathbf{v}$, we use WENO method (Weighted Essentially Non-Oscillatory polynomial interpolation of data for the numerical solution of conservation laws) method [45].

3.5 Numerical algorithm for the FPD method

In this section, we present sequences of successive basic numerical operations in the Fluid Particle Dynamics method and some specific details of the method. For sake of simplicity, we neglect thermal fluctuations and assume that the density of the suspended fluid particles is the same as the density of the solvent. We consider the low Reynolds number fluids and therefore the advective term $(\mathbf{v}\cdot\nabla)\mathbf{v}$ in most cases is negligible and in such cases we neglect it. However, the absence of the inertial terms is the origin of a slow artificial particle migration perpendicular to the flow. Therefore, in some cases when we need long term observation of a suspension (for example when number of iteration is much more than 10^6) the convective term can be important and we keep

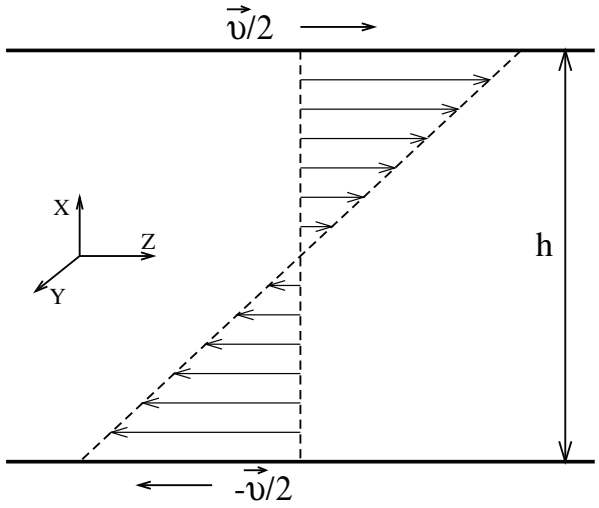

Figure 3.4: Shear flow.

it.

Initially, we take three-dimensional $[N_x]\,[N_y]\,[N_z]$ equal spacing ($dx = dy = dz = \delta = 1$) MAC grid and initialize parameters such as number and size of suspended particles (objects). The next step is to define an initial flow. In the case of a shear flow, we either impose constant and opposite values of velocities on two opposite plates in a given direction or impose initial velocity everywhere inside the fluid as

$$w(x) = \dot{\gamma} x, \tag{3.31}$$

where $\dot{\gamma}$ is the shear rate and velocities of plates are $v = \pm\dot{\gamma}h/2$, here h is the distance between the plates (see figure 3.4). We use no-slip conditions at the fluid/walls interface. For example in the case of a Poiseuille flow, we can impose pressure gradient in one direction. We impose the periodic boundary condition in the same direction (the z direction on figure 3.4). In x and y directions, we consider walls with no-slip boundary conditions. After initializing the flow, we set the initial positions and orientations of the suspended objects. Those objects can be simple spherical particles, ellipsoidal particles, dumbbells or chain of a few spherical/ellipsoidal particles. To study a disordered phase of a suspension, we randomly and isotropically distribute objects in the simulation box

(taking care to avoid any overlaps). To obtain a random distribution of particles, it is convenient to use a random variable uniformly distributed on $[0;1]$ interval ($x_i \in [0;1]$),

$$r_i = a_i + (b_i - a_i)x_i$$

where $i = 1, 2, 3$ for a three-dimensional box, a_i and b_i are the edges of a box in each direction and r_i is the random number in the $[a_i; b_i]$ interval. To obtain an isotropic random distribution of objects one needs an isotropic distribution of vectors in three dimensions. This can be obtained in the spherical coordinate by defining the angular variables as follow:

$$\phi{=}\pi(1 - 2x_1)$$

and

$$cos(\theta) = 1 - 2x_2$$

where x_1 and x_2 are random variables defined in the $[0;1]$ interval. Note that the distribution associated with the random variable is uniform in $[0;1]$ interval.

After initializing the particles position, we can define the viscosity field in the whole suspension using the equations (3.4) and (3.5). The next step is the calculation of the viscous terms, advective terms $(\mathbf{v}\cdot\nabla)u$ (if it is taken into account) and forces $\mathbf{f}$ in equations (3.14), (3.15) and (3.16). The calculation of forces varies depending on the chosen system of suspended objects, presence of an external field, configuration of suspensions, etc. Once viscous terms, advective terms and forces are calculated, we can calculate $\mathbf{v}^*$ velocity field using the equations (3.14-3.16). This is the first step of the Projection Method (PM). Then using $\mathbf{v}^*$, we solve the Poisson's equation (3.12) to find the pressure field (second step of the PM).

To solve the Poisson's equation, we use either one of two different numerical methods. The first method is the Successive Over Relaxation (SOR) method where instead of directly solving the Poisson's equation (3.12), we solve the following equation:

$$\frac{\partial p}{\partial \tau} = \Delta p - \nabla\cdot\mathbf{v}^*\frac{\rho}{dt}. \tag{3.32}$$

Here τ is an artificial time and the equation (3.32) is solved by a 3^{rd} order Euler method until an absolute value of each side of the equation is smaller than the chosen value

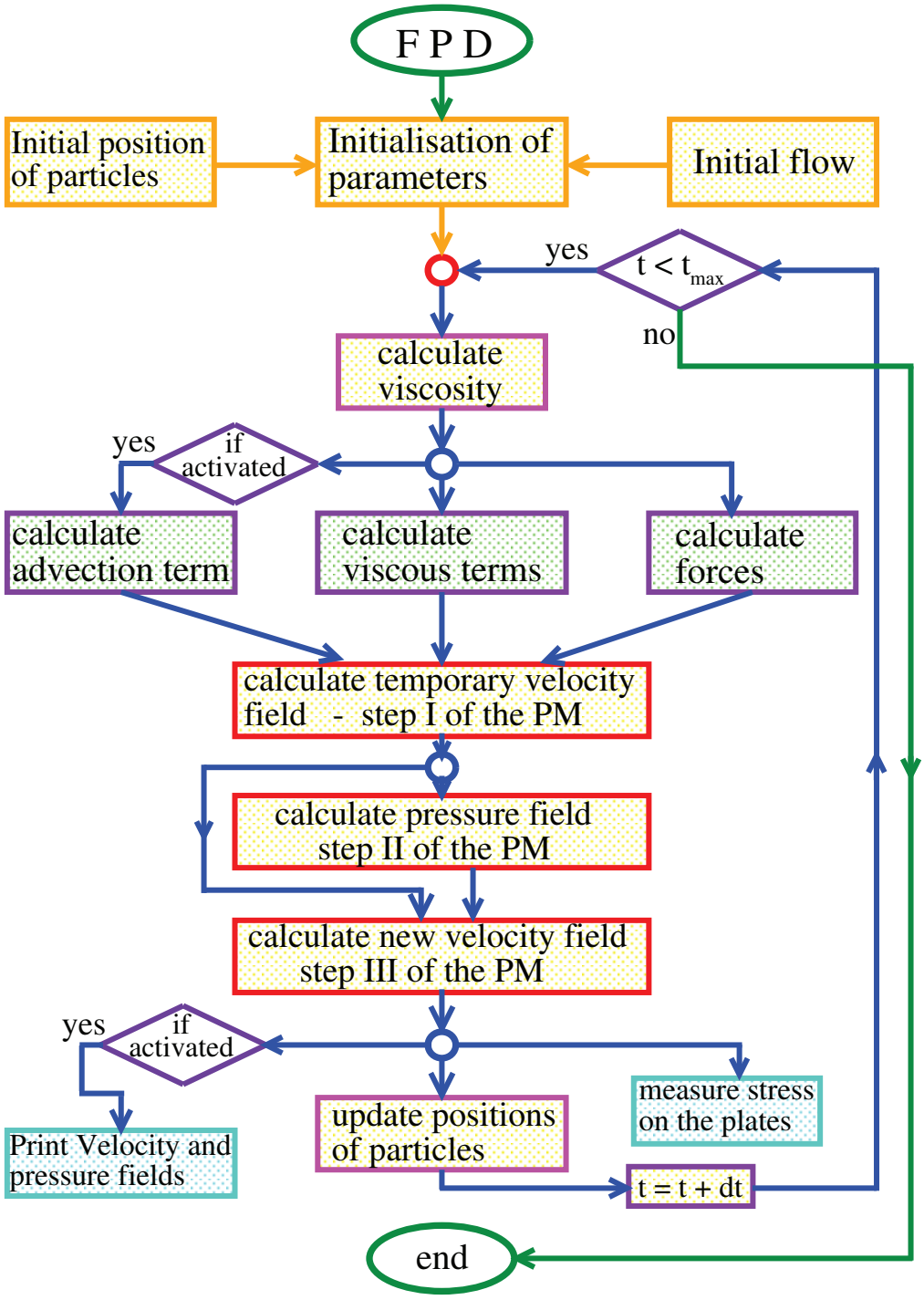

Figure 3.5: Basic flow chart of an algorithm for the FPD method.

which defines an accuracy of the numerical solution. The second method which we use to calculate numerically the equation (3.12) is based on direct solver of the Poisson's equation from the FISHPACK library [50]. Once the temporary velocity field $\mathbf{v}^*$ and pressure field is found using the equation (3.13) the new velocity field $\mathbf{v}^{n+1}$ can be calculated immediately. This is the third step of the PM. At this stage, we have full information about viscosity, velocity and pressure field in whole suspension at proper places (viscosity and velocity are defined at the center of cells and velocity components are defined on the corresponding faces) and we can calculate the stress components. The last step of the full loop is updating positions of the particles in the suspension as following:

$$\mathbf{r}_n(t+dt) = \mathbf{r}_n(t) + \langle \mathbf{v}_n \rangle \, dt, \tag{3.33}$$

where $\mathbf{r}_n$ is the coordinate of the $n-th$ particle center and $\langle \mathbf{v}_n \rangle$ denotes the average velocity inside of this particle:

$$\langle \mathbf{v}_n \rangle = \frac{\sum \alpha \mathbf{v^{n+1}}}{\sum \alpha}. \tag{3.34}$$

To ensure averaging inside a particle initially, we take a close cube around the particle and then use the factor,

$$\alpha = \frac{\eta_{i,j,k} - \eta}{\eta_p - \eta},$$

which is close to 1.0 inside the particle (in high viscosity region) and decreases down to zero outside and close to the particle. When $\xi = 0$, there are only two possible values for α: inside particles $\alpha = 1$ and everywhere else $\alpha = 0$. The basic flow chart of an algorithm for the FPD method is shown in figure 3.5.

3.6 Determination of the volume fraction

The volume fraction ϕ of a suspension is defined as the volume of suspended phase (particles for example) divided by the whole volume of the suspension.

$$\phi = \frac{\sum_{i=1}^{N} V_i'}{V}, \tag{3.35}$$

where N is the number of suspended particles, V_i' is the volume of the $i-th$ particle

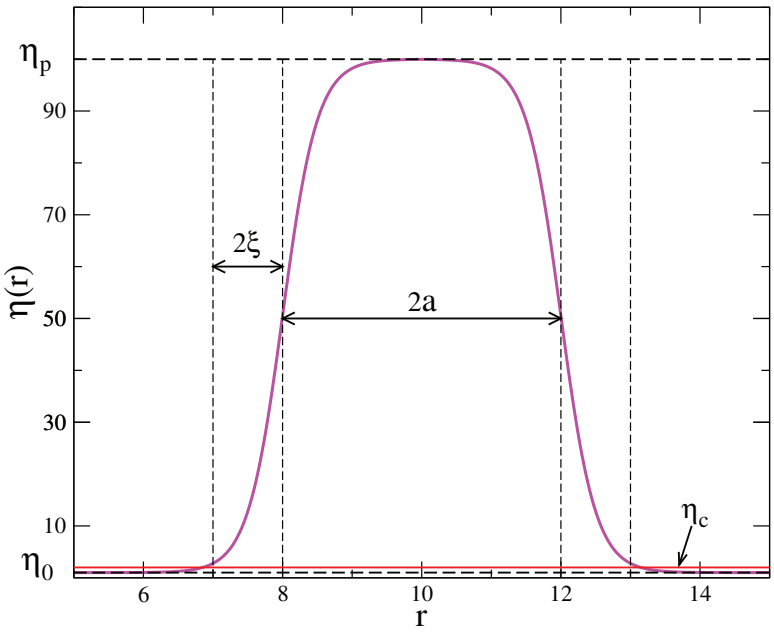

Figure 3.6: The viscosity profile of a spherical particle.

and V denotes the total volume of the suspension. For the suspension of spherical mono-disperse spheres of radius R the volume fraction will be:

$$\phi = \frac{\frac{4}{3}\pi R^3 N}{V}. \tag{3.36}$$

In the FPD method the use of equation (3.35) even for a suspensions of identical spherical particles is complicated because of the presence of a shell (of size 2ξ), where viscosity decreases from the particle viscosity η_p to the solvent viscosity η and an effective radius of beads are not clearly defined (figure 3.6). Furthermore, if two particles touch each other their total volume can be slightly changed. Therefore, we use an empirical critical value of viscosity η_c in order to estimate the volume fraction ϕ. Namely, we count the number of cells, where viscosity is higher than η_c ($\eta_{i,j,k} > \eta_c$), then the ratio of this number over the total number of cells in the simulation box gives estimation of the volume fraction of the suspension. The critical value of viscosity η_c depends on the ratio ξ/a, where ξ is the fluid-particle interface thickness and a is the typical size of a particle, it also depends on the particle viscosity η_p and solvent viscosity η. The viscosity profile in the middle of a spherical particle for $a = 2\delta$, $\xi = 0.5\delta$, $\eta = 1$,

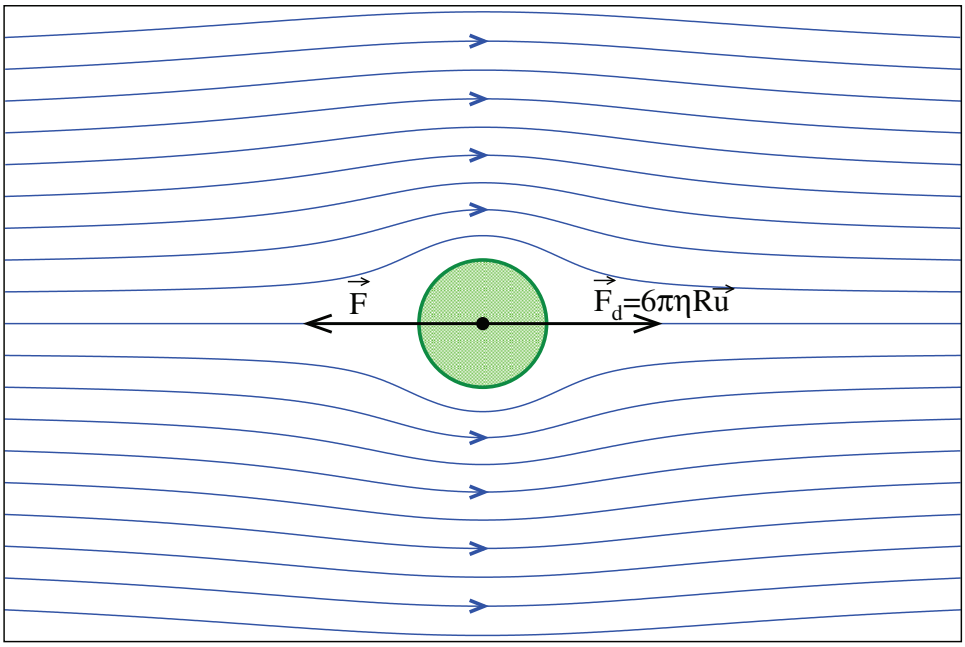

Figure 3.7: Forces on and streamlines around a sphere in Stokes flow.

$\eta_p = 100$, $\eta_c = 2$ and $R_{eff} \simeq a + 2\xi = 3\delta$ ($\delta = 1$ is the mesh size) is plotted in figure 3.6. To determine the value of η_c and then the volume fraction, we use two different ways. The first way is to put spherical particles in a uniform Stokes flow and apply a force $\mathbf{F}$ which is required to compensate the drag force $\mathbf{F}_d$ exerted by the flow on the particle and make it immobile (see figure 3.7).

$$\mathbf{F}_d = 6\pi\eta R\mathbf{U}, \tag{3.37}$$

here $\mathbf{U}$ is the flow velocity at infinity. At equilibrium $\mathbf{F} = \mathbf{F}_d$ and from equation (3.37) the effective radius R_{eff} can be determined. Using the effective radius for a single particle, one can estimate the value of the critical viscosity η_c and R_{eff} for given values of a and ξ.

The second method to determine the value of the critical viscosity is to chose it in such a way that the volume fraction and the corresponding effective viscosity η_{eff} (of suspensions of rigid spherical particles) is in agreement with the Einstein's law in dilute

regime,

$$\eta_{eff} = \eta(1 + \frac{5}{2}\phi),$$

Both ways for determining η_c is consistent to each other and gives the same results. For example for spheres with radius $a = 2\delta$ and thickness $\xi = 0.5\delta$ the critical value of viscosity is $\eta_c = 2$ which corresponds to the effective radius $R_{eff} \simeq a + 2\xi = 3\delta$ as shown in figure 3.6.

3.7 Improvement and extension of the FPD method

In this section, I briefly list the improvements and extensions I made to the FPD method.

1. In the Successive Over Relaxation (SOR) method for solving the Poisson's equation (3.12) instead of equally relaxing all the cells in the simulation box, we can separately relax part of them where absolute value of the right hand side of equation (3.32) is bigger to the value estimated on the rest of the cells which are already below the precision value. Depending on the amplitude and intensity of the forces in simulation box this modification speeds up the calculations time by factor from 1 to 12.

2. Adding the periodic boundary condition in all directions. In the case of a shear flow the periodic boundary conditions can be applied only in two directions. For example along z and y in figure 3.4.

3. Generalization of the shape of suspended particles to an ellipsoidal shape. Instead of the auxiliary field (3.4) which can only express spherical particles, we use the generalized auxiliary field (3.38). It makes possible to describe any particle (or part of object) of ellipsoidal shape.

$$\varphi_n(\boldsymbol{r}) = \frac{1}{2}\left[1 + tanh\left(\frac{(abc)^{1/3}(1-s)}{\xi}\right)\right], \tag{3.38}$$

and

$$s = \sqrt{\frac{(\Delta\mathbf{r}_n.\mathbf{n}_a)^2}{a^2} + \frac{(\Delta\mathbf{r}_n.\mathbf{n}_b)^2}{b^2} + \frac{(\Delta\mathbf{r}_n.\mathbf{n}_c)^2}{c^2}}, \tag{3.39}$$

where $\Delta\mathbf{r}_n = \mathbf{r} - \mathbf{r}_n$, $\mathbf{r}_n$ is the off-lattice center of the $n-th$ ellipsoid, a, b, and c are semi-axes and $\mathbf{n}_a$, $\mathbf{n}_b$ and $\mathbf{n}_c$ are orthogonal unit vectors along those semi-axes,

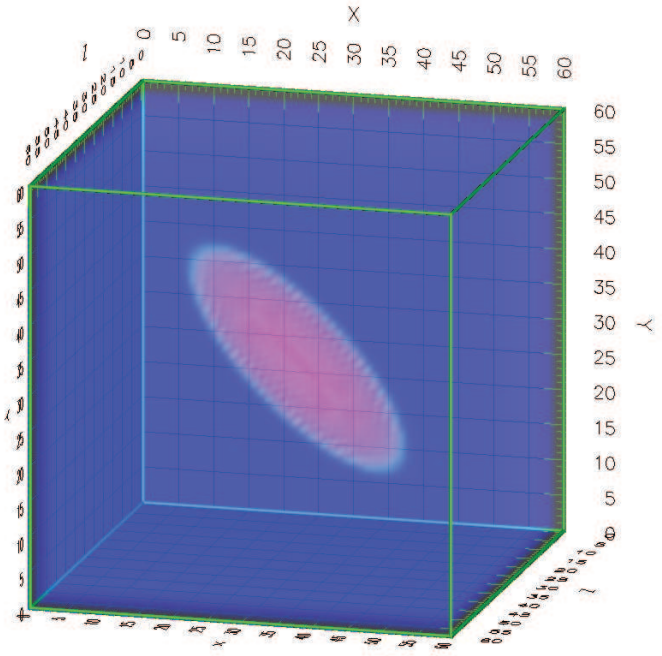

a)

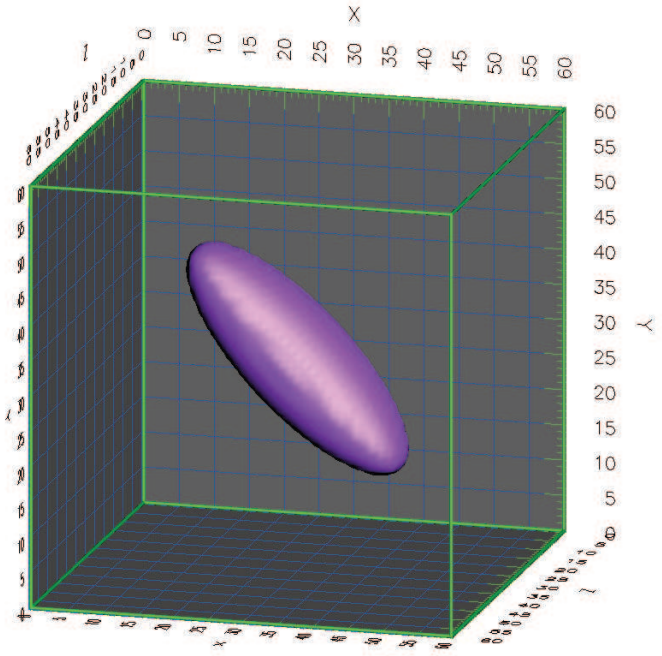

b)

Figure 3.8: Three dimensional view of the ellipsoidal particle in the simulation box. a) The viscosity field. b) Isosurface of the viscosity field.

respectively. Moreover in the case of an ellipsoidal particle one needs to rotate the unit vectors $\mathbf{n}_a$, $\mathbf{n}_b$ and $\mathbf{n}_c$ of each ellipsoids at each time iteration. To do so, we calculate the vorticity vector $\boldsymbol{\omega}$ of each ellipsoids at every iteration by averaging components of the vorticity inside ellipsoids. The angular velocity $\boldsymbol{\Omega}$ is half of the vorticity,

$$\boldsymbol{\omega}_n = \boldsymbol{\nabla} \times \mathbf{v}_n = 2\boldsymbol{\Omega}_n$$

Using the average angular velocity

$$\langle \boldsymbol{\Omega} \rangle = \frac{1}{n} \sum_n \boldsymbol{\Omega}_n \tag{3.40}$$

one can rotate the unit vectors $\mathbf{n}_a$, $\mathbf{n}_b$ and $\mathbf{n}_c$ as follow:

$$\mathbf{n}_i(t + dt) = \mathbf{n}_i(t) + dt(\langle \boldsymbol{\Omega} \rangle \times \mathbf{n}_i(t)), \tag{3.41}$$

where $i = a, b, c$. We need to carefully rotate the smallest parallelepiped around the ellipsoid where averaging (equation 3.40) takes places with the particle. On figure 3.8 we show three dimensional view of the ellipsoidal particle with $a = 20\delta$, $b = c = 7\delta$, $\xi = 0.5\delta$, $\eta = 1$, $\eta_p = 100$, $\mathbf{n}_a = (-1/\sqrt{2}, 1/\sqrt{2}, 1)$, $\mathbf{n}_b = (0, 0, 1)$ and $\mathbf{n}_c = (1/\sqrt{2}, 1/\sqrt{2}, 1)$ a) the viscosity field. b) the isosurface of the viscosity field.

4. In a shear flow, applying force (shear stress) on the plates and measure the established shear rate instead of applying a given shear rate (by applying constant velocities on plates) and calculating stress close to walls (plates). If we impose the shear stress, the velocity of plates varies according to the average velocities on their closest active layers.

5. Calculation of forces in equations (3.14), 3.15) and (3.16) for every individual studding systems (models). For swimmers for example (see chapter 6).

3.8 Examples

In this section, are presented some canonical results obtained using the FPD method in comparison to corresponding well known analytical solutions to validate the FPD method.

3.8.1 Stokes flow past a sphere

One of the fundamental results in low Reynolds number hydrodynamics is the Stokes solution for a uniform flow past a sphere. The exact analytical solutions for velocity components and the pressure in the spherical coordinate system (r, θ, ϕ) at zero Reynolds number have the following form [51]:

$$v_r = Ucos\theta \left[1 + \frac{R^3}{2r^3} - \frac{3R}{2r}\right], \tag{3.42}$$

$$v_\theta = -Ucos\theta \left[1 - \frac{R^3}{4r^3} - \frac{3R}{4r}\right], \tag{3.43}$$

and

$$p = p_\infty - \frac{3}{2}\frac{\eta UR}{r^2}cos\theta. \tag{3.44}$$

Here v_r and v_θ are the radial and angular components of fluids velocity in the spherical coordinates, U and p_∞ are the velocity and pressure of the uniform flow at infinity (far enough from the sphere), η is the viscosity of the fluid and R is the sphere radius. In order to numerically simulate Stokes flow fast a sphere, we use a simulation box with dimension [60][60][60] and impose an initial uniform flow everywhere with the velocity $\mathbf{v} = (0, 0, U)$, where $U = 0.02$ is constant on the boundaries. Then we use a spherical particle with a radius $a = 4\delta$; and fluid-particle interface thickness $\xi = 0.5\delta$, ($R_{eff} \simeq a + 2\xi = 5\delta$) placed in the middle of the box. We apply a force $\mathbf{F} = -\mathbf{F}_d = -6\pi\eta R\mathbf{v}$ according to equation (3.37) at the center of the particle to compensate the drag exerted by the flow on the particle (see figure 3.7). Size of the simulation box in each direction is six times bigger than the diameter of the particle, so we neglect a confinement effect due to the finite size of box and keep fixed the velocity of the fluid on the boundary plates of the box perpendicular to the x axis. On figure 3.9 we show the superposition of two (numerical and analytical) velocity fields for the spherical particle in the uniform Stokes flow with $U = 0.02$, $a = 4\delta$, $\xi = 0.5\delta$, $R_{eff} \simeq a+2\xi = 5\delta$ ($\delta = 1$ is the mesh size). The dark green circle corresponds to the radius a and the light green circle corresponds to the radius with diffusive interface $a+2\xi$. Three dimensional view of the velocity field around the spherical particle in the uniform Stokes flow are shown on figure 3.12 for the same values of the parameters. We also show relative errors of the velocity field. On

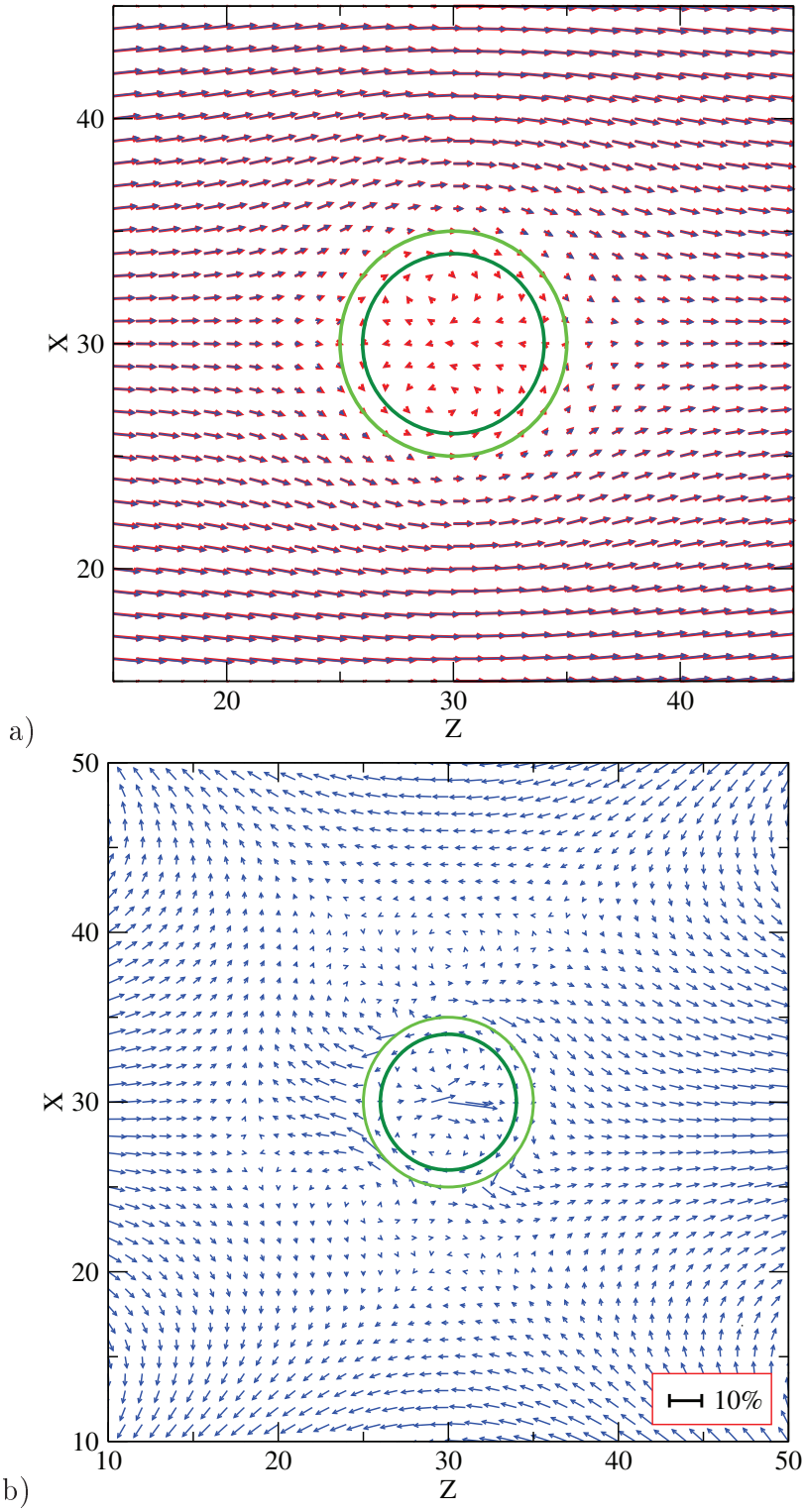

Figure 3.9: a) The velocity fields around the spherical particle in the uniform Stokes flow. b) The relative errors of the velocity field.

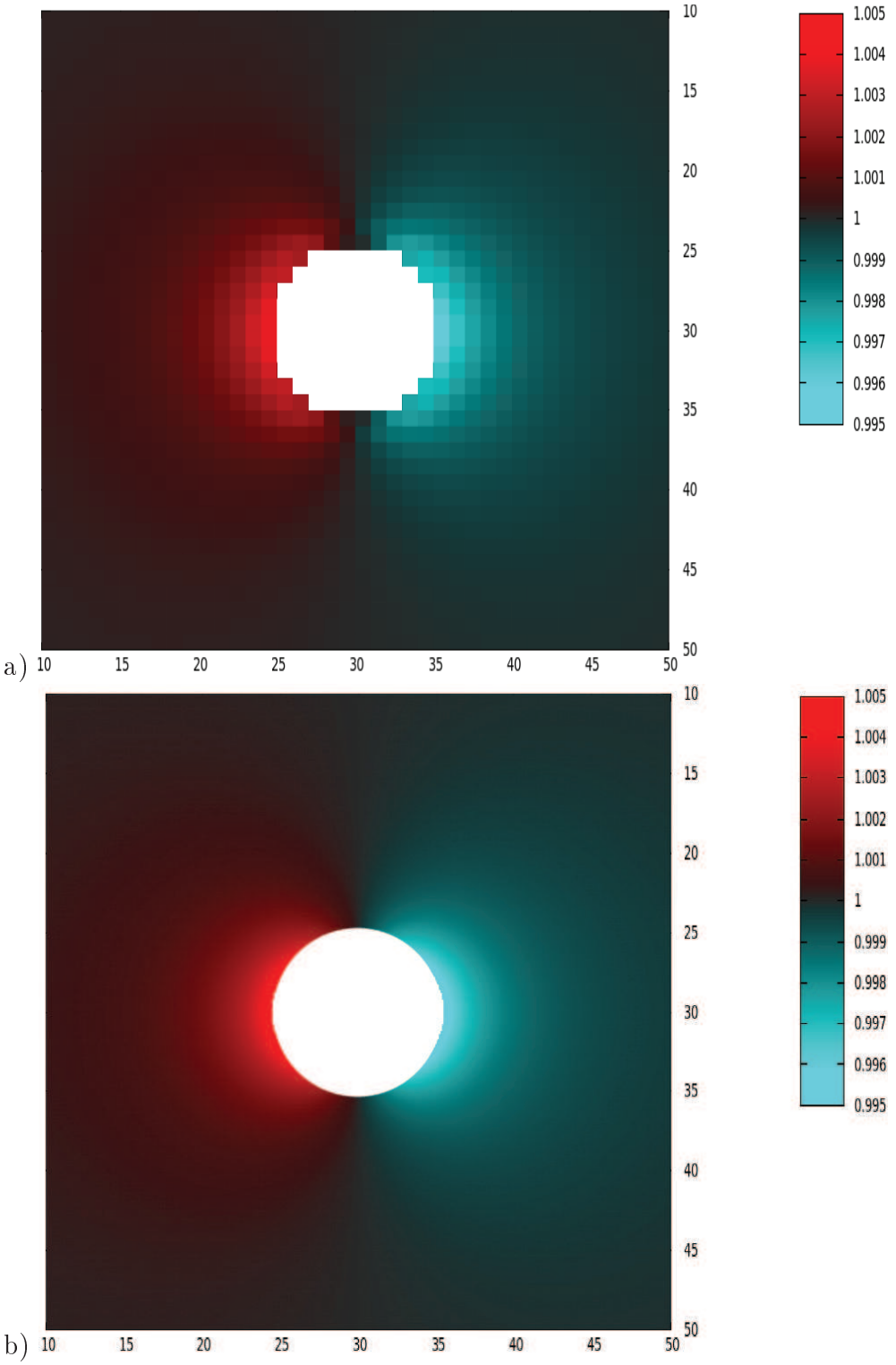

Figure 3.10: The pressure fields around the spherical particle in the uniform Stokes flow. a) numerical result obtained using the FPD method. b) The theoretical prediction.

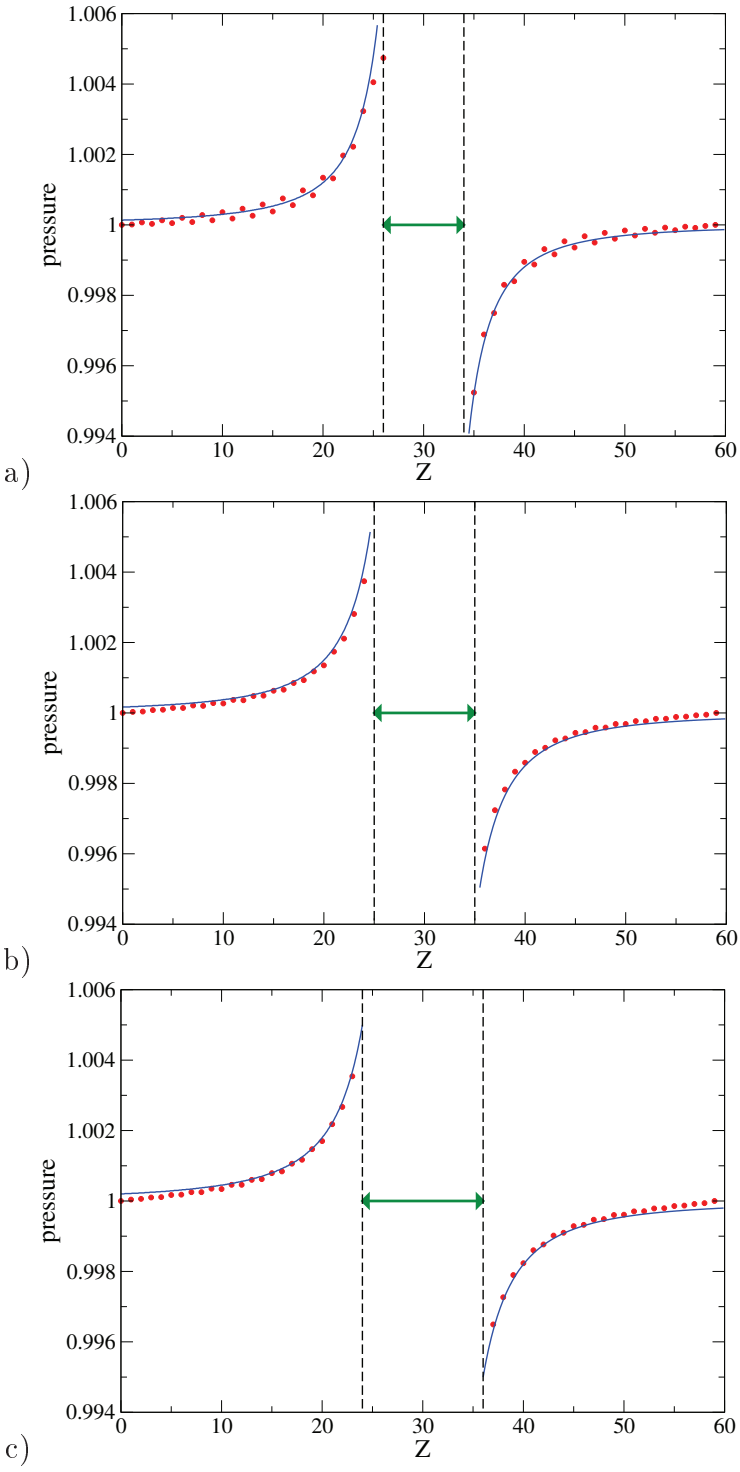

Figure 3.11: Pressure in the middle of the box in the Stokes Flow Past a Sphere. a) $\xi = 0$, b) $\xi = 0.5\delta$, c) $\xi = \delta$.

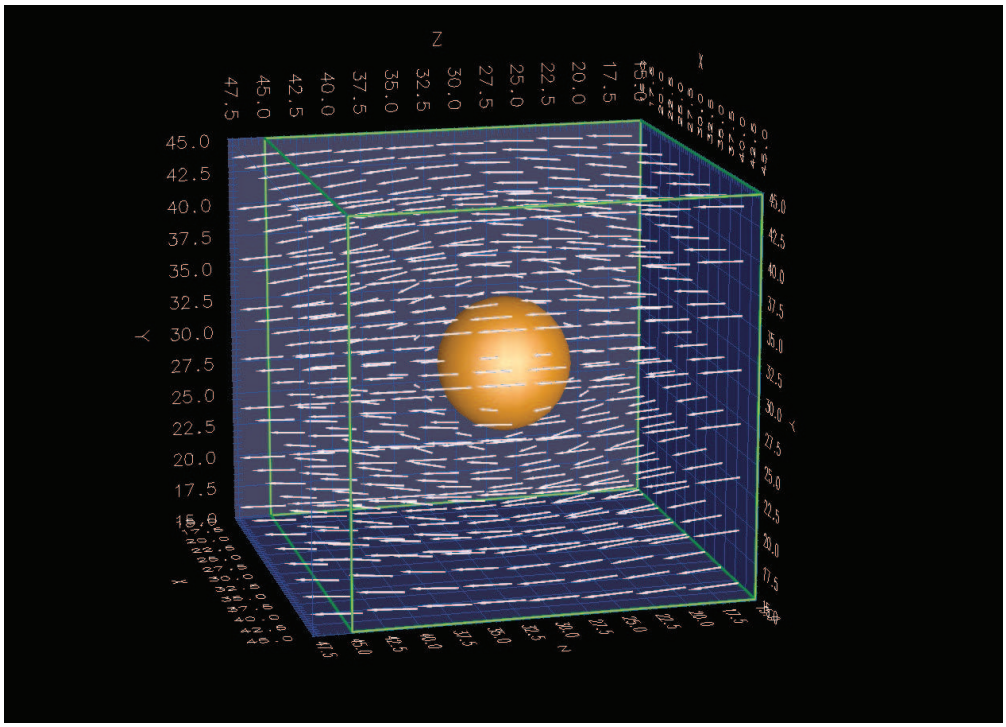

Figure 3.12: Three dimensional view of the velocity fields around the spherical particle in the uniform Stokes flow.

the panel a) red arrows represents numerical results using the FPD method while the blue arrows are plotted using the (3.42) and (3.43) analytical solution. On the panel b) we show the relative errors of the velocity field estimated as following:

$$\epsilon = \frac{|\mathbf{v}_{num} - \mathbf{v}_{the}|}{U},$$

where $\mathbf{v}_{num}$ and $\mathbf{v}_{the}$ are numerical and theoretical velocities, respectively.

The figure 3.10 shows the pressure fields around a spherical particle in a uniform Stokes flow: a) numerical result obtained using the FPD method, b) The exact analytical prediction (3.43) with $u_\infty = 0.02$, $a = 4\delta$, $\xi = 0.5\delta$ and $R_{eff} \simeq r + 2\xi = 5\delta$. On figure 3.11 the pressure is plotted in the middle of the box for three different values of fluid-particle thickness: a) $\xi = 0$; $R_{eff} \simeq 4\delta$, b) $\xi = 0.5\delta$; $R_{eff} \simeq 5\delta$ and c) $\xi = \delta$; $R_{eff} \simeq 6\delta$. The red dots are numerical results and the solid line is plotted using the analytical solution. The double arrow indicates the region occupied by the sphere along

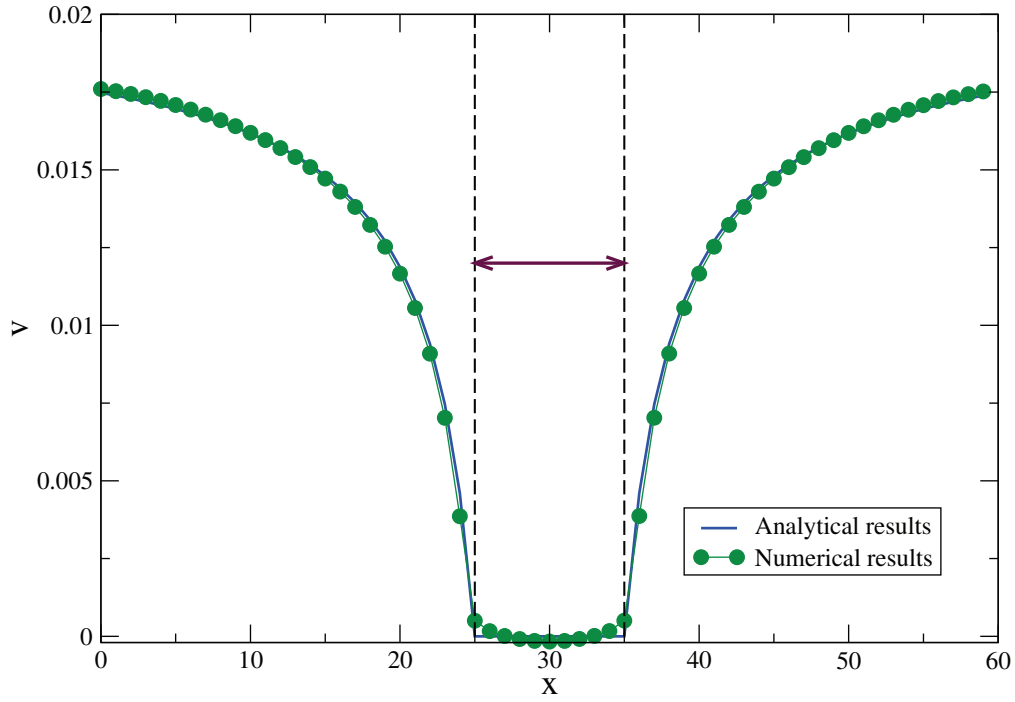

Figure 3.13: The velocity profile along $x-$ axis for a Stokes flow past a sphere.

z. On figure 3.13 the velocity profiles is shown along x axis for a Stokes flow past a sphere. The numerical results (full circles) are compared to the analytical results (solid curve) outside of the sphere calculated using equations (3.42-3.43).

To illustrate how the viscosity contrast represents the solid-like nature of the fluid particle in the FPD method on figure 3.14 we show the velocity fields of Stokes flow past a sphere calculated using FPD method for different values of the viscosity ratio between inside and outside of the bead: a) $\eta_p/\eta = 1$, b) $\eta_p/\eta = 3$, c) $\eta_p/\eta = 10$ and d) $\eta_p/\eta = 100$. The velocity of the flow is $U = 0.02$, radius of bead $a = 6\delta$ and $\xi = 0.5\delta$. As we can see on figure 3.14 d) and figure 3.9 a) for the high viscosity contrast the flow field is very similar to those for a solid particle. While there are some recirculation of the flow inside the particle for small viscosity ratios (3.14 a) and b)).

Note that our code is able to handle zero fluid-particle interface thickness ($\xi = 0$). However, some small oscillations appear in the numerical values of the pressure as shown in figure 3.10 a. That is the reason why we choose for all our simulations the value $\xi = 0.5\delta$ which ensures the most reliable velocity and pressure fields.

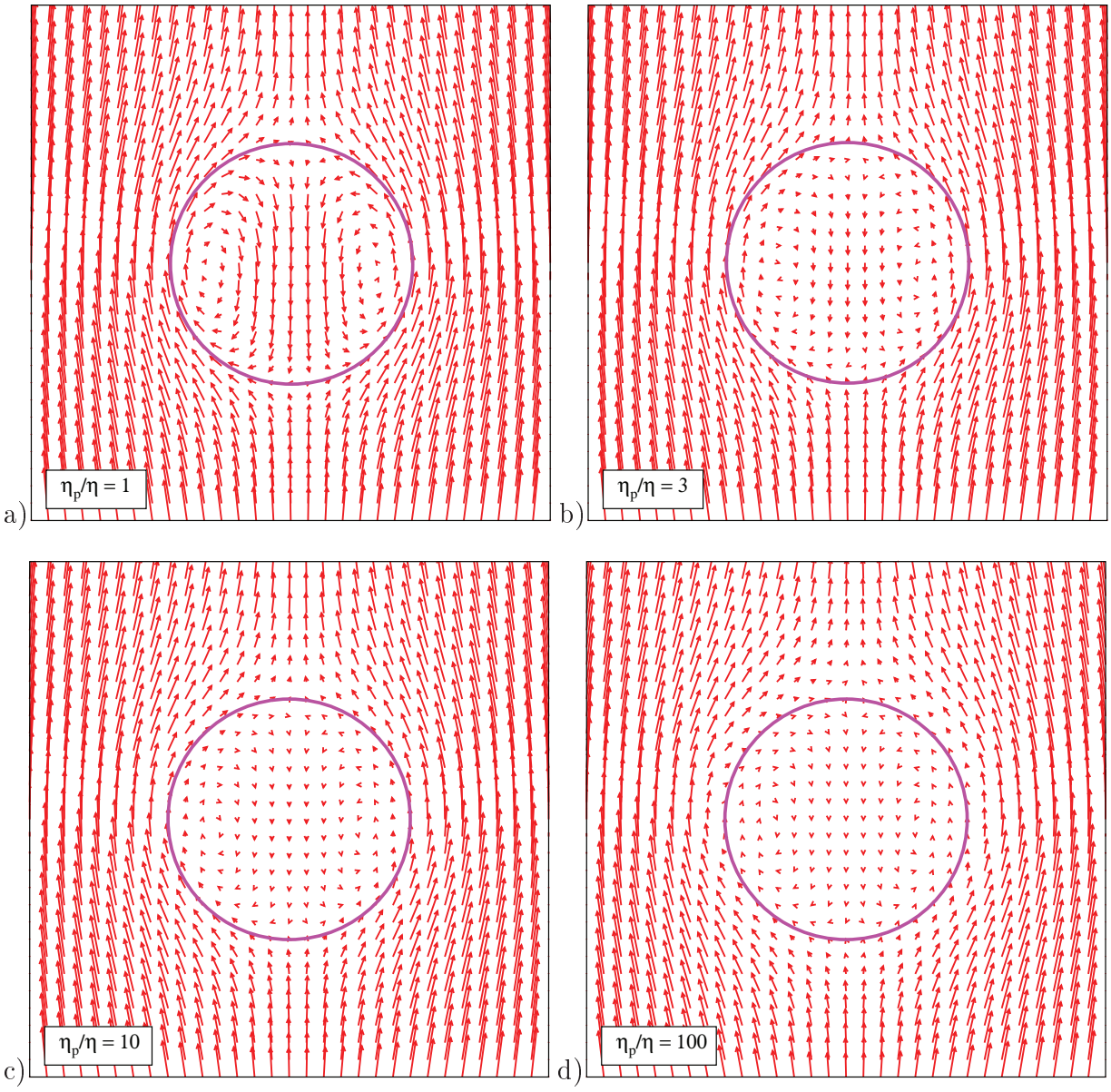

Figure 3.14: The velocity fields of Stokes flow past a sphere for different viscosity contrast.

3.8.2 Spherical particle in a shear flow

An another important example to compare our numerical result to the well known exact theoretical solution is the shear flow around a rigid spherical particle at zero Reynolds number. The solutions for the velocity components (u, v, w) and pressure for the shear flow around a sphere in Cartesian coordinates have the following form [52]:

$$u = \dot{\gamma}\left\{\frac{x}{2}\left[1-\frac{1}{r^5}\right]+\frac{x}{2}\left[1-\frac{1}{r^3}\right]-\frac{5}{2}\frac{z^2x}{R^2}\left[\frac{1}{r^5}-\frac{1}{r^7}\right]-\frac{\Omega x}{r^3}\right\}, \tag{3.45}$$

$$v = \dot{\gamma}\left\{\frac{z}{2}\left[1-\frac{1}{r^5}\right]-\frac{z}{2}\left[1-\frac{1}{r^3}\right]-\frac{5}{2}\frac{zx^2}{R^2}\left[\frac{1}{r^5}-\frac{1}{r^7}\right]+\frac{\Omega z}{r^3}\right\}, \tag{3.46}$$

$$w = -\dot{\gamma}\frac{5}{2}\frac{xyz}{R^2}\left[\frac{1}{r^5}-\frac{1}{r^7}\right]. \tag{3.47}$$

and

$$p = p_\infty - \frac{6\dot{\gamma}xz}{R^2r^5} \tag{3.48}$$

Where

$$r = \sqrt{\frac{x^2}{R^2}+\frac{y^2}{R^2}+\frac{z^2}{R^2}},$$

$\dot{\gamma}$ is the shear rate, p_∞ is the pressure far enough from particle, R is the radius of particle and

$$\Omega = -\frac{\omega_z}{\dot{\gamma}}, \tag{3.49}$$

here ω_z denotes the angular velocity of a rigid sphere in the shear flow. If a spherical particle is free in the shear flow then it rotates with the angular velocity $\omega_z = -\dot{\gamma}/2$, so $\Omega = 1/2$. When particle is not rotating in the shear flow (for example in the presence of an external counter torque) the angular velocity ω_z can be equal to zero and therefore $\Omega = 0$. On the contrary if Ω is increased, (using external torque) we can obtain angular velocity $\omega_z = -\dot{\gamma}$ and $\Omega = 1$ for example. To compare the result obtained with FPD method to the analytical one for a spherical particle in a shear flow, we took three-dimensional [60][60][60] simulation box and imposed a shear flow in ZOX plane (see 3.4) with the shear rate $\dot{\gamma} = 0.02$ with a spherical particle with radius $a = 4\delta$ and $\xi = 0.5\delta$, ($R_{eff} \simeq a + 2\xi = 5\delta$) placed in the middle of the box. The fluid velocity on the boundary plates of the box (perpendicular to x axis) is constant, so the shear rate is fixed during the simulation. To stop or enhance the rotation of particle in shear flow

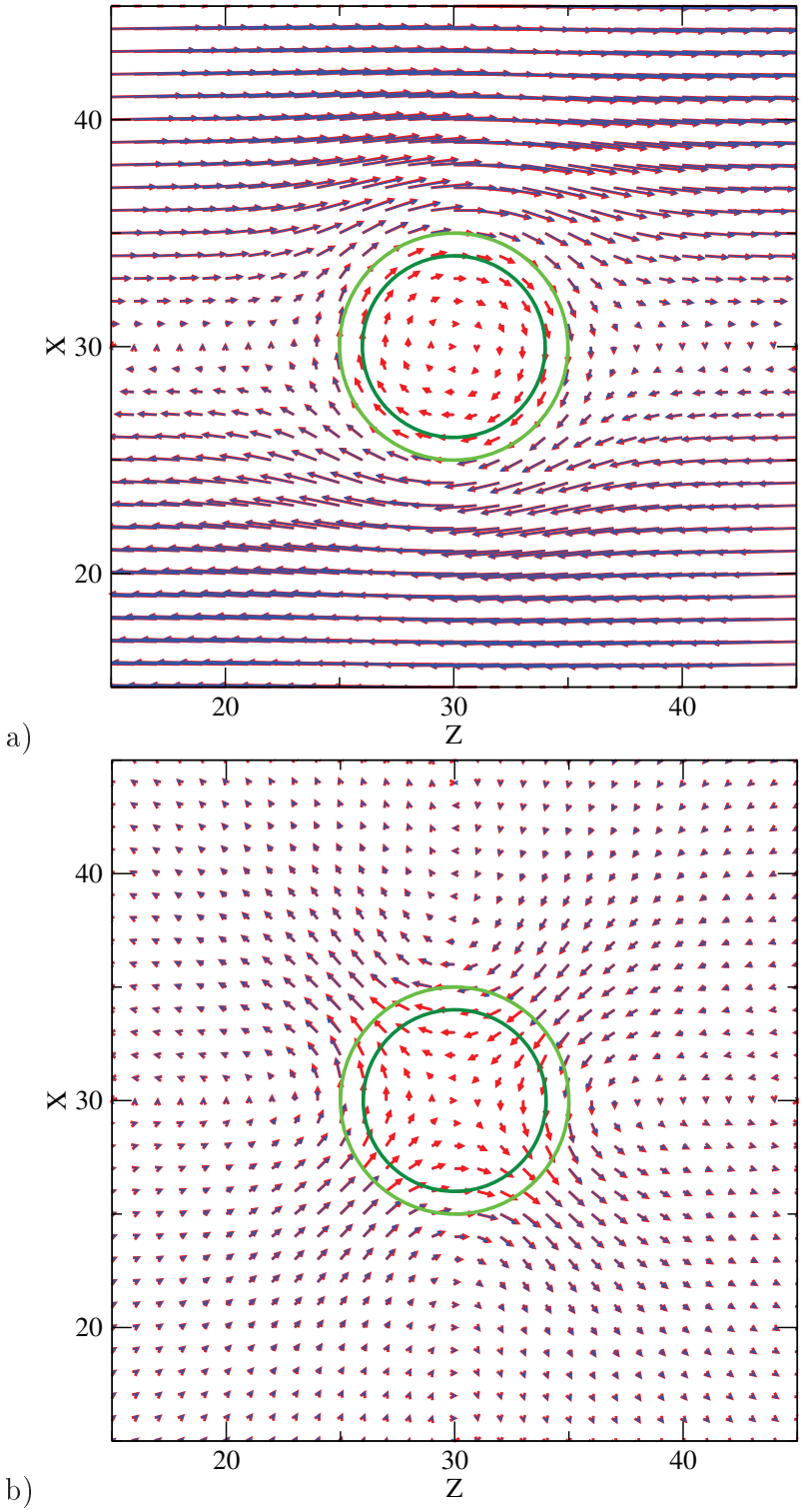

Figure 3.15: a) The full velocity field around the spherical particle in a shear flow. b) The disturbance of the velocity fields. $\Omega = 1/2$.

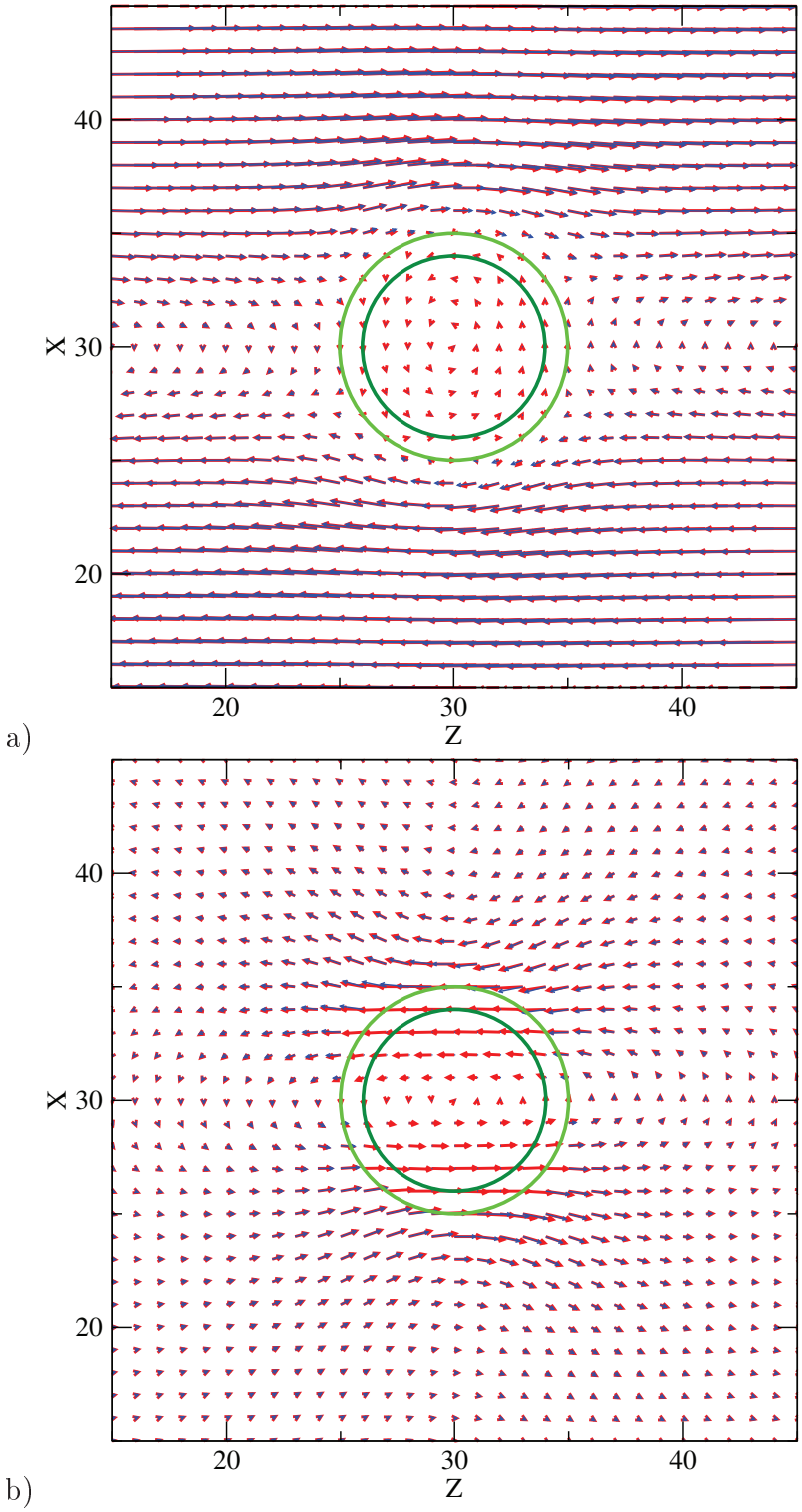

Figure 3.16: a) The full velocity field around the spherical particle in a shear flow. b) The disturbance of the velocity fields. $\Omega = 0$.

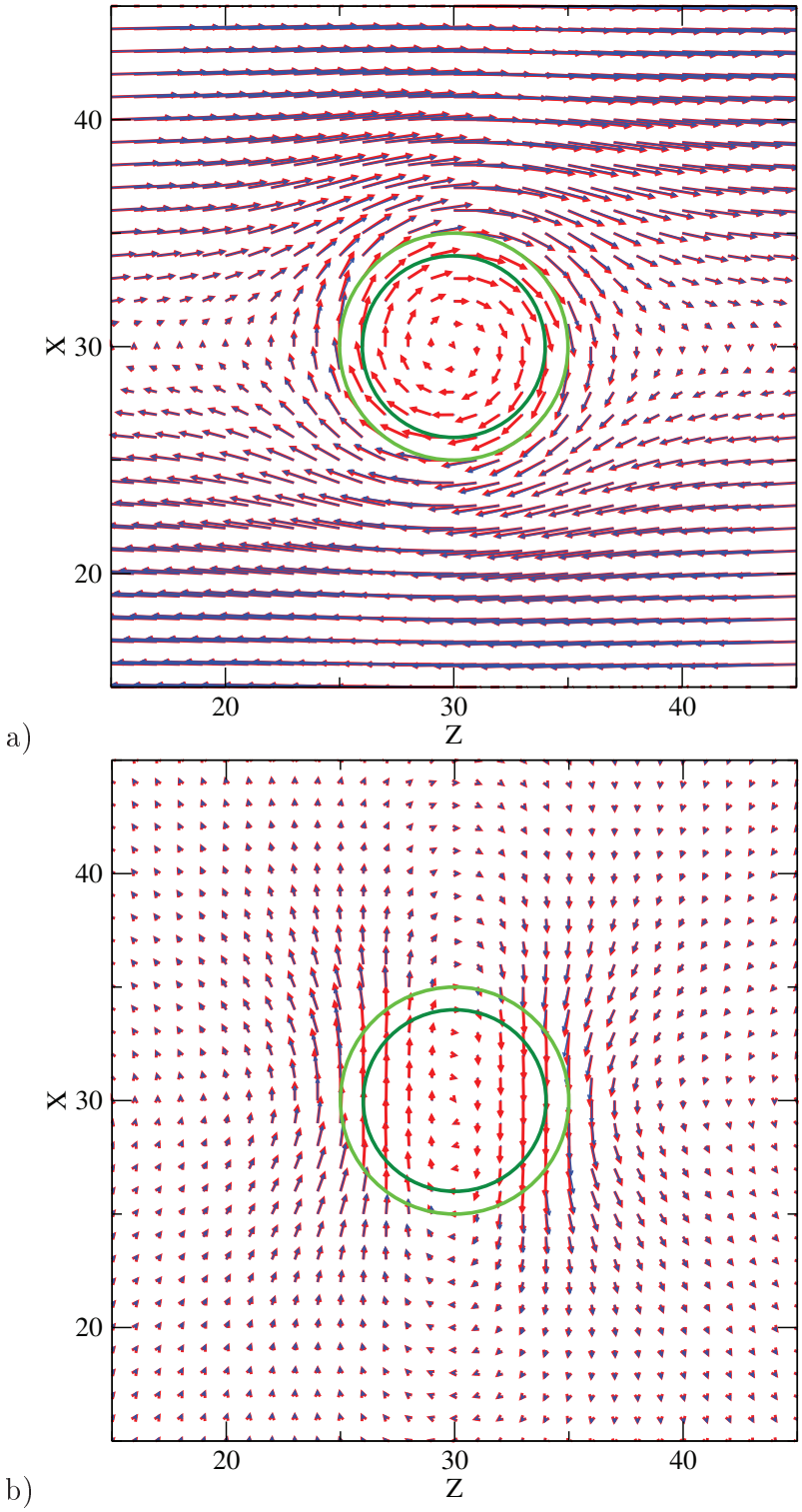

Figure 3.17: a) The full velocity field around the spherical particle in a shear flow. b) The disturbance of the velocity fields. $\Omega = 1$.

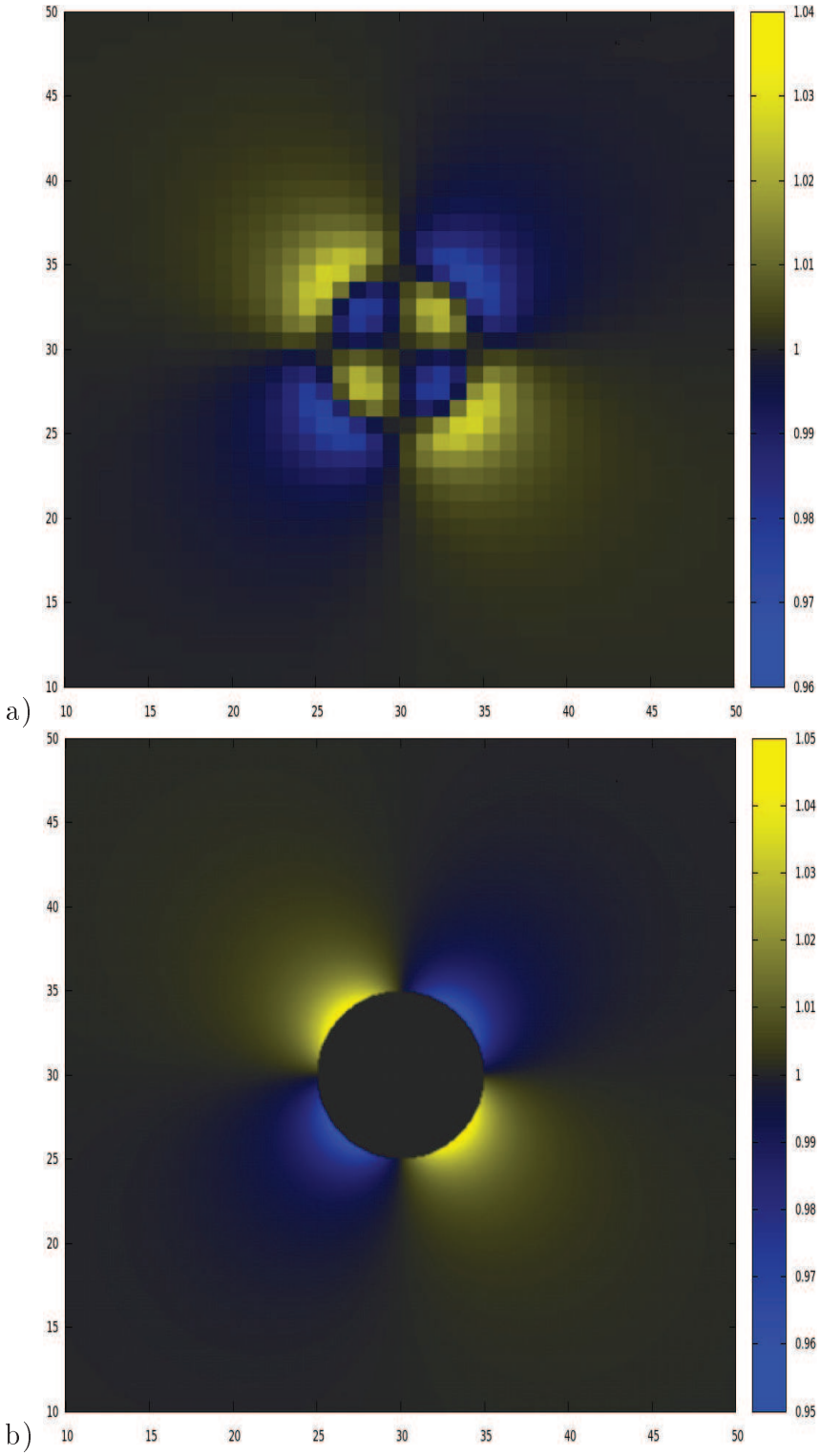

Figure 3.18: The pressure fields around the spherical particle in the shear flow. a) Numerical result of the FPD method. b) The analytical prediction.

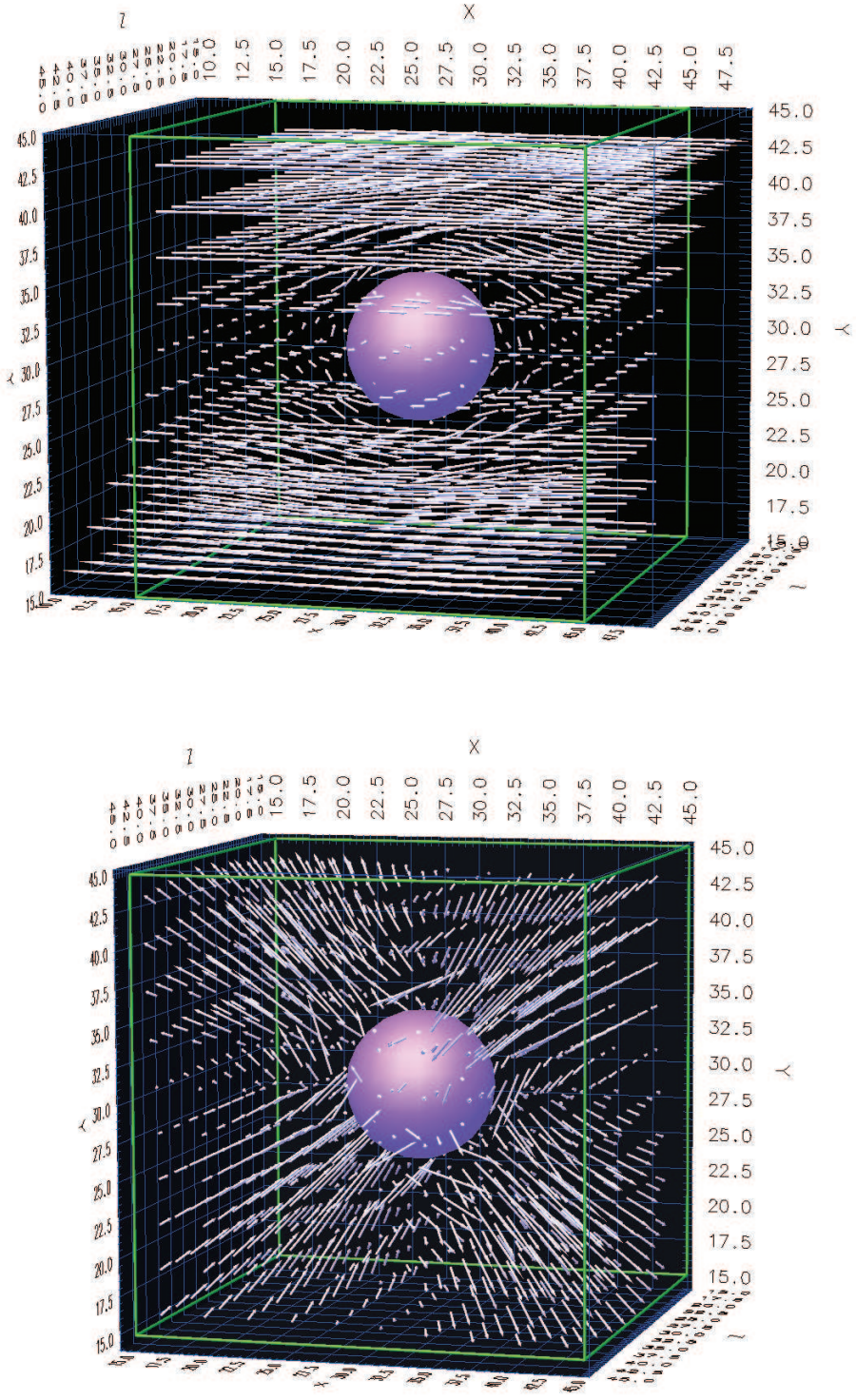

Figure 3.19: a) Three dimensional view of the velocity fields around the spherical particle in the shear flow. b) The disturbance of the velocity field.

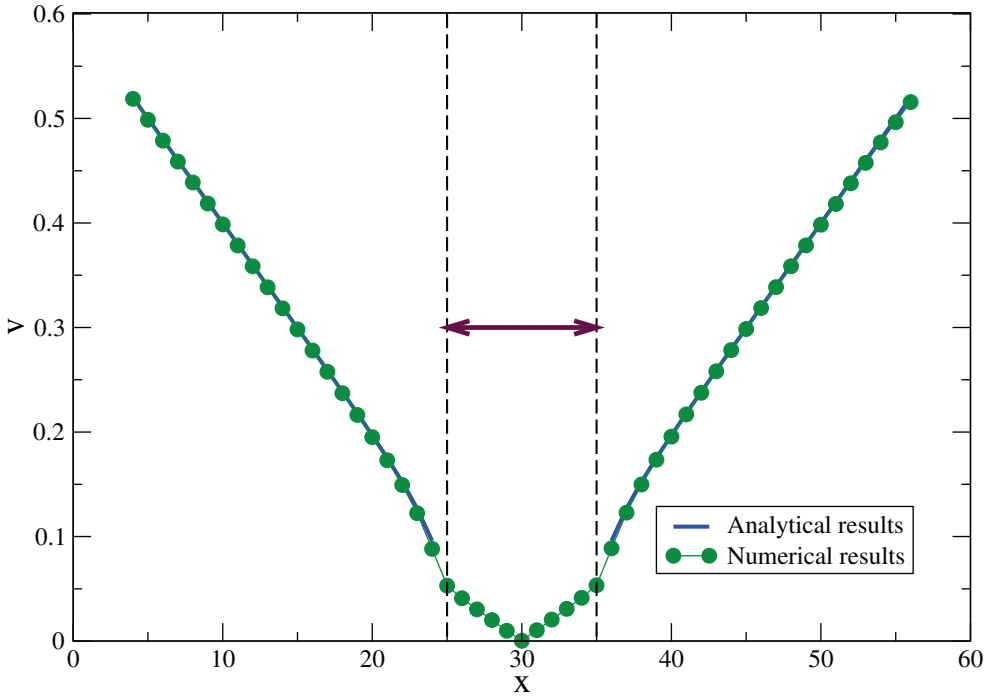

Figure 3.20: The velocity profile along the $x-$ axis for a sphere in the shear flow.

we applied force quadrupole on the particle (see details in chapter 5).

In figures 3.15, 3.16 and 3.17 it is shown two different representations of two velocity fields for a spherical particle in a shear flow for three values of the angular velocity: $\Omega = 1/2$, $\Omega = 0$ and $\Omega = 1$, respectively. Red arrows presents the velocity field obtained using the FPD method and the blue arrows corresponds to the velocity field plotted using analytical expressions (3.45) and (3.46). The radius of the particle is $a = 4\delta$, the fluid-particle interface thickness $\xi = 0.5\delta$ and the effective radius $R_{eff} \simeq a + 2\xi = 5\delta$. On figures 3.15, 3.16 and 3.17, a) shows the fluid velocity fields while b) shows disturbances of the velocity fields of the shear flow due to the presence of the particle ($\mathbf{v}' = \mathbf{v} - \dot{\gamma}x$). Figure 3.20 shows the velocity profiles $v = \sqrt{u^2 + v^2 + w^2}$ along x axis for a sphere in the shear flow. The numerical results (full green circles) are compared to the analytical results (solid curve) outside of the sphere obtained using equations (3.45-3.47). The pressure fields around the spherical particle in the shear flow obtained using the FPD method is compared to the theoretically predicted one plotted using the equation (3.48) on the figure 3.18. On figure 3.19, we show three dimensional views of

the numerically obtained velocity around the spherical particle in the shear flow and the disturbances of the velocity fields of shear flow for the parameters given above.

Note that the numerical method shows the velocity and pressure distribution even inside the particle since the viscosity of the particle in the simulation is finite ($\eta = 1$; $\eta_p = 100$) while the analytical expressions (3.48) predicts the pressure only outside of the particle.

3.8.3 Collision between two spheres

Another test of the method is the simulation of the collision between two spheres in a symmetric shear flow $zOx-$plane (figure 3.21). It allows to test the contact events between two particles as well as the reversibility of the Stokes equation. The two spheres are initially moving toward each other, symmetrically positioned along the $z-$ axis with respect to the line $v_z = 0$. The initial x inter-distance between the particle centers is the impact parameter noted b. Of course, when they are very close, the two spheres are not in true physical contact at any time: a thin layer of fluid is clearly visible on figure 3.21. When the two spheres collide (if $b < 2R$), they form a doublet. This doublet rotates around the $y-$ axis, its orientation is defined by the angle φ. Initially, when the two spheres come into contact, (at $\varphi = \varphi_0$ which depends on b) the doublet is rotating as a rigid system at a certain angular velocity. Then for $\varphi = -\varphi_0$ the two sphere separate. Separation and contact as well as the spheres trajectories before and after $\varphi = 0$ are the mirror images of each other through the plane $z = 0$ simply reflecting the Stokes equation reversibility in the case of rigid spheres. The angular velocity of the doublet is not constant but increases to a maximum at $\varphi = 0$. Following the work of Bartok & Mason [53], we compare the doublet rotation $[\varphi(t)]$ to the Jeffery orbit [54] of an ellipsoid of revolution with an axis ratio of 2:

$$tan(\varphi) = 2tan\left(\frac{2\dot{\gamma}t}{5}\right). \tag{3.50}$$

Figure 3.21 shows the collision between two identical spheres in a shear flow. a) $b = 5\delta$ and $R = 3\delta$ ($a = 2.5\delta$, $\xi = 0.5\delta$). b) $b = 8\delta$ and $R = 5\delta$ ($a = 4\delta$, $\xi = 0.5\delta$). The upper sphere is going to the right while the lower one is going to the left. The inset show the doublet when the spheres are in contact. The dotted-line circles represent the

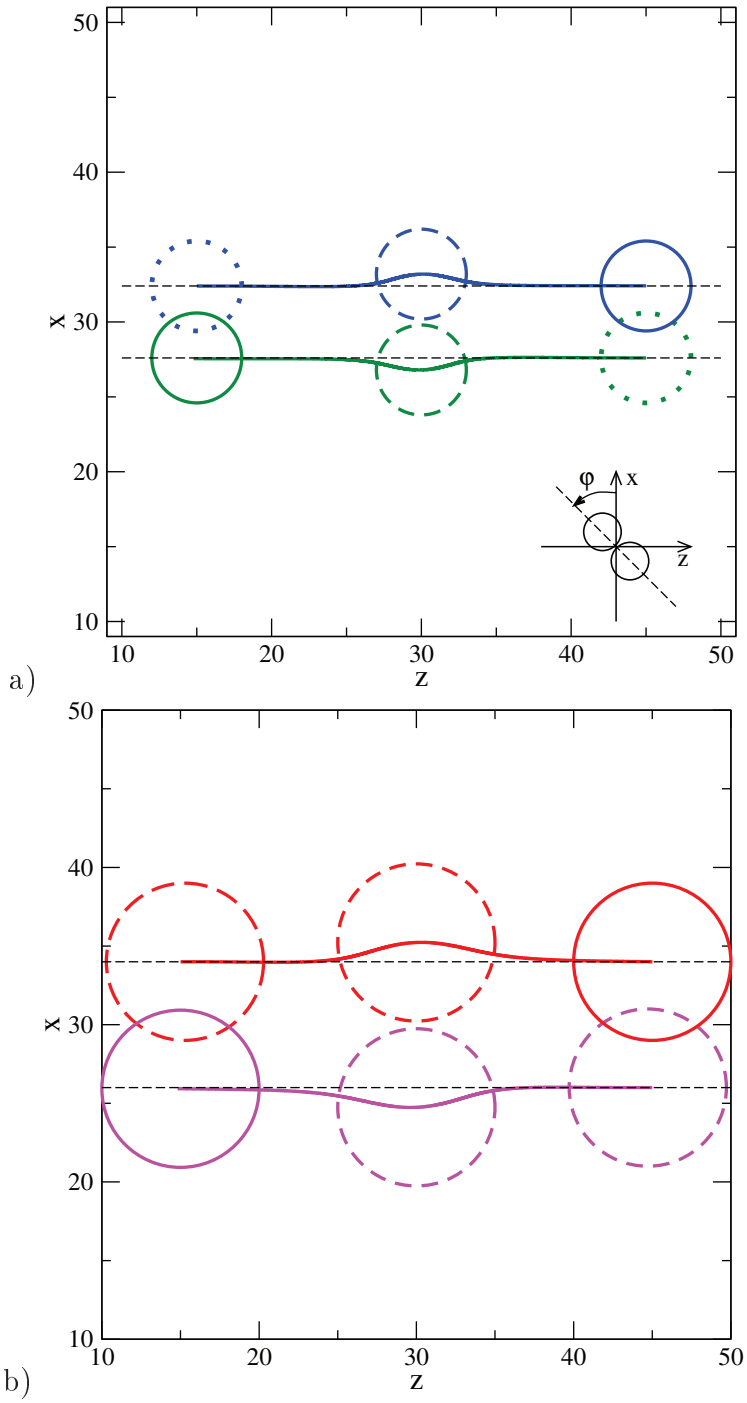

Figure 3.21: The collision between two identical spheres in a shear flow. a) $b = 5\delta$ and $R = 3\delta$. b) $b = 8\delta$ and $R = 5\delta$.

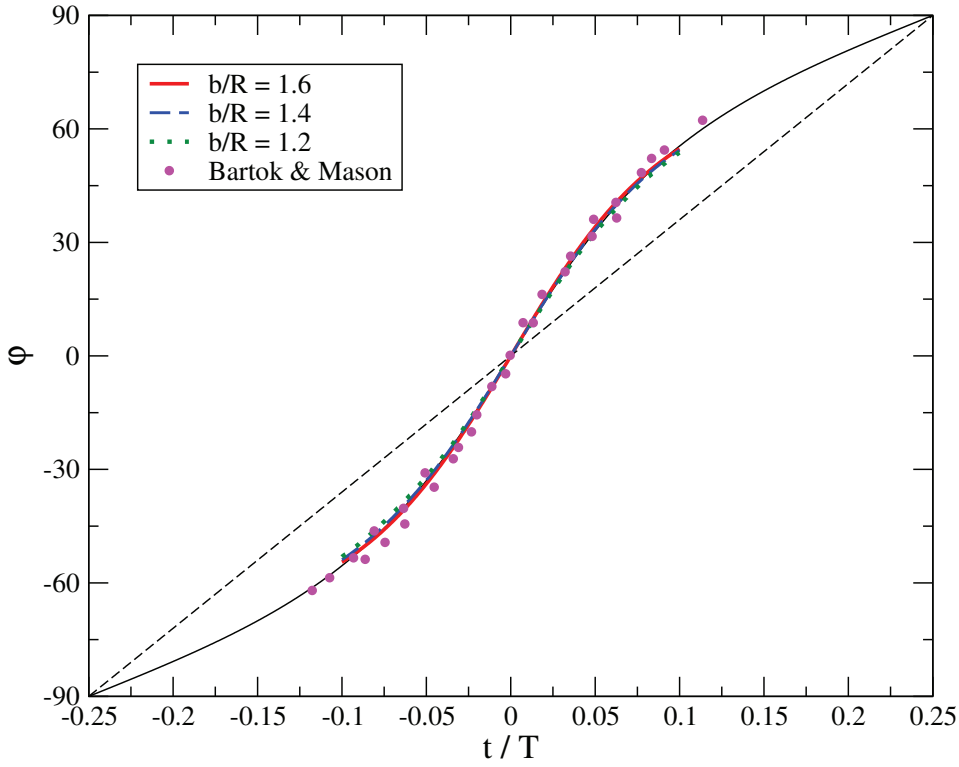

Figure 3.22: The variation of φ with time for different impact parameters and compared to equation (3.50) as well as experimental results of Bartok & Mason [53].

initial positions of the spheres at time $t = -t_0$. The dashed-line circles represents the spheres at $t = 0$ and the solid-line circles at a time $t = t_0$. The two curves represents the trajectory of the sphere centers. One can see that the $x-$distance between the two spheres is identical for $t = \pm t_0$, this is due to the reversibility of the Stokes equation in the case of rigid spheres. Figure 3.22 shows an excellent agreement between our numerical results, the law (3.50) and the experimental values of Bartok & Mason [53]. On this figure, time is conventionally fixed to $t = 0$ when the doublet is vertical (along the $x-$ axis, i.e. $\varphi = 0$).

3.8.4 Ellipsoidal particle in the shear flow

The motion of an ellipsoidal particle in a shear flow of a Newtonian fluid was studied by Jeffery in 1922 [54]. The exact analytical solution for the orbit of ellipsoid of revolution

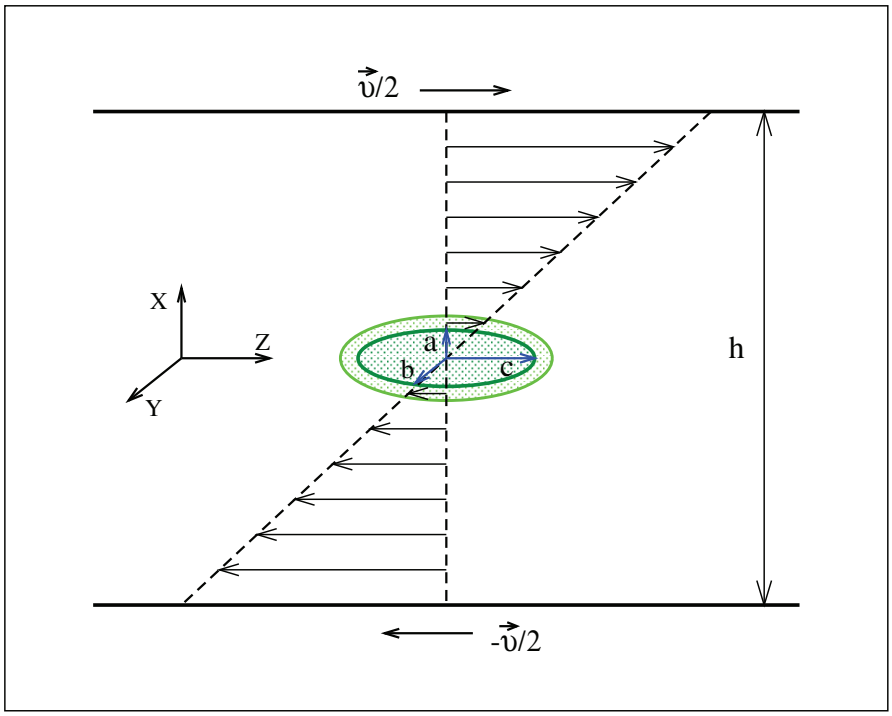

Figure 3.23: The ellipsoidal particle in the shear flow.

in shear flow at zero Reynolds number has the following form:

$$tan(\varphi) = \frac{a}{b}\, tan\left(\frac{\dot{\gamma} abt}{a^2 + b^2}\right), \tag{3.51}$$

where φ is the angle of orientation a, b and c ($b = c$) are semi-axes of ellipsoid,$\dot{\gamma}$ denotes the shear rate and t is the time. To compare orbit of rotation obtained by the FPD method to the Jeffery's orbit defined by equation (3.51), we put the prolate spheroid in the middle of the simulation box where the shear flow is imposed with the shear rate $\dot{\gamma} = 0.02$. The semi-major axis a is initially parallel to the z axis, the semi-minor axis b is directed along x ($c = b$) (see the figure 3.23). The figure 3.23 shows the schematic diagram of the ellipsoidal particle in the shear flow with $\dot{\gamma} = 0.02$, $a = 5$, $b = c = 2$ and $\xi = 0.5$. The orientation angle φ is defined in the range $(-\pi/2; \pi/2)$ using the equation (3.51) while the angle of orientation φ_1 obtained from the simulation, $\varphi_1 = arccos(\alpha_x)$ is defined in the domain $(0; \pi)$, here α_x is x component of the unit vector along the semi-minor axis a. We decompose both orientation angles in the interval $(0; \pi/2)$ in

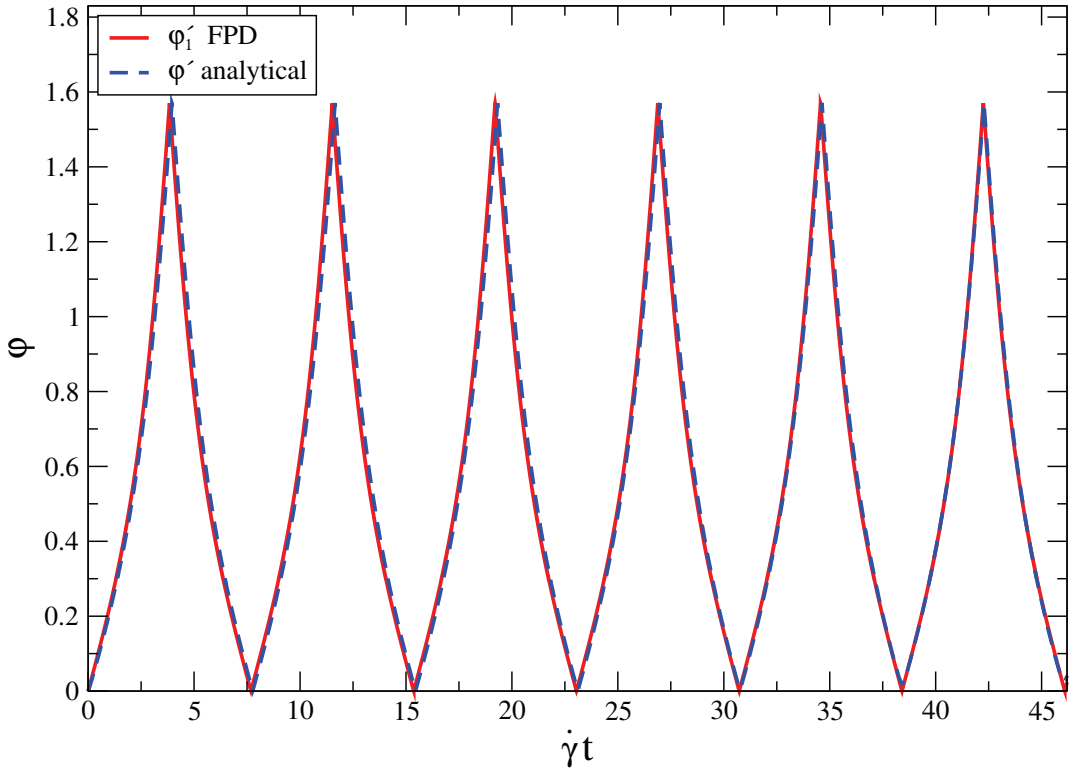

Figure 3.24: Comparison between the Jeffery's orbit and the one obtained using the FPD method.

order to compare the numerically obtained result and the analytical prediction.

$$\varphi' = \left| arctan\left[r_e.tan\frac{\dot{\gamma} r_e t}{r_e + 1/r_e} \right] \right|, \quad \varphi' \in (0;\, \pi/2) \tag{3.52}$$

$$\varphi_1' = \left| \frac{\pi}{2} - \left| arccos(\alpha_{\mathbf{x}}) - \frac{\pi}{2} \right| \right|, \qquad \varphi_1' \in (0;\, \pi/2) \tag{3.53}$$

here r_e is the ratio between the major and minor axis of an ellipsoid of revolution.

The figure 3.24 shows comparison between the numerically obtained orbits of ellipsoid using the FPD method to the Jeffery's orbits defined using the equation (3.51). The solid red line φ_1' defined in the interval $(0;\, \pi/2)$ represents the numerical result. While the dashed blue line φ' defined in the same interval corresponds to the Jeffery's orbit with $r_e = 0.518$. The semi-axes are $a = 5\delta$; $b = c = 2\delta$, the particle fluid interface thickness is $\xi = 0.5\delta$ and shear rate is $\dot{\gamma} = 0.02$. The ratio between the major and

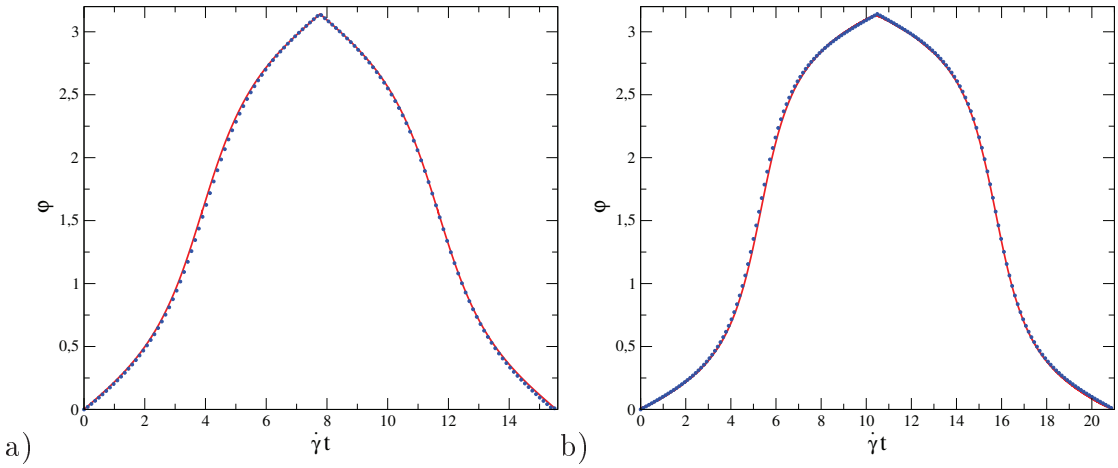

Figure 3.25: Jeffery's orbits a) $r_e = 0.5$ and $r_e^J = 0.518$. b) $r_e = 2/7$ and $r_e^J = 0.33$.

minor axis r_e in equation (3.52) fits the numerical result if $r_e^{th} = 0.518$, which is close to the expected one,

$$r_e = \frac{a + 2\xi}{c + 2\xi} = \frac{2 + 2 \times 0.5}{5 + 2 \times 0.5} = 0.5.$$

The orientation angle for rotation of prolate spheroid under shear as a function of time are shown in figure 3.25. The red curves represents the Jeffery's orbit defined in the interval $(0; \pi)$. The blue dotted lines are the result of our simulations using the FPD method. The shear rate $\dot{\gamma} = 0.02$. a) $a = 5\delta$; $b = c = 2\delta$; $\xi = 0.5\delta$; $r_e = 0.5$ and $r_e^J = 0.518$. b) $a = 6\delta$; $b = c = \delta$; $\xi = 0.5\delta$; $r_e = 2/7 = 0.286$ and $r_e^J = 0.33$, where r_e^J is the ratio between the major and minor axis used in equation (3.52).

3.9 Conclusion

In this chapter, we described the Fluid Particle Dynamic method (FPD). In the introduction (section 3.1), we reviewed some background and utilization of the method as well as its positive and negative aspects. In the section 3.2, we introduced the main theory behind the FPD method. In the next section 3.3, we considered the projection method which is integrated with the FPD method. Then, in section 3.4, we introduced the MAC grid and some details of the discretization. In the next section 3.5, we wrote down the numerical procedure of the FPD method and present the basic flow chart

of the algorithm. In the section 3.6, we selectively considered determination of the volume fraction. In the next section 3.7, we briefly listed number of changes and possible extensions made in the FPD method. Then in the section 3.8, we presented some canonical examples obtained using the FPD method in comparison with well-known analytical results. Namely, Stokes flow past a sphere, a spherical particle in the shear flow, collision between two spheres and Jeffery's orbit for ellipsoidal particles in the shear flow. These examples show very good agreements with the corresponding exact analytical solutions which provides additional reliability of the FPD method.

Now that we are convinced about the reliability of the FPD method, in the next chapters, we will extensively use this method to solve several different problems (a confined sphere in a shear flow: chapter 4; a suspension in the presence of torque chapter 5; suspension of micro swimmers chapter 6).

Chapter 4

The effect of confinement on the rotation of a spherical particle in a shear flow

In this chapter, we numerically examine the role of particle-wall interactions for a single spherical particle in a Newtonian fluid being confined and submitted to a simple shear flow at low Reynolds numbers. We show that particle-wall interactions decrease the rotational velocity of the sphere in the shear flow. We also show that in a unconfined shear flow the presence of the wall in the vicinity of a particle *decreases* as well the rotational velocity and changes the translational velocity of the particle so that the difference between velocity of the particle and the velocity of the wall decreases. All simulations are performed in 3D. Our numerical results are compared with another theoretical and numerical works, a very good agreement is found with [55, 56, 18, 57, 58] and disagreement with [59].

Dans ce chapitre nous examinons numériquement le rôle des interactions particule-paroi pour une seule particule sphérique dans un fluide Newtonien confinée entre deux parois et soumise à un simple écoulement de cisaillement à faible nombre de Reynolds. Nous montrons que l'interaction particule-paroi fait diminuer la vitesse de rotation de la sphère. Nous montrons également que dans un cisaillement non confiné en présence d'une seule paroi, une particule proche de la paroi voit diminuer sa vitesse de rotation ainsi que la différence entre sa vitesse de translation et la vitesse de la paroi. Toutes les simulations sont réalisées en 3D. Nos résultats numériques sont comparés avec des travaux théoriques et numériques, un très bon accord est trouvé avec [55, 56, 18, 57, 58] et de désaccord avec [59].

4.1 Introduction

Quite often, in microfluidic devices used in biochemical and biomechanical processes (to study blood samples, bacteria, micro-swimmers etc.) one or more dimensions of a

micro-channel are comparable with the size of the objects in this channel. In such cases an effect of the finite dimension of the channel on the flow fields and motion/rotation of particles becomes important. Note that the effect of confinement on a sheared rigid object is similar to geological processes: tectonic shortening of deep-seated rocks to shallow levels in the lithosphere [60, 61], the dispersion of agglomerated fillers [62].

The behavior of a spherical particle in an infinite shear flow is very well described analytically [54]. The spherical particle experiences a uniform rotation with an angular velocity $\omega_y = \pm\dot{\gamma}/2$, where $\dot{\gamma}$ is the shear rate.

In the case where a two walls moving with equal but opposite velocities $\mathbf{v}$ are touching the spherical bead (the sphere diameter is equal to the gap size between the walls) the tangential velocity of the bead is the same as the velocity of walls, so the angular velocity of the bead is $\omega_y = \pm\dot{\gamma}$ [59] (see figure 4.1).

The effect of finite dimension on the rotation of a single spherical particle under shear flow was numerically investigated by Bikard et al. [55] using Rem3D finite element method. They found that proximity of the particle and walls increases the rotational period of the sphere but because of the numerical convergence problems they did not reach the sticking contact between the sphere and the walls. The similar behavior was found by D'Avino et al. [56] using the finite element method. However, an opposite effect was obtained by Pomchaitawarda et al. [59]. They observed an enhancement of the angular velocity of the sphere when reducing the gap size. Pomchaitawarda et al. used a cone-and-plate shearing device. However, they report in the limit cases that $\omega_z = -\dot{\gamma}$ with a sticking contact between the sphere and the walls and $\omega_z = -\dot{\gamma}/2$ in an unconfined flow.

We make numerical simulations using FPD method (discussed in chapter 3) and found that by decreasing the gap size between spherical particle and walls while the particle is getting closer to the walls, the absolute value of the angular velocity of the particle is decreasing. The result is in very good agreement with the result of Bikard et al. [55] as well as results of D'Avino et al. [56] and analytical calculations of Sangani et al. [18] but our result is in disagreement with the measurement of Pomchaitawarda et al. [59].

We also investigate the effect of a singe wall on the rotation and movement of the spherical particle. When the particle is close to the wall in the shear flow, ro-

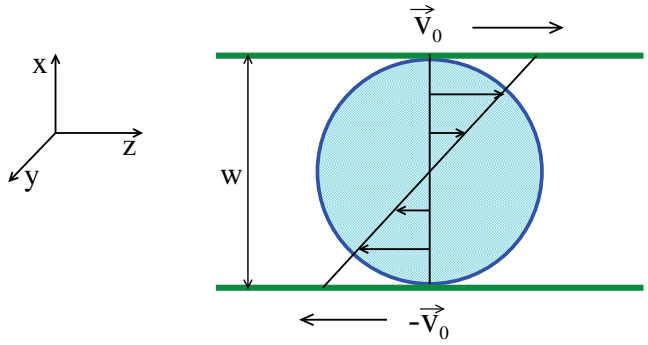

Figure 4.1: Schematic diagram of a spherical particle with sticking contact to walls in shear flow.

tational velocity of the particle decreases and the translational velocity of the particle increases/decreases so that the difference between the velocity of the particle and the velocity of the wall decreases in comparison to the velocity (rotational and translational) of the flow. Our results are compared with the literature and a good agreement is found with the theoretical work of Goldman et al. [57] and experimental observations of Darabaner et al. [58].

In the following section, we consider parameters used in the numerical method. Then in section 4.3, we show our numerical results in comparison to the ones of other authors, we give an interpretation of our results, the velocity fields around a spherical particle in a shear flow for different confinements. We conclude in section 4.4.

4.2 Numerical consideration

In order to study the effects of confinement and presence of walls on the dynamics of a single spherical particle in a shear flow, we use the "fluid particle dynamics" FPD (see details in Chapter 3). The particle is considered large enough and the Brownian motion is not taken into account. The density of the particle and of the solvent is equal, so the effect of gravity is neglected. A spherical particle with viscosity η_p is placed in a Newtonian liquid of viscosity η sheared between two walls. The simulation box size is $\ell_y = \ell_z = 60\delta$ and $13\delta \leq \ell_x = w \leq 60\delta$, here, $\delta = 1$ is the mesh size. The spherical particle is placed at the center of the simulation box (see figure 4.2). The two walls

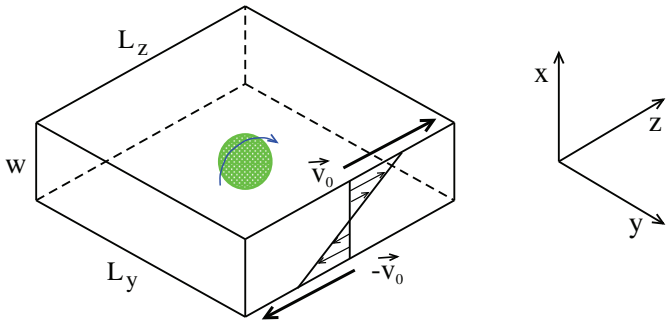

Figure 4.2: Schematic representation of the simulation box around spherical particle in a shear flow.

located at $x = \pm w/2$ move with $v_z = \pm v_0$ velocities,

$$v_z(x = \pm\frac{w}{2}, y, z) = \pm v_0 = \pm\frac{\dot{\gamma} w}{2}$$

respectively, such that the constant shear rate ($\dot{\gamma} = 0.025$) is maintained for different values of w. The periodic boundary conditions are used along y and z directions, while fixed velocities are imposed to the walls. No-slip conditions are used at the fluid/walls interface.

The time step for each numerical iteration is $\delta t = 0.001$. A typical size of particle used in the simulations is $a = 4\delta$, the fluid-particle interface thickness $\xi = 0.5\delta$, and the effective radius of particles $R \simeq a + 2\xi = 5\delta$. The small Reynolds number is such that:

$$Re = \frac{\rho \dot{\gamma} a^2}{\eta} \simeq 0.625,$$

and the advection term in the Navier-Stokes equation is taken into account.

4.3 Simulations results

In this section, we present our numerical result obtained with FPD method in comparison to other numerical and theoretical results. Then, we show the flow field around

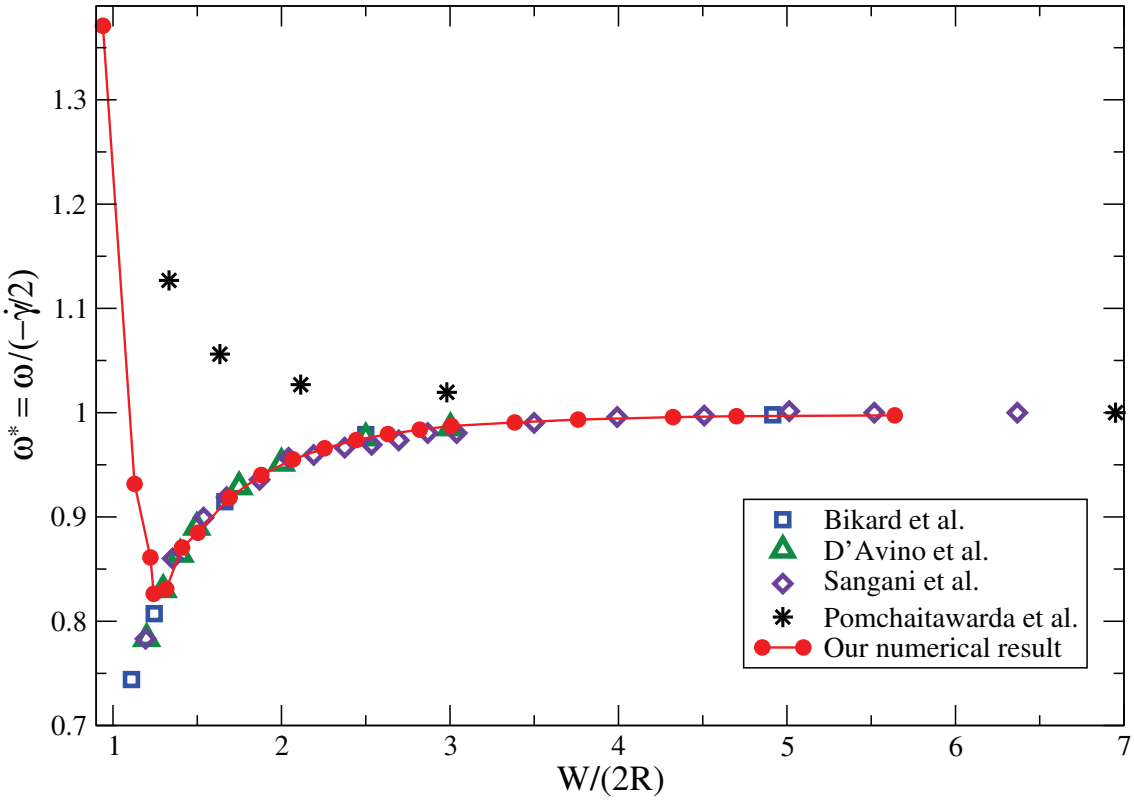

Figure 4.3: Normalized angular velocity as a function of (Gap size)/(Particle diameter).

the confined particle. finally, we show some results concerning the effect of the wall on the translational and rotational velocities of the particle.

4.3.1 Rotation of confined spherical particle in a shear flow

To study the effect of finite dimension on the rotation of a spherical particle in a shear flow, we place the spherical particle with $a = 4\delta$, $\xi = 0.5\delta$, ($R_{eff} \simeq 5\delta$) where $\delta = 1$ in the center of the simulation box. We vary the gap size w between the walls from 13δ to 60δ and calculate the angular velocity of particle ω_y. To calculate the angular velocity of a rigid spherical particle, we calculated the vorticity of the velocity field $\mathbf{V}$ and then averaged it inside the particle:

$$\omega_y = \frac{1}{2} < rot\mathbf{V} >,$$

here $< . >$ denotes averaging in the high viscosity region. On figure 4.3, we plot the normalized angular velocity $\omega_y^* = \omega_y/(-\dot{\gamma}/2)$ as a function of $w/2R$ where w is the gap size and $2R$ is the particle diameter. Our numerical results (full red circles with line) are compared with the results of Bikard et al. [55] (blue squares), D'Avino et al. [56] (green triangles), Sangani et al. [18] (violet diamonds) and Pomchaitawarda et al. [59] (black stars). A good agreement is found with results of Bikard et al. [55], D'Avino et al. [56] and Sangani et al. [18] while disagreement is found with the experimental results of Pomchaitawarda et al. [59] Although, when the sphere diameter is equal to the gap size according to the rigid contact between the sphere and walls angular velocity of sphere should be $\omega_z = -\dot{\gamma}$. The results of Pomchaitawarda et al. incorporates correctly this behavior ($\omega = -\dot{\gamma}$, when $w = 2R$) as well as another asymptotic behavior: $\omega = -\dot{\gamma}/2$ in unconfined flow. However, we believe that some experimental artifacts are present in their results. There are certainly some solid contacts between the particles and the walls of their rheometer. The methods of Bikard et al. [55], D'Avino et al. [56] and Sangani et al. [18] cannot express the case where rigid contact occur between the sphere and walls. In our simulations for very small gap size the angular velocity of the sphere increases (see figure 4.3). Because of the presence the diffusive interface around the sphere where viscosity of fluid decrease from the particle viscosity ($\eta_p = 100$) to the solvent viscosity ($\eta = 1$): when the gap size decreases an equivalent rigid contact between sphere and walls occurs even before $w/(2R)$ reaches 1.0 within a small interval with different intensity and $\omega^* = \omega/(-\dot{\gamma}/2)$ increases.

As a matter of fact, when the sphere interface touches the walls, the angular velocity of the wall is imposed to the sphere and $\omega_y \to -\dot{\gamma}$ for $w/2R \to 1$.

4.3.2 The velocity field around confined spherical particle in a shear flow

Figures 4.4 and 4.5 show the xz cross section of the velocity field at the center of the simulation box as well as the spherical particle placed in the confined shear flow. a) and c) show $\mathbf{v}-$ the velocity field of the shear flow around the particle, while b) and d) represent the disturbances of the velocity field due to presence of the particle ($\mathbf{v}' = \mathbf{v} - \dot{\gamma}x\mathbf{k}$, here $\mathbf{k}$ is the unit vector along z axis). The size of particle $a = 4\delta$, $\xi = 0.5\delta$, and $R_{eff} = 5\delta$ where $\delta = 1$. shear rate $\dot{\gamma} = 0.025$, $\eta_p = 100$ and $\eta = 1$. On figure 4.4 for a) and b) $w/(2R) = 1.0$, and for c) and d) $w/(2R) = 1.4$. For figure 4.5

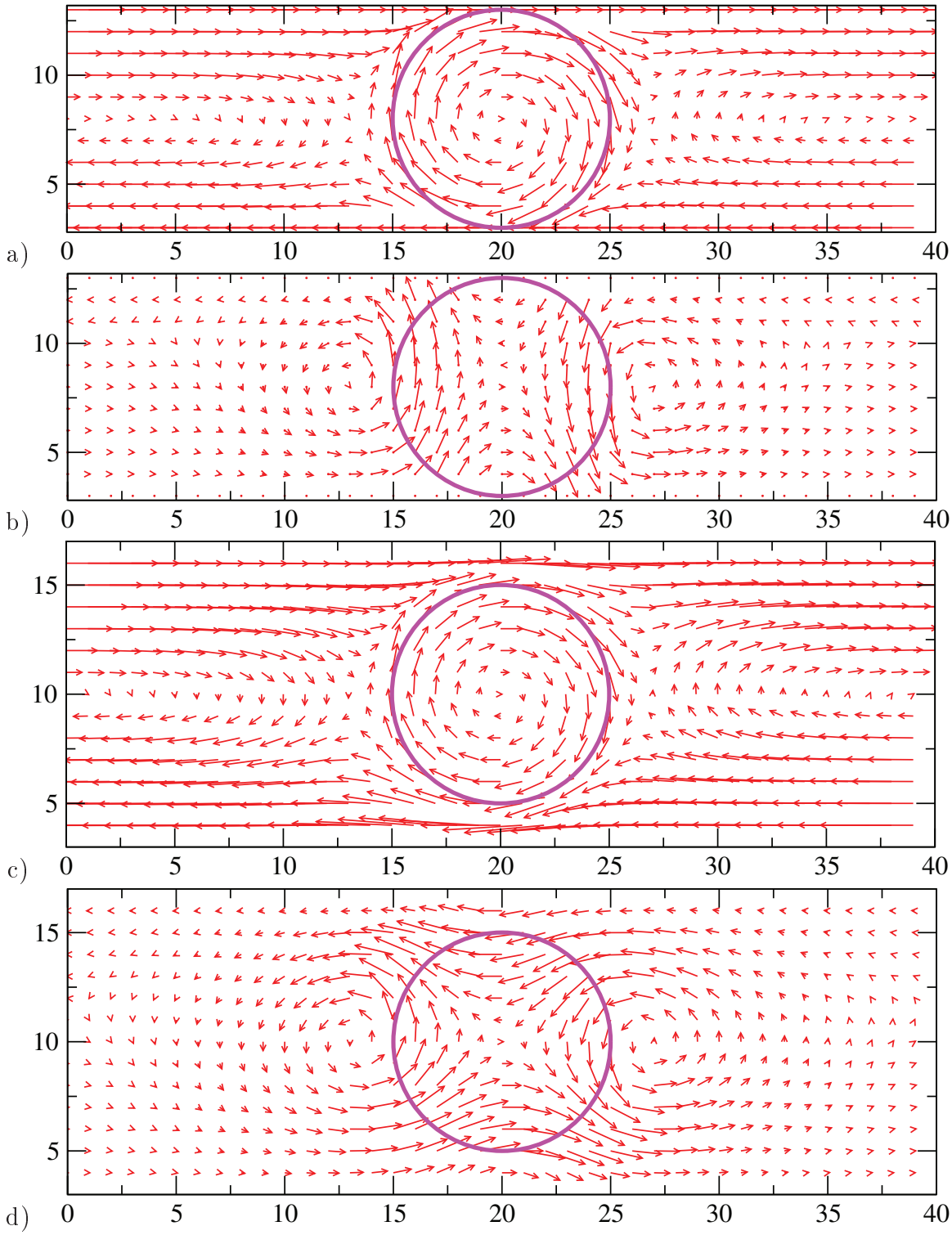

Figure 4.4: a) and c) cross section of the full velocity field around the spherical particle in confined shear flow. b) and d) the disturbance of the velocity fields. a) & b) $w/(2R) = 1.0$, c) & d) $w/(2R) = 1.4$.

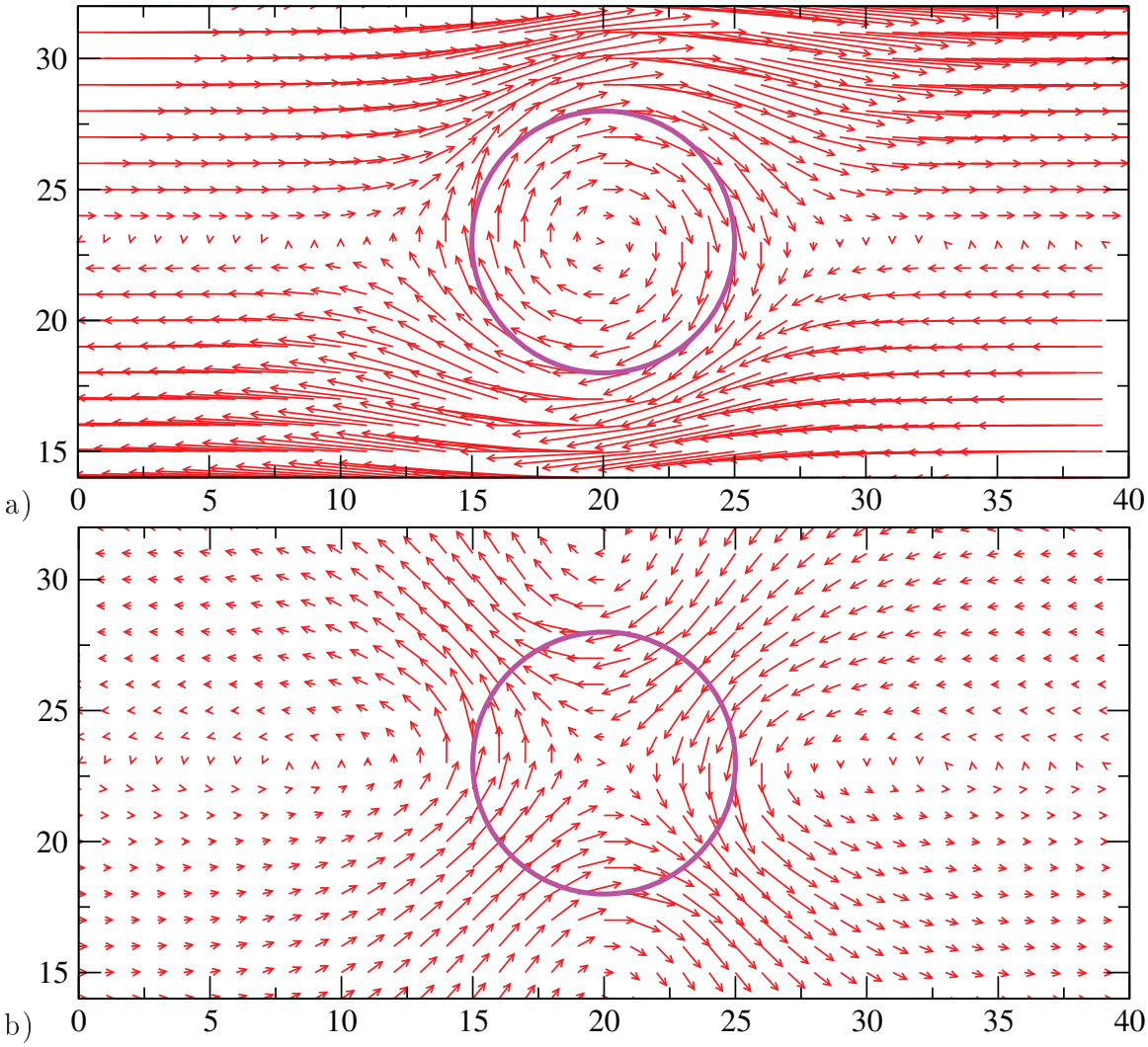

Figure 4.5: a) Cross section of the full velocity field around the spherical particle in non-confined shear flow. b) The disturbance of the velocity fields. $w/(2R) = 4.0$.

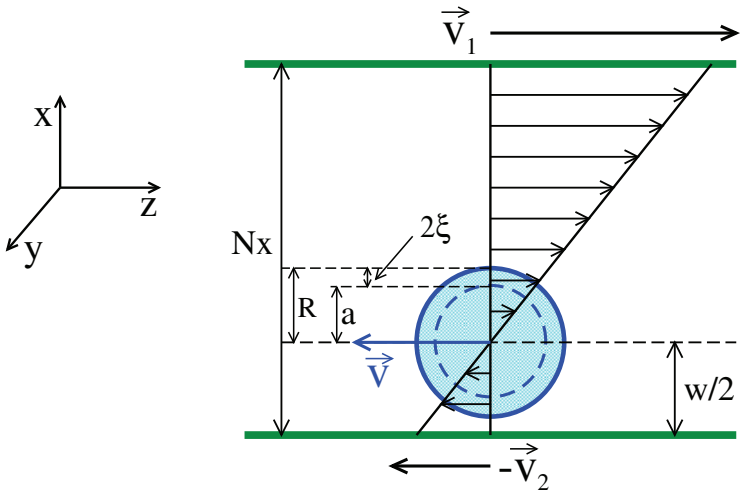

Figure 4.6: Schematic diagram of the shear flow around the spherical particle close to a wall.

confinement is very small $w/(2R) = 4.0$ and the flow is quite similar to the uniform shear flow around a spherical particle (see 3.8.2).

This velocity field allows us to better understand the decrease of the angular velocity ω_y, when increasing the confinement. The presence of a rigid spherical particle in confined shear flow creates two vortices on the left and right sides of the particle as we can see on figure 4.4 b) and d). Those vortices rotate in the opposite direction with respect to the one imposed by the shear flow on the particle and they slow down the particle rotation. A flow line between the particle and the walls is clearly oppose to the shear flow (figure 4.4 d). We can also clearly see the recirculation areas on figure 4.4 a) and c) left and right side of particle which are vanishing small when gap size is larger (see figure 4.5 a). Note that this vortexes have been also obtained by Kaoui et al. [63] on the confined spherical vesicle.

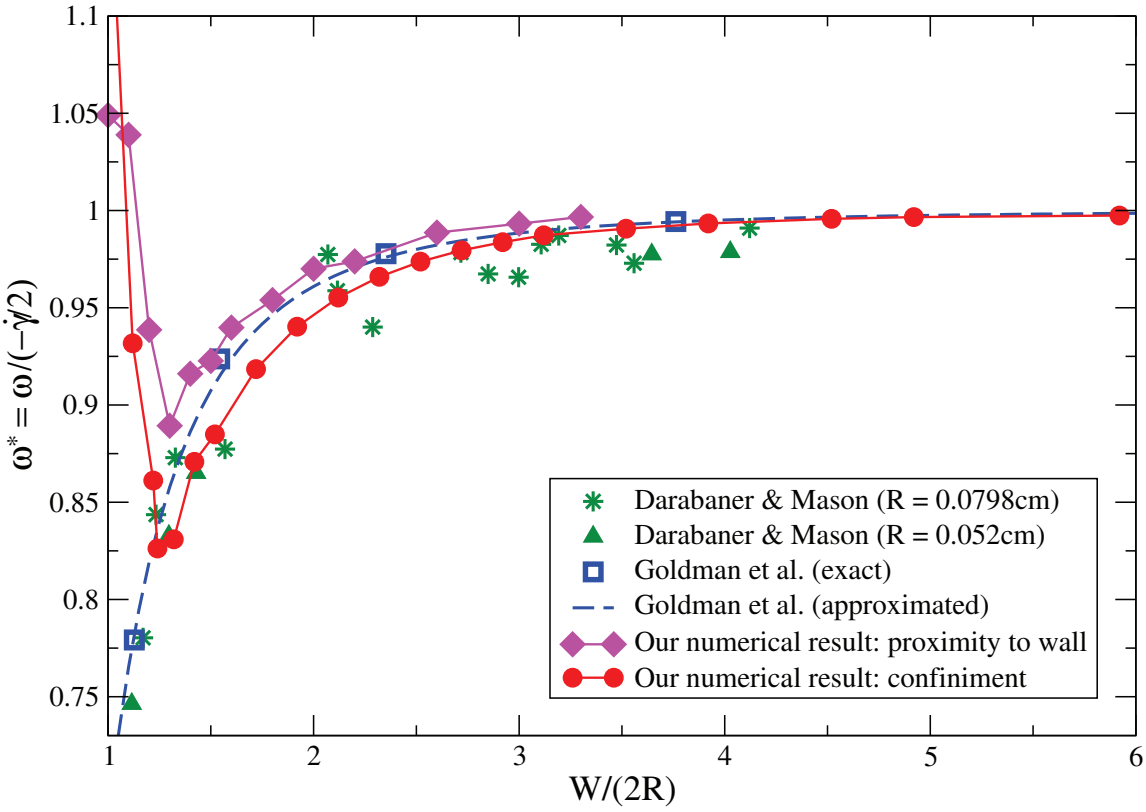

Figure 4.7: Change of angular velocity for different distances to the wall.

4.3.3 The effects of a single wall on the dynamics of a spherical particle in a uniform shear flow

We found that when a spherical particle is close to a single wall even in a unconfined shear flow the particle velocity changes. Namely, the particle rotational velocity decreases when the particle approaches the wall and the translational velocity increases or decreases depending on the velocity of the wall in such a way that the difference between the velocity of the particle and the velocity of the wall decreases compared to the difference between the velocity of the flow at the same place and the velocity of the wall (see blue arrow on figure 4.6). In order to separate the difference of the translational velocity of the particle from the velocity of the shear flow, velocities of walls ($\mathbf{v}_1$ and $\mathbf{v}_2$) are such that shear rate is fixed and velocity of shear flow at the center of the particle is zero in the absence of a particle (see figure 4.6). On figure 4.7 , we compare

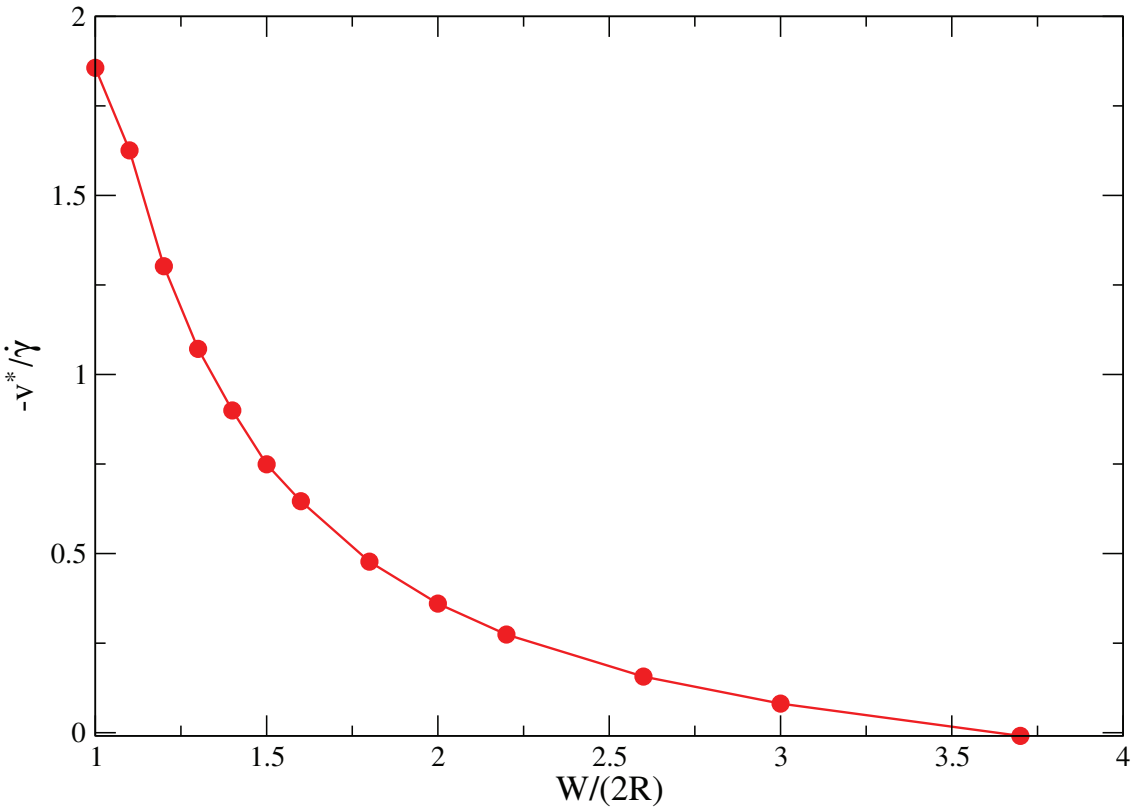

Figure 4.8: The translational velocity of the spherical particle for different distance to the wall.

normalized angular velocity $\omega_y^* = \omega_y/(-\dot{\gamma}/2)$ of a spherical particle placed close to a wall (pink squares with line) and ω_y^* for a spherical particle in a confined shear flow (red circles with line) as function of $w/(2R)$ with their results of Goldman et al. [57] and Darabaner et al. [58]. Where R is the radius of the particle and w is twice the distance from the center of the particle to the wall (see figure 4.6). In the case of the confinement (red circles with line) w is the gap size between walls. As we can see on figure 4.7 the particle rotational velocity decreases in both cases, in confinement and in the vicinity to a single wall. When $w/(2R) = 1.32$, the angular velocity of confined sphere is about 9% smaller than angular velocity of spherical particle placed close to single wall. Below $w/(2R) = 1.32$ the sphere starts to touch the wall (through its interface of thickness ξ) and ω^* starts to increase.

Figure 4.8 shows $(-\mathbf{v}^*/\dot{\gamma})$ the change of translational velocity of a spherical particle

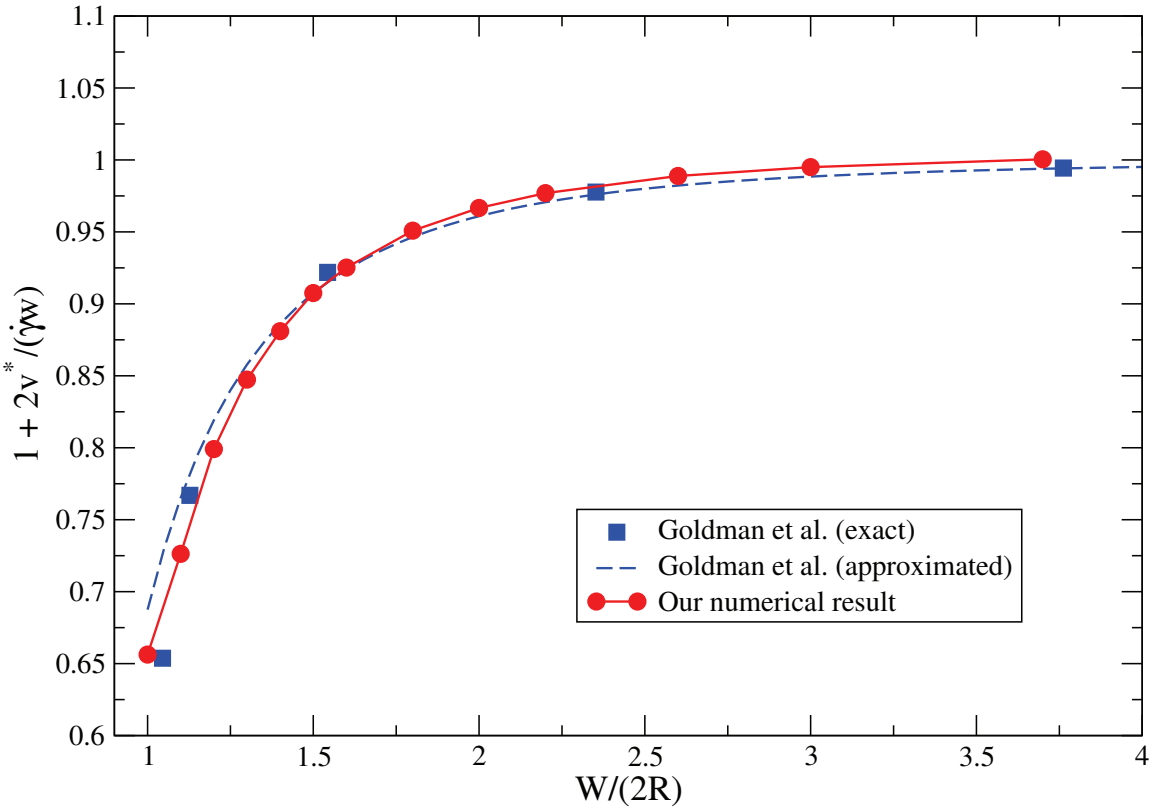

Figure 4.9: Decrease of the translational velocity of the spherical particle close to a wall in a shear flow.

in a shear flow close to a single wall as function of $w/(2R)$, here $\mathbf{v}^*$ is the difference between the velocity of the particle and the velocity of the pure shear flow at the center of particle, $\dot{\gamma}$ is the shear rate. The particle radius $a = 4.4\delta$, fluid-particle interface thickness $\xi = 0.5\delta$, and effective radius $R_{eff} = 5.4\delta$ where $\delta = 1$. shear rate $\dot{\gamma} = 0.025$. On figure 4.9 the full normalized translational velocity of the spherical particle $(U/(\frac{w}{2}\dot{\gamma}))$ as function of $w/(2R)$ is compared with the theoretical work of Goldman et al. [57] and good agreement is found. Here U is the full translational velocity of the particle in the shear flow ($U = \frac{w}{2}\dot{\gamma} + v^*$ and $U/(\frac{w}{2}\dot{\gamma}) = 1 + 2v^*/(\dot{\gamma}w)$).

Figure 4.10 shows the xz cross sections of the velocity field at the center of the simulation box. The spherical particle with effective radius $R_{eff} = 5.4\delta$ is placed close to a single wall in the shear flow. a) shows the full velocity field of shear flow around particle $\mathbf{v}$, while b) is the disturbances of the velocity fields and c) is the velocity field

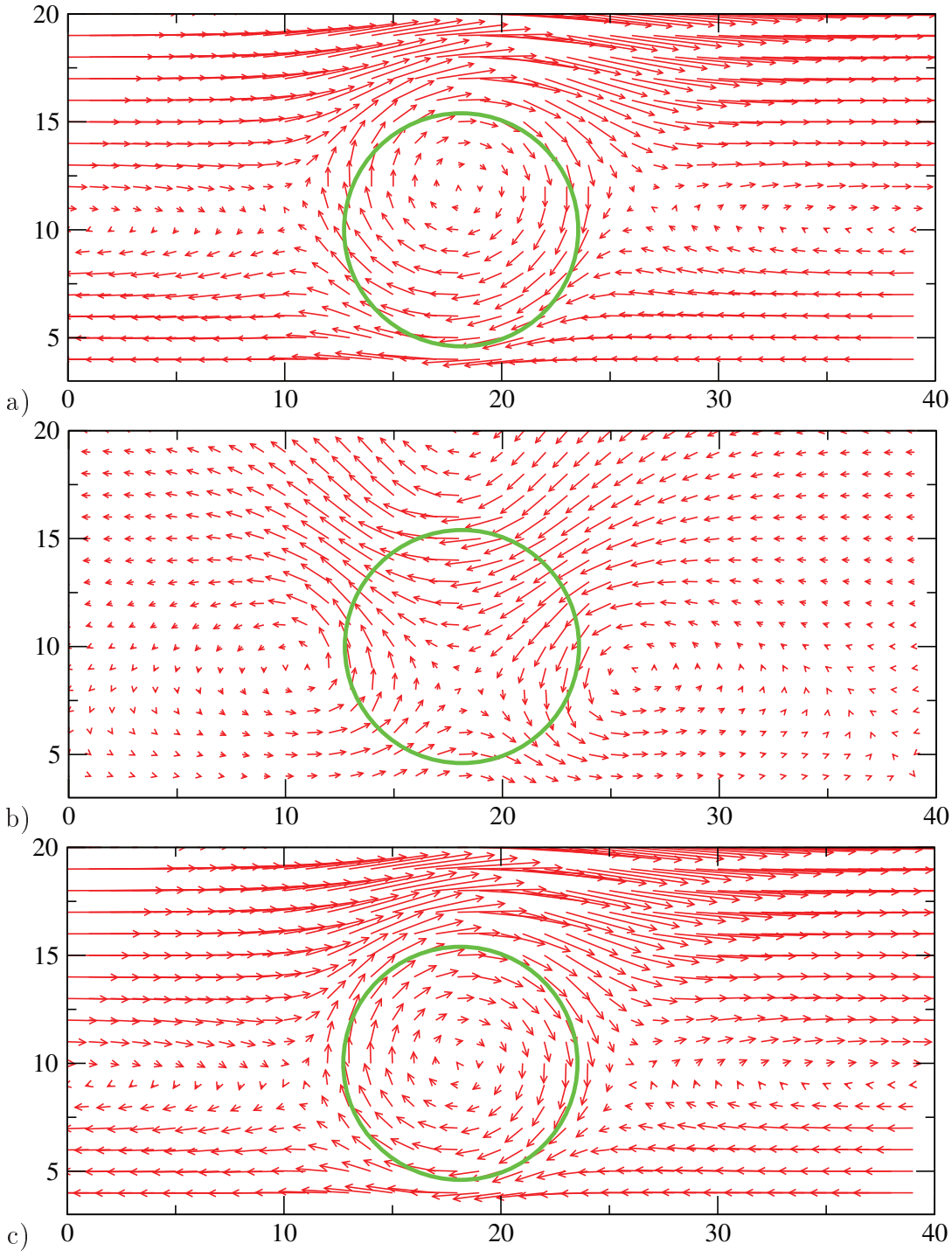

Figure 4.10: a) Cross section of the full velocity field around the spherical particle in unconfined shear flow placed close to wall. b) The disturbance of the velocity fields. c) The velocity field shifted by $\mathbf{v}^*$.

in the frame where the particle is immobile ($\mathbf{v}'' = \mathbf{v} - \mathbf{v}^*$). The distance from the center of the particle to the wall is $w/2 = 7\delta$. The flow field close to wall is stronger and the particle is moving left with the velocity $\mathbf{v}^* = -0.0225\,\mathbf{k}$, where $\mathbf{k}$ is the unit vector along z axis. This creates an impression that the particle is higher than the green contour as we can see on figure 4.10 a). After shift the full velocity field $\mathbf{v}$ by $\mathbf{v}^*$, we recover a vortex which shows the particle in its actual place, in the green contour (see figure 4.10 c).

4.4 Conclusion

In this chapter, we conducted a numerical study in order to investigate the effect of confinement on the rotation of a spherical particle placed in the shear flow, as well as the effect of the wall on the rotation and translation of a particle close to a single wall in an unconfined shear flow. We show that the confinement reduces the particle rotation. We compare our result to the other numerical and theoretical results and found very good quantitative agreement. We also found that the vicinity of a single wall modifies the velocity of a particle. Namely, the angular velocity of a particle is reduced and the translational velocity of a particle is modified so that the difference between the velocity of particle and the velocity of the wall is decreased. We believe taking into account those effects presented in confined geometry would be useful in order to optimize the setup of some microfluidic devices. We also showed that when the particle is very close to the wall(s) it starts to touch to wall(s) through its interface (of thickness ξ). It seems that we are able to reproduce a sort of solid contact between the particle and the wall(s).

In the next chapter, we will consider the rheology of the sheared suspension in presence of an external torque which modifies as well the rotation of particles in a shear flow.

Chapter 5

Sheared suspensions in presence of an external torque

In this chapter, we conduct a numerical investigation on sheared suspensions of non-colloidal spherical particles on which a torque is applied. Particles are mono-dispersed and neutrally buoyant. Since the torque modifies particles rotation, we show that it can indeed strongly change the effective viscosity of semi-dilute or even more concentrated suspensions. We performed our calculations up to a volume fraction of 28%. And we compare our results to data obtained at 40% by Yeo and Maxey [Phys. Rev. **E81**, 62501 (2010)] with a totally different numerical method. Depending on the torque orientation, one can increase (decrease) the rotation of the particles. This results in a strong enhancement (reduction) of the effective shear-viscosity of the suspension. We construct a dimensionless number Θ which represents the average relative angular velocity of the particles divided by the vorticity of the fluid generated by the shear flow. We show that the contribution of the particles to the effective viscosity can be suppressed for a given and unique value of Θ independently of the volume fraction. In addition, we obtain a universal behavior (*i.e.* independent of the volume fraction) when we plot the relative effective viscosity divided by the relative effective viscosity without torque as a function of Θ. Finally, we show that a modified second Faxén law can be equivalently established for large concentration.

Dans ce chapitre, nous effectuons une étude numérique sur les suspensions non-colloïdales de particules sphériques en cisaillement où un couple est appliqué sur les particules. Les particules sont mono-disperses avec une flottabilité neutre. Comme le couple modifie la vitesse angulaire des particules, nous montrons qu'il peut en résulter un fort changement de la viscosité effective des suspensions en régime dilué mais aussi à des régimes plus concentrés. Nous avons effectué nos calculs jusqu'à une fraction volumique de 28%. Et nous comparons nos résultats aux données obtenues à 40% par Yeo et Maxey [Phys. Rev **E81**, 62501 (2010)] avec une méthode numérique totalement différente. Selon l'orientation du couple, on peut augmenter (diminuer) la rotation des particules. Il en résulte une augmentation (diminution) forte de la viscosité effective de la suspension. Nous construisons un nombre sans dimension Θ qui représente la vitesse angulaire relative moyenne des particules divisée par la vorticité du fluide générée par l'écoulement de cisaillement. Nous montrons que la contribution des particules à la viscosité effective peut être supprimée pour une valeur donnée et unique de Θ indépendamment de la fraction volumique. De plus, nous obtenons un comportement universel (*i.e.* indépendant de la fraction volumique) lorsque nous traçons la viscosité relative divisée par la viscosité relative en l'absence de couple en fonction de Θ. Enfin, nous établissons une seconde loi de Faxén empirique valable des régimes dilués aux régimes concentrés.

5.1 Introduction

Solid particles suspended in a conventional Newtonian liquid form a suspension. This composite fluid constitutes a widespread fluid material in nature as well as in industry [64]. Fluids with controllable viscosity when an external field is applied are of a considerable interest because of their occurrence in many kinds of industrial devices such as active dampers, clutches or brakes [13, 12, 11]. For example, concerning automobile dampers: depending on road conditions, viscosity of the damping fluid needs to be adjusted. An external field is used to modify properties of the fluid by exerting a torque on suspended particles of nanometric or micrometric size. For electro-rheological (ER) fluids [21, 65], polarizable particles are dispersed in a nonconducting liquid. When the suspension is submitted to an electric field, each dipolar particle can align itself along the electric field direction. This alignment is suspected to stop or modify the shear-induced rotation of particles perpendicularly to the field. A second phenomenon is a clustering: the particles group together in elongated aggregates due to their attractive dipole-dipole interaction of magnetic or electrical origin for example. These two effects reversibly change the mechanical properties and thus the rheology of the medium. In some ER fluids, a rotation of the particles can be induced by the electric field. This rotation has been experimentally observed as well as its impact on the effective viscosity of the overall suspension [65]. This phenomenon can be used to tune the effective viscosity of a suspension. The possibility of changing the viscosity of a suspension by exerting a torque on its particles has also been demonstrated on ferrofluids subjected to a rotating magnetic field [66]. Ferrofluids are suspensions of rigid particles wearing a magnetic dipole. By applying a time varying external magnetic field, a torque is exerted on particles which thus rotate. This kind of effect exists not only for industrial applications but also for biological suspensions where the gravitational field is suspected to exert a torque on inhomogeneous spherical unicellular algae [67, 9]. By changing cells rotation in a shear flow, gravity might impact flow properties of algae suspensions.

Brenner [14] analytically studied the dynamics of polar spherical particles in a shear flow. The suspension is submitted to an external field which modifies the rotation

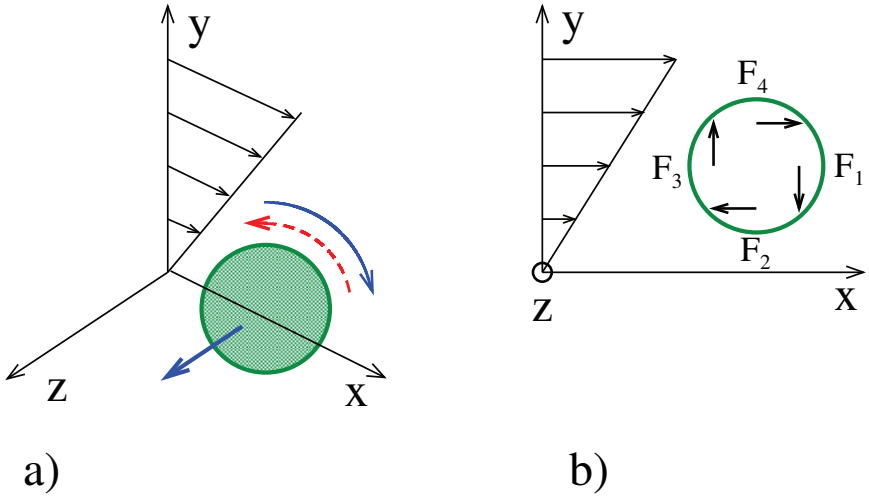

Figure 5.1: Particle in a shear flow submitted to an external torque **L**.

of the spheres and therefore the effective viscosity of the suspension. This work was inspired by an experimental study [22] on magnetic fluids. In the dilute regime where hydrodynamic interactions can be neglected, the case of dipolar spherical particles in an external field can be solved analytically (see below).

At higher concentrations, numerical investigations are necessary. We refer here to the work of Prosperetti and his group [68, 69, 70, 71] hereafter referred to collectively as Prosperetti *et al.* They used a direct simulation method and studied the behavior of a suspension subjected to a torque in a statistically nonuniform flow and the behavior of a suspension subjected to a uniform shear flow. Feng *et al.* [72] used a boundary element method and studied a set of force-free translationally mobile spheres confined between a pair of no-slip parallel plates. The spheres rotate at an imposed position-independent angular velocity ω_z by applying a given torque. There is no imposed shear rate: the

rotation of the spheres generate a suspension-scale simple shear flow (Couette flow) . Feng *et al.* [72] also used a Poiseuille geometry. Yeo and Maxey [17] used a force-coupling method to study sheared suspensions at high concentrations and submitted to a torque. At concentration higher than 48%, they observe a regular and periodic arrangement of the particles in the flow. Below that value, including 40%, they observe an homogeneous sheared suspension without any rearrangement.

On figure 5.1 we show a) Particle in a shear flow submitted to an external torque **L**. The flow makes the particle rotate in one direction (solid arrow) while the torque induces a rotation in the same direction or in the opposite direction (dashed arrow) depending on the orientation of **L**. b) In our simulations, the torque is applied with a set of tangential forces $\mathbf{F}_i$ with $i = 1..4$ applied to each sphere in the xOy plane.

In this paper, we use the fluid particle dynamics method (FPD discussed in chapter 3) [40] to investigate the effect of torque on the rheology of a suspension of spherical particles. We analyze the competition between an imposed shear flow and an applied torque, as well as their respective contribution to the total effective viscosity on a range of volume fraction from 0 to 28%. We obtain a universal behavior independent of the volume fraction when we plot the total relative effective viscosity divided by the total relative effective viscosity in the absence of torque as a function of the dimensionless number Θ:

$$\Theta = \frac{\dot{\gamma}/2 + < \omega_z >}{\dot{\gamma}/2}. \tag{5.1}$$

It represents the difference between the angular rotation of the particles $< \omega_z >$ and the solid rotation component of the sheared fluid ($\dot{\gamma}/2$) in the absence of particles, divided by $\dot{\gamma}/2$. In the absence of an external torque, the particles angular rotation is equal to $-\dot{\gamma}/2$ and $\Theta = 0$. This number can be either positive or negative depending on the torque orientation anti-parallel or parallel to the flow vorticity (figure 5.1). Θ is the dimensionless number used all along this paper. The symbol $< . >$ means that we average on the set of particles. Since here we impose a constant torque on each particle, we average the angular velocity on the set of particles. Note that Θ has a meaning only when $\dot{\gamma}$ is non-zero.

We perform simulations up to 28% and we also include the plot of Yeo and Maxey [17] data obtained at 40% with a different numerical method. We show that they are perfectly consistent with our results when these data are plotted as a function of Θ.

The volume fraction ϕ is defined as the volume of the set of particles divided by the total volume of the suspension. On each particle, the same value of the torque is applied. When the external applied torque is anti-parallel to the vorticity (z-axis on figure 5.1), the torque slows down particles rotation and the effective viscosity is increased. This can be understood since particles create a counter rotating flow opposed to that of the shear flow. Therefore, in order to impose the same value of the shear rate $\dot{\gamma}$, the shear stress σ_{xy} must be larger. Thus, the effective viscosity

$$\eta_{eff} = \frac{\sigma_{xy}}{\dot{\gamma}} \tag{5.2}$$

is increased. On the contrary, when the particle rotation is enhanced by an external torque parallel to the vorticity, it is easier to shear the suspension and η_{eff} decreases.

We show that structuration of the particles into aggregates is not necessary to obtain a strong modification of the effective viscosity: the modification of particles rotation is indeed sufficient to create a shear thinning or a shear thickening effect. The second Faxén law [73] which is a relationship between applied torque and rotation velocity of particles is usually valid for dilute suspensions. Here, we derive an empirical second Faxén law valid from dilute to concentrated suspensions (up to 40%).

In section 5.2, we briefly present the well known results concerning the effective viscosity of sheared suspensions. In section 5.3, we apply a torque on particles in a dilute suspension under shear. We analytically derive the effective viscosity as a function of Θ. In section 5.4, we show some parameters and details of our numerical method, the fluid particle dynamics. In section 5.5, in order to test our method with several particles, we first apply a constant torque on each sphere in a fluid at rest (in the absence of a shear flow). In such a case, we compare our results on vortex viscosity with the ones of Prosperetti *et al.* as well as Feng *et al.* [72] We also compare our numerical results on shear viscosity in the absence of torque with other published results. Then, concerning our work (rotating particles submitted to a torque and a shear flow) we show that plotting the effective viscosity as a function of Θ, reveals universal behavior (*i.e.* independent of the volume fraction). Finally, we conclude in section 5.6.

5.2 Effective viscosity of suspensions of torque free and rigid particles

It is well known that the effective viscosity η^0_{eff} of a sheared suspension of torque free spherical particles follows a virial expansion [64]:

$$\eta^0_{eff} = \eta[1 + \alpha\phi + \beta\phi^2 + \mathcal{O}(\phi^3) \tag{5.3}$$

where ϕ is the volume fraction defined as the volume of particles normalized by the total volume of the suspension, η being the viscosity of the suspending Newtonian fluid. For a suspension of hard spheres, the linear term (the intrinsic viscosity) is $\alpha = 2.5$ as calculated by Einstein [74, 75] for a strong dilution. Then, when the semi-dilute regime is reached (for $\phi > 20\%$), the particles get closer and start to interact hydrodynamically. Batchelor and Green [76] showed that hydrodynamic interactions contribute to the second order in ϕ. They found $\beta = 5.2 \pm 0.3$ for a non-Brownian suspension where particles are uniformly distributed. Since then, a more precise estimation of $\beta = 5.0$ has been achieved by Cichocki and Felderhof [77]. For more concentrated suspensions, interactions with three or even more bodies contribute to the effective viscosity and the empirical law of Krieger and Dougherty [78] describes η^0_{eff} on a broad range of volume fractions:

$$\eta^0_{eff} = \frac{\eta}{(1 - \phi/\phi_m)^{\alpha\phi_m}} \tag{5.4}$$

where ϕ_m corresponds to the maximum random packing value of the volume fraction:

$$\phi_m \approx 0.62$$

for spherical and rigid particles. Note that equation (5.3) is the Taylor expansion up to order 2 of equation (5.4) for $\phi \ll 1$.

We define the relative effective viscosity in the absence of torque:

$$\Delta\eta^0_{eff} = \frac{\eta^0_{eff} - \eta}{\eta}. \tag{5.5}$$

5.3 Dilute suspensions in presence of an external torque

In this section we show how to calculate the contribution of an external torque exerted on each particle to the effective viscosity of a sheared suspension in the dilute regime. If we consider a dilute regime where spherical and neutrally buoyant particles of radius R, are far enough not to interact, we can consider a set of N independent particles like the one represented on figure 5.1. In the dilute regime and in the absence of an external torque, each particle rotates in the shear flow at the angular velocity $\boldsymbol{\omega}$ with the non-zero component

$$\omega_z = -\frac{\dot{\gamma}}{2}. \tag{5.6}$$

When an external torque $\mathbf{L}$ is applied to the particle along the z-axis, ω_z can be increased or decreased depending on the orientation of the torque. The total deviatoric stress σ_{xy} which must be applied to the suspension in order to maintain a given shear rate $\dot{\gamma}$ is such that

$$\sigma_{xy} = \sigma^0_{xy} + \sigma^R_{xy}. \tag{5.7}$$

Where σ^R_{xy} is the contribution of the external torque to the stress, while σ^0_{xy} is the deviatoric stress in the absence of torque. Batchelor [79] showed that:

$$\sigma^R_{xy} = \frac{N\,L}{2\mathcal{V}}, \tag{5.8}$$

where L is the component of the torque $\mathbf{L}$ along the z-axis, N is the number of particles and $\mathcal{V}$ is the total volume of the suspension. Since we deal with low Reynolds number hydrodynamics, we can use the linearity of Stokes equation which rules the incompressible fluid flow around particles. The second Faxén law [73] relates the external torque $\mathbf{L}$ exerted on the particle to the angular velocity $\boldsymbol{\omega}$:

$$\mathbf{L} = -8\pi R^3 \eta (\frac{1}{2}\, rot\, \mathbf{V}_0 - \boldsymbol{\omega}), \tag{5.9}$$

where $\mathbf{V}_0$ is the velocity field in the absence of particles, in our case: $\mathbf{V}_0 = (\dot{\gamma} y, 0, 0)$. It gives

$$L = 8\pi R^3 \eta \Omega \tag{5.10}$$

where

$$\Omega = \frac{\dot{\gamma}}{2} + \omega_z \tag{5.11}$$

represents the difference of angular velocity between ω_z and the one imposed by the shear flow alone: $-\dot{\gamma}/2$. For a torque free particle, we have $\Omega = 0$ (*i.e.* $\omega_z = -\dot{\gamma}/2$). By using the definition of the volume fraction

$$\phi = \frac{4/3\,\pi R^3\,N}{\mathcal{V}},$$

we obtain:

$$L = \frac{6\mathcal{V}}{N\,\phi\eta\Omega}, \tag{5.12}$$

which gives

$$\sigma_{xy}^R = 3\phi\eta\Omega \tag{5.13}$$

and the contribution of the particles relative rotation to the effective viscosity in the dilute regime,

$$\eta_{eff}^R = \frac{\sigma_{xy}^R}{\dot{\gamma}} \tag{5.14}$$

is such that:

$$\eta_{eff}^R = \frac{3}{2}\phi\eta\Theta \tag{5.15}$$

with

$$\Theta = \frac{\Omega}{\dot{\gamma}/2}$$

as defined before. Note that η_{eff}^R has been also called vortex viscosity by Condiff and Dahler [80].

When no torque is applied ($\omega_z = -\dot{\gamma}/2$), it corresponds to $\Theta = 0$, and when the external torque stops the particle rotation ($\omega_z = 0$) then $\Theta = 1$. When Θ is positive ($L > 0$), particles rotation is slowed down by the external torque and effective viscosity is increased. But when Θ is negative ($L < 0$), the rotation of particles is increased by the external torque and the effective viscosity is decreased. Therefore, at fixed external torque, shear thickening or shear thinning is observed when Θ is respectively positive or negative. As a matter of fact when increasing the shear rate $\dot{\gamma}$ the flow overcomes the external torque effect and since Θ tends to 0 the suspension recovers its torque free

effective viscosity η^0_{eff}.

The total effective viscosity is given by:

$$\eta_{eff} = \frac{\left(\sigma^0_{xy} + \sigma^R_{xy}\right)}{\dot{\gamma}} \tag{5.16}$$

it leads to

$$\eta_{eff} = \eta^0_{eff} + \eta^R_{eff}. \tag{5.17}$$

As in equation 5.5, we can define the relative effective viscosity in the presence of torque:

$$\Delta\eta_{eff} = \frac{(\eta_{eff} - \eta)}{\eta} \tag{5.18}$$

which gives for dilute suspensions:

$$\Delta\eta_{eff}(\phi, \Theta) = \frac{5}{2}\,\phi(1 + \frac{3}{5}\Theta). \tag{5.19}$$

For example, when the external torque stops the particle rotation ($\omega_z = 0$ and $\Theta = 1$), one obtains $\Delta\eta_{eff} = 4\phi$. This gives a modified intrinsic viscosity such that $\alpha(\Theta = 1) = 4$: a result which was first derived by Brenner [14].

5.4 Model and 3D numerical method

Suspended elements are mono-disperse spheres of radius R. Considering large particles, the Brownian motion is not taken into account. Spheres are suspended in a Newtonian liquid of viscosity η sheared between two walls. The two walls located at $y = \pm w/2$ move at $v_x = \pm v_0$ respectively, so that the shear rate is

$$\dot{\gamma} = \frac{2v_0}{w}.$$

No-slip conditions are used at the fluid/walls interface. In order to neglect the effect of walls, we choose $15 < w/R < 20$ *i.e.* $w \gg R$. As an initial condition, we distribute the spheres randomly and homogeneously (taking care to avoid any overlaps).

Note that our code is able to handle small but finite Reynolds numbers. However, in this work, Reynolds number are about 10^{-2}, therefore inertial effects are indeed

negligible. We deal with neutrally buoyant particles with a density ρ equal to the fluid density. We use the 3 dimensional version of "fluid particle dynamics" (FPD) see details in Chapter 3). Note that our calculations are done for several volume fractions up to $\phi = 28\%$. For bigger ϕ-values, we cannot avoid effects such as the formation of depletion layers close to the walls [15].

In order to apply an external torque perpendicular to the shear plane (xOy) on the particles, a set of tangential forces $\mathbf{F}_i$ where $i = 1...4$ are applied on each particle in the xOy plane (figure 5.1-b). Each force has the same intensity. Then, the same torque

$$\mathbf{L} = \Sigma_{i=1}^{4} \mathbf{r}_i \times \mathbf{F}_i \tag{5.20}$$

is applied on each particle. In order to change $\mathbf{L}$, we vary the components F_i.

Depending on simulations, values from $\dot{\gamma} = 10^{-5}/\delta t = 10^{-2}$ to $\dot{\gamma} = 10^{-6}/\delta t = 10^{-3}$ are used. Inertia is negligible since only small Reynolds numbers are considered here:

$$10^{-2} < Re = \frac{\rho \dot{\gamma} a^2}{\eta} < 10^{-1}.$$

The typical simulation box size is $\ell_x = \ell_y = \ell_z = w = 60\delta$. Here, $\delta = 1$. Boundary conditions are such that the fluid velocity is imposed on the upper ($y = +w/2$) and lower ($y = -w/2$) wall: $v_x(x, y = \pm w/2, z) = \pm v_0$, while periodic boundary conditions are adopted in the xz - directions.

The stokes flow around the spheres is sufficient to avoid particle inter-penetrations. However, above $\phi = 35\%$, we must decrease the time step δt in order to avoid such numerical artifacts. Note that in our simulations, we have not included the dipole-dipole attraction (like magnetic interactions for example) since we would like to study the effect of rotation of particles on the rheology separately from the effects of clustering. On figure 5.2 we show: a) the viscosity field of a suspension of 50 spherical particles. b) The isosurface of the viscosity field. The radius of particles is $a = 3\delta$, the fluid-particle interface thickness $\xi = 0.5\delta$, effective radius of particles $R \simeq a + 2\xi = 4\delta$, the particle viscosity $\eta_p = 100$ and the solvent viscosity, here $\delta = 1$ is the mesh size.

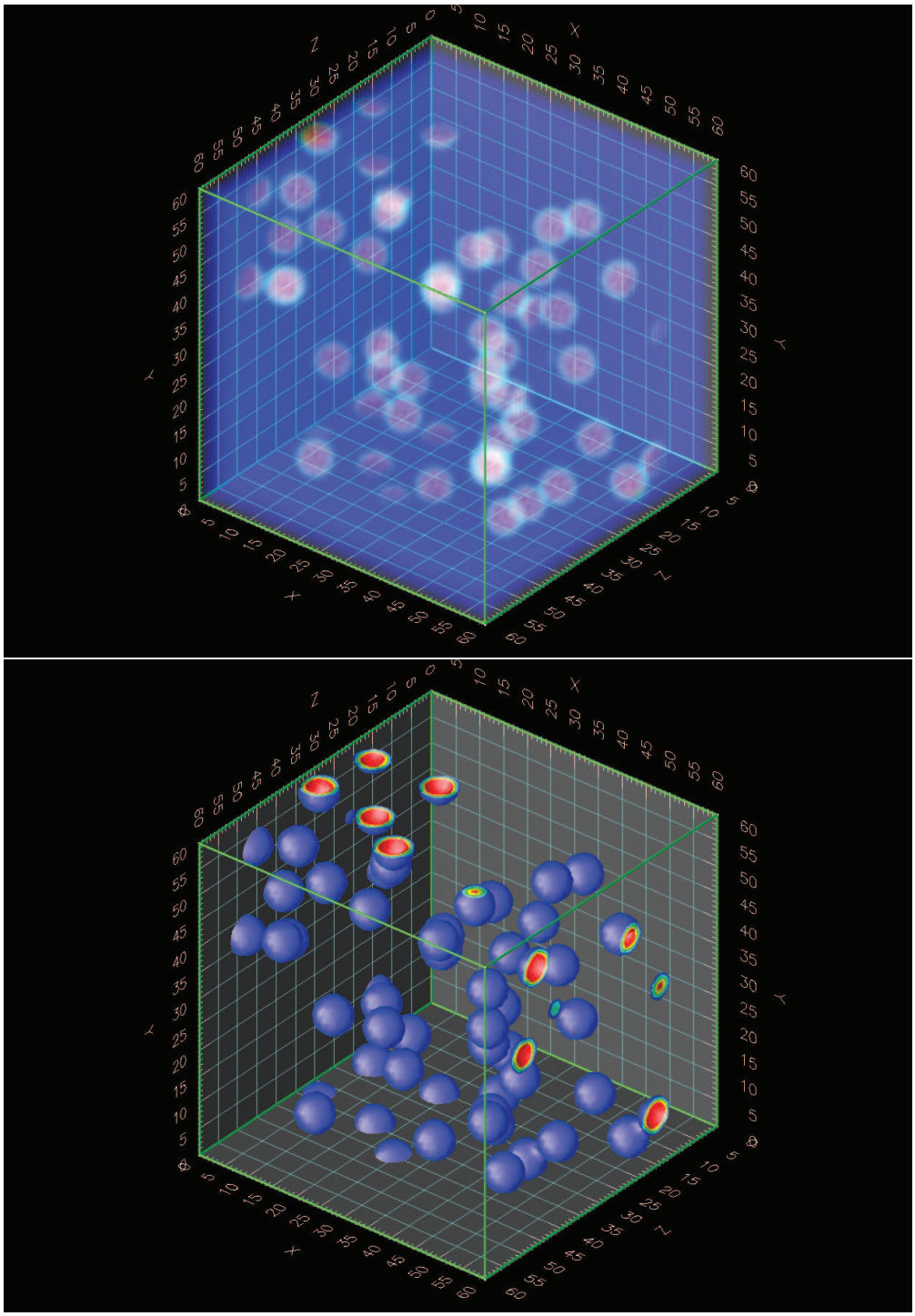

Figure 5.2: a) The viscosity profile of the suspension of 50 spherical particles. b) The Isosurface of the viscosity field.

5.4.1 Calculation of the effective viscosity

The effective viscosity of the suspension is evaluated by calculating the tangential force per unit surface exerted by the walls on the fluid:

$$f_x^{\pm}(t) = \bar{\sigma}_{xy}(y = \pm w/2,\, t)\, n_y \tag{5.21}$$

which is necessary to maintain a constant velocity $\pm v_0$ on the upper $(+)$ and lower $(-)$ walls. The unit vector $\mathbf{n}$ is normal to the fluid/wall interface. $\bar{\sigma}_{xy}$ represents the average of $\sigma_{xy}(\pm w/2)$ on the whole surface of the fluid in contact with the walls. The time dependent effective viscosity is thus

$$\eta_{\mathit{eff}}(t) = \frac{f_x^+(t) - f_x^-(t)}{2\dot{\gamma}}. \tag{5.22}$$

Initially, we start with a random distribution of spheres positions. After a transient regime, the effective viscosity reaches a plateau and remains stable after several thousands of time steps (see figure 5.3). By eliminating the initial transient regime and averaging the plateau values, we finally obtain the averaged effective viscosity $\bar{\eta}_{eff}$ calculated for a given initial configuration. On figure 5.3 we plot the relative effective viscosity as function of the simulation time with shear rate $\dot{\gamma} \simeq 0.0175$.

5.5 Results

In this section, we show our numerical results for the vortex viscosity in comparison to other published results as well as shear viscosity in the absence of torque. Then we present our results concerning shear viscosity in presence of an external torque. After that we derive a semi-empirical formula for the effective viscosity of the suspension valid up to 40% concentration.

5.5.1 Vortex viscosity

Feng *et al.* [72] have calculated the contribution of a torque applied on suspended particles in a fluid at rest to the effective viscosity $\eta_{eff}^R(\phi)$ (vortex viscosity). In order to compare our results with Feng *et al.* and Prosperetti *et al.* we apply the same torque

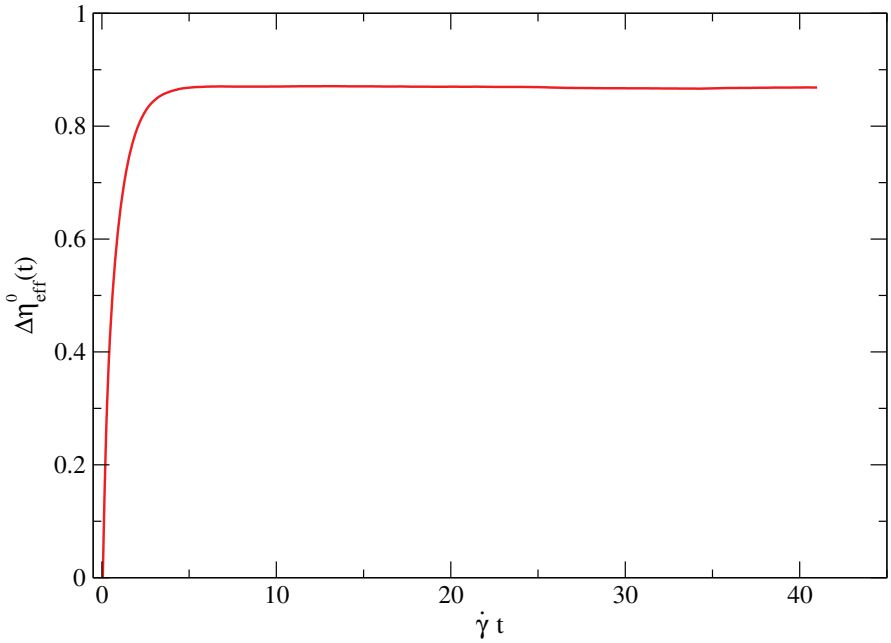

Figure 5.3: a) The effective viscosity as function of simulation time.

L on each particle and by averaging the angular velocity of the particles $< \omega_z >$ (a value that depends on ϕ) we can easily obtain the vortex viscosity by using the following relation [72, 80]:

$$\boldsymbol{\mathcal{L}} = 4\eta^R_{eff}(\phi)\left[\frac{1}{2}\boldsymbol{\nabla}\times\mathbf{V_0} - <\boldsymbol{\omega}>\right], \tag{5.23}$$

where

$$\boldsymbol{\mathcal{L}} = \frac{N\boldsymbol{L}}{\mathcal{V}}$$

is the total torque per unit volume. Note that this expression is an *a priori* constitutive law which applies to the suspension itself. It is different from the 2nd Faxén law (5.9) which applies to a single sphere in a fluid. Equation (5.23) simply shows that difference between the particles angular velocity and the vorticity of the fluid is proportional to $\boldsymbol{\mathcal{L}}$. The coefficient of proportionality is the effective vortex viscosity. This expression originally introduced by Condiff and Dahler [80] has been *a posteriori* verified by Feng *et al.* in two different geometries. In our case we apply the same torque **L** on each particle along the $z-$axis ($L > 0$) and the particles have a clockwise rotation. Therefore,

it reads

$$\mathcal{L} = 2\sigma_{xy}^{R}. \tag{5.24}$$

Since the fluid is at rest when no torque is applied ($V_0 = 0$), we obtain:

$$\eta_{eff}^{R} = \frac{\sigma_{xy}^{R}}{2 < \omega_z >}. \tag{5.25}$$

Here, the configuration (rotating particles in a fluid at rest) is a bit different from the other configuration studied in this paper (rotating particles in an imposed shear flow). In the first case, the value of the induced shear rate $\dot{\gamma}_{ind}$ depends on ϕ. Therefore, the corresponding value of Θ depends also on ϕ. However, by using equation (5.9) which holds for the dilute regime ($\phi \ll 1$), we obtain

$$\sigma_{xy} = \frac{N}{2V} 8\pi\eta R^3 \omega_z \tag{5.26}$$

Thus

$$\frac{\eta_{eff}^{R}}{\eta} = \frac{3}{2}\phi \tag{5.27}$$

[14] equivalent to $\Theta = 1$ for a dilute suspension of non-rotating spherical particles in an imposed shear flow. On figure 5.4, we compare our results to Feng's results and to the results obtained previously by Prosperetti *et al*: numerical results and the empirical law:

$$\frac{\eta_{eff}^{R}}{\eta} = 1.5\,\phi\,(1-\phi)^{1.5-0.41\phi} \tag{5.28}$$

The agreement is indeed very good. In our simulations, the same torque is applied on all the spherical particles. As expected, at low ϕ, the result of Brenner [14] is recovered.

We can also calculate the effective viscosity when no torque is applied on a sheared suspension ($\dot{\gamma}$ imposed and $L = 0$) (*i.e.* $\Theta = 0$), this validates also our measure of ϕ. In the first case, the effective viscosity of the sheared suspension behaves as equation 5.4.

On figure 5.5, we have plotted our numerical results, effective shear viscosity as a function of the volume fraction when no torque is applied (*i.e.* $\Theta = 0$). Comparison is made with experimental data (upper and lower limits are given by Thomas [81] as well as with the simulation results of others. [72, 82, 83, 81, 84] Here also we obtain a very good agreement.

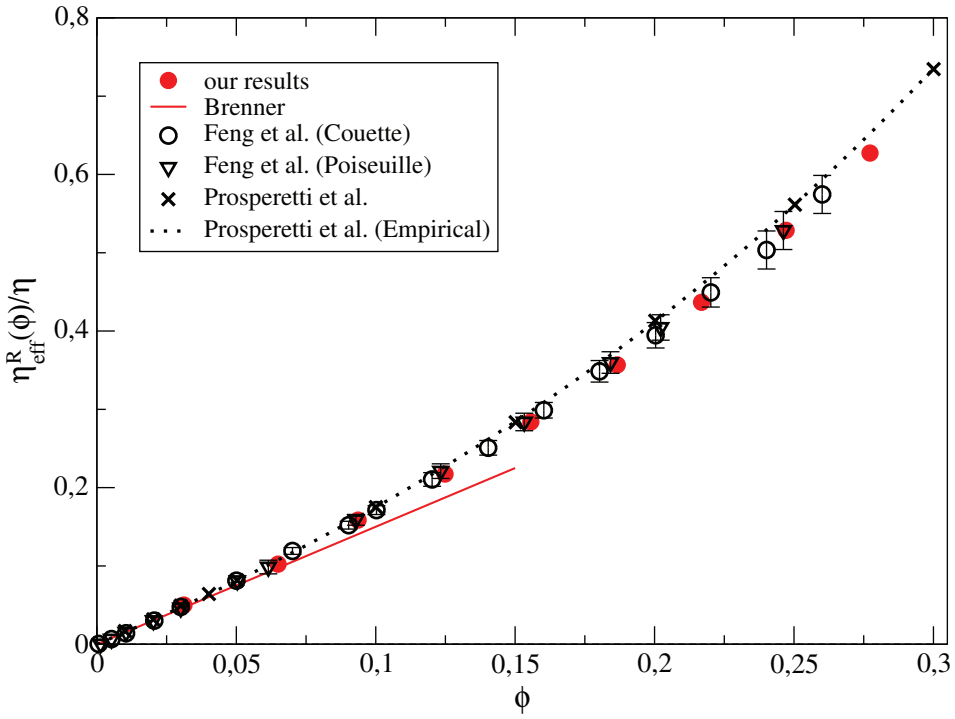

Figure 5.4: Vortex viscosity as a function of the volume fraction.

5.5.2 Shear viscosity in presence of an external torque

Now, we concentrate on a sheared suspension in the presence of a torque on each particle ($\dot{\gamma} \neq 0$, *i.e.* Θ finite) which represents our new results. We examine the competition between the torque exerted on each particle and the shear rate imposed by the flow. The torque can help to increase or decrease the rotation velocity of the particles in comparison to the one ($\omega_z = -\dot{\gamma}/2$) imposed by the shear rate. This has been already examined for very dense suspensions by Yeo and Maxey [17] where periodic arrangements were observed for $\phi \geq 48\%$. Here, we examine the range of $0 < \phi < 28\%$. However, we show the results of Yeo and Maxey obtained for $\phi = 40\%$ (below concentration where arrangements are observed) are consistent with our results once plotted as a function of Θ (they are plotted as a function of a dimensionless torque by Yeo and Maxey [17]).

In figure 5.6, the relative effective viscosity is plotted for three values of Θ as a function of ϕ. Solid lines are calculated with equation (5.29). When no torque is

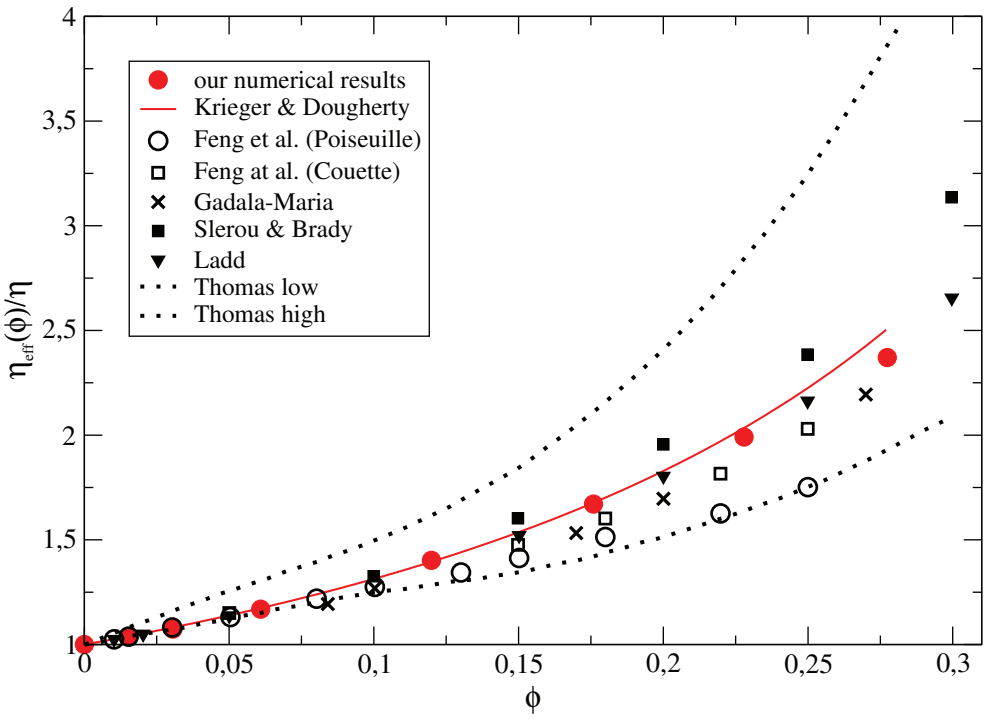

Figure 5.5: Effective shear viscosity as a function of the volume fraction when no torque is applied.

applied ($\Theta = 0$), we recover the non-linear dependence of $\Delta\eta^0_{eff}$ well fitted by equation (5.4). When particle rotation is stopped ($\Theta = 1$) the effective viscosity is increased while it is decreased when particle rotation is in the same direction than the one imposed by the shear flow ($\Theta = -1$). At $\phi = 28\%$, we see a small difference between Krieger and Dougherty's law and our data. This is due to a slight depletion of particles close to the walls which occur at hight enough concentration [15] which tends to decrease the shear effective viscosity.

As predicted by equation (5.19) for dilute regimes, plotting the relative effective viscosity $\Delta\eta_{eff}$ as a function of Θ gives a set of linear curves which cross the zero viscosity axis for the same value $\Theta \approx -1.6 \pm 0.1$ close to $\Theta = -5/3$ and with a slope $3/2\phi$ (figure 5.7). But, $\Delta\eta_{eff}$ is still linear for higher volume fractions up to 28%, following the empirical law:

$$\Delta\eta_{eff}(\phi, \Theta) = \Delta\eta^0_{eff}(\phi)\left(1 + \frac{3}{5}\Theta\right) \tag{5.29}$$

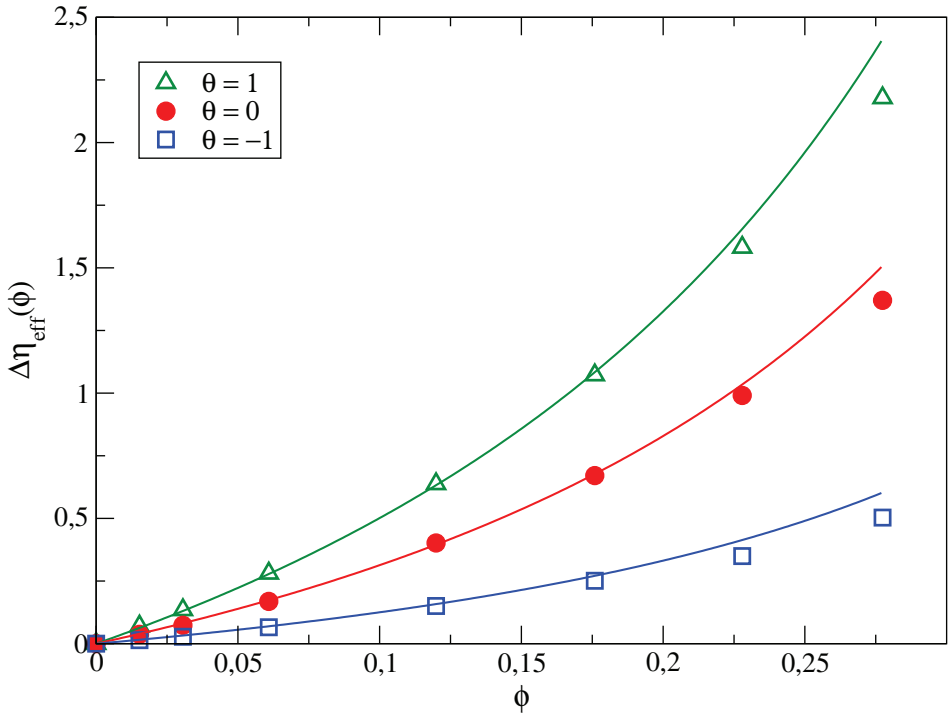

Figure 5.6: Relative effective viscosity as a function of the volume fraction ϕ for three different values of Θ.

which tends to equation (5.19) when $\phi \ll 1$ since $\Delta\eta^0_{eff}$ tends to $5/2\phi$. Here the value of Θ is averaged on the N particles:

$$\Theta = \frac{<\Omega>}{\dot{\gamma}/2} = 1 + \frac{<\omega_z>}{\dot{\gamma}/2}, \tag{5.30}$$

where $<\ .\ >$ is the average on the set of particles. On figure 5.7 we show relative effective viscosity as a function of Θ for different values of the volume fraction. Solid lines are obtained with equation (5.29) which fits remarkably well our numerical results. The data points of Yeo and Maxey [17] obtained for $\phi = 40\%$ with a totally different numerical method are also very well fitted when represented as a function of Θ (see below). Therefore all the curves, whatever the value of ϕ collapse on one single curve while plotting

$$F(\Theta) = \frac{\Delta\eta_{eff}}{\Delta\eta^0_{eff}} \tag{5.31}$$

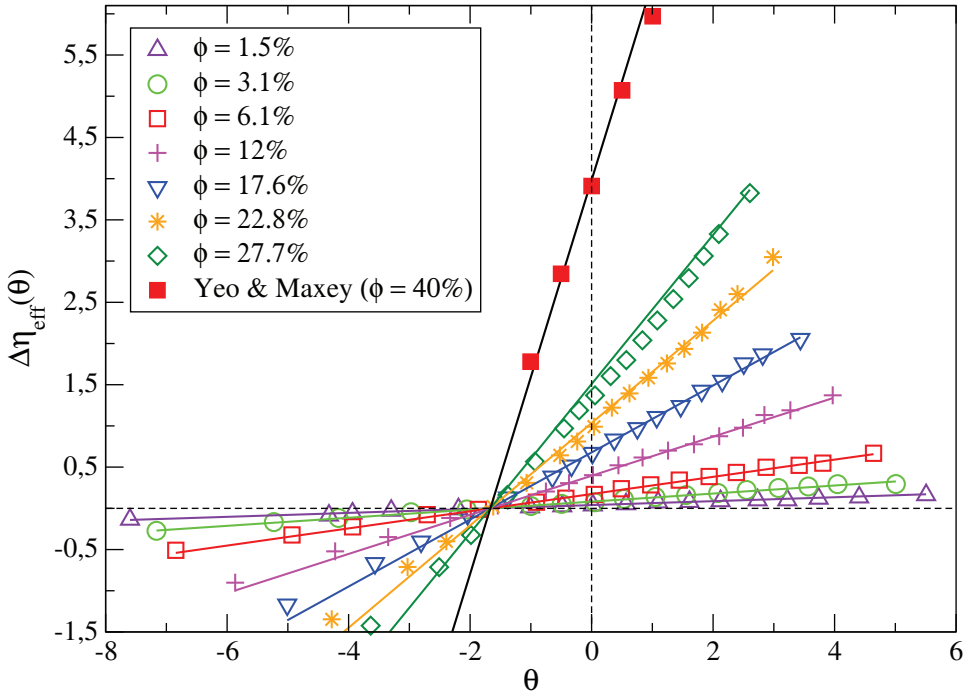

Figure 5.7: Relative effective viscosity as a function of Θ for different values of the volume fraction.

as a function of Θ:

$$F(\Theta) = 1 + \frac{3}{5}\Theta. \tag{5.32}$$

Ratio $F(\Theta)$ of the relative effective viscosities $\Delta\eta_{eff}$ and $\Delta\eta^0_{eff}$ as a function of Θ is shown on figure 5.9 for different values of the volume fraction ϕ. A single master curve is obtained: as predicted by equation (5.32) represented by the straight line. The Yeo and Maxey [17] data are very well fitted by the law (5.32). Note that it is possible to obtain a negative relative effective viscosity for sufficiently high absolute values of Θ (for $\Theta < 0$). This is due to the rotation of particles (for $\Theta < 0$) which increases the shear rate while a negative stress σ_{xy} has to be imposed to maintain the same value of $\dot{\gamma}$. Note that whatever the volume fraction, for the same value of $\Theta = -5/3$ (*i.e.* $< \omega_z >= -4/3\dot{\gamma}$), the contribution of the particles to the effective viscosity can be suppressed by applying a critical torque L_c derived below.

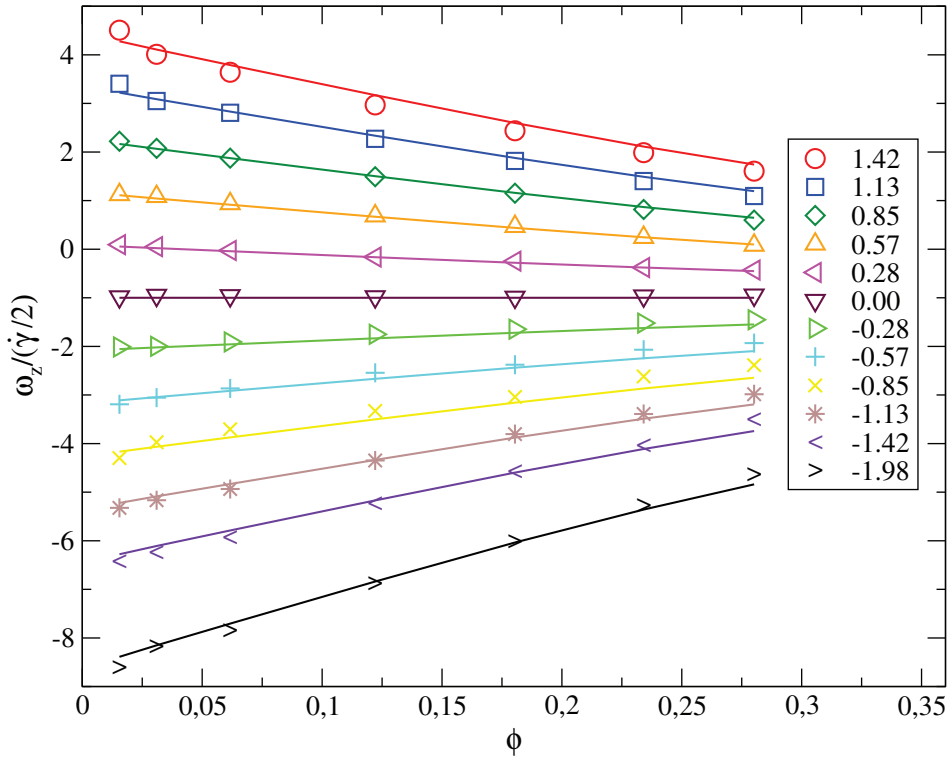

Figure 5.8: Dimensionless angular velocity as a function of volume fraction for several values of the applied dimensionless torque.

5.5.3 Empirically modified second Faxén law

We can also derive the expression of L from an empirically modified second Faxén law. By transposing the expression of $L(\omega_z)$ *i.e.* equation (5.9) in the dilute regime to a concentrated regime, one can write:

$$L = -\frac{12\mathcal{V}}{5N}\left(\eta^0_{eff} - \eta\right)\left[\frac{1}{2}\overline{\mathbf{rotV_0}}|_z - <\omega_z>\right], \tag{5.33}$$

where we have replaced $5/2\phi\eta$ by $(\eta^0_{eff} - \eta)$. This is exact for dilute regimes and empirical for more concentrated regimes. $\overline{\mathbf{rotV_0}}|_z$ is the $z-$component of the vorticity averaged on the total volume of the suspension in the absence of torque [71]. But since we impose a given shear rate, we get:

$$\overline{\mathbf{rotV_0}}|_z = -\dot{\gamma}/2. \tag{5.34}$$

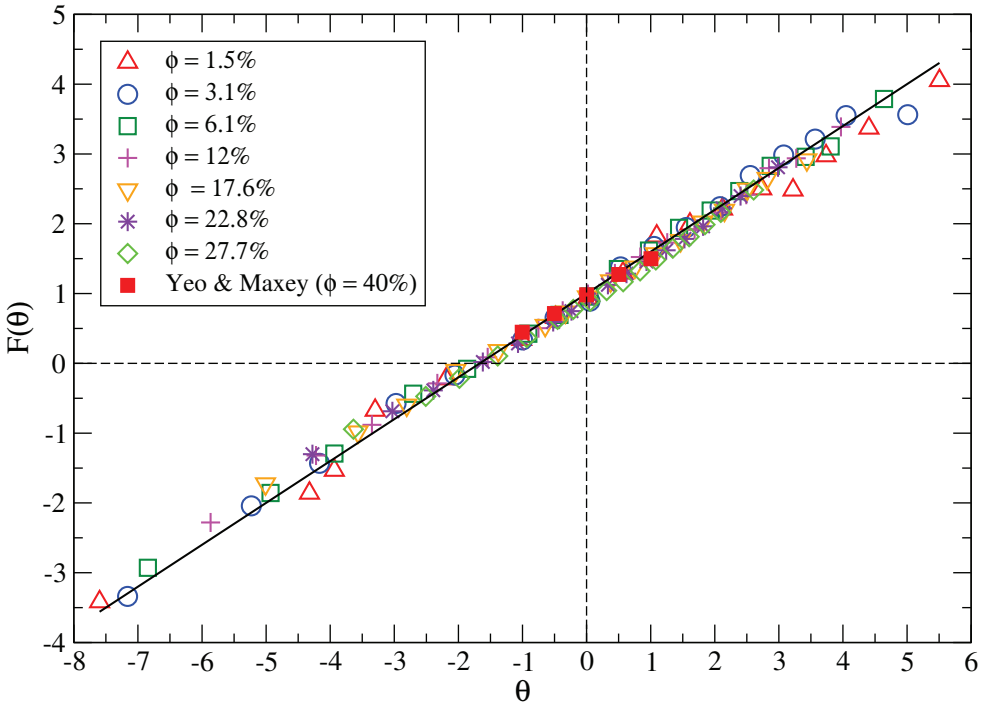

Figure 5.9: Ratio $F(\Theta)$ of the relative effective viscosities $\Delta\eta_{eff}$ and $\Delta\eta^0_{eff}$ as a function of Θ for different values of the volume fraction ϕ.

Thus we can write:

$$L = \frac{12\mathcal{V}}{5N}\left(\eta^0_{eff} - \eta\right)\left(\frac{\dot{\gamma}}{2} + < \omega_z >\right). \tag{5.35}$$

In our simulations, for a given volume fraction, we impose the same value of the torque L on each particle and we calculate the value of ω_z averaged on all the particles. Dimensionless angular velocity as a function of volume fraction for several values of the applied dimensionless torque $L^* = L/(8\pi R^3\eta\dot{\gamma})$ is shown in figure 5.8. The numerical results are indeed very well fitted with equation (5.35). Figure 5.10 shows the values of the torque per particle needed to obtain $\Theta = -5/3$ (*i.e.* $\Delta\eta_{eff} = 0$). When $\phi \ll 1$, L_c tends to a constant value independent of ϕ:

$$L_c = \frac{20}{3}\pi R^3\eta\dot{\gamma}, \tag{5.36}$$

it is the torque per particle that is needed to obtain $\Theta = -5/3$ in the dilute regime.

Yeo and Maxey [17] plotted the total effective viscosity in the presence of a torque

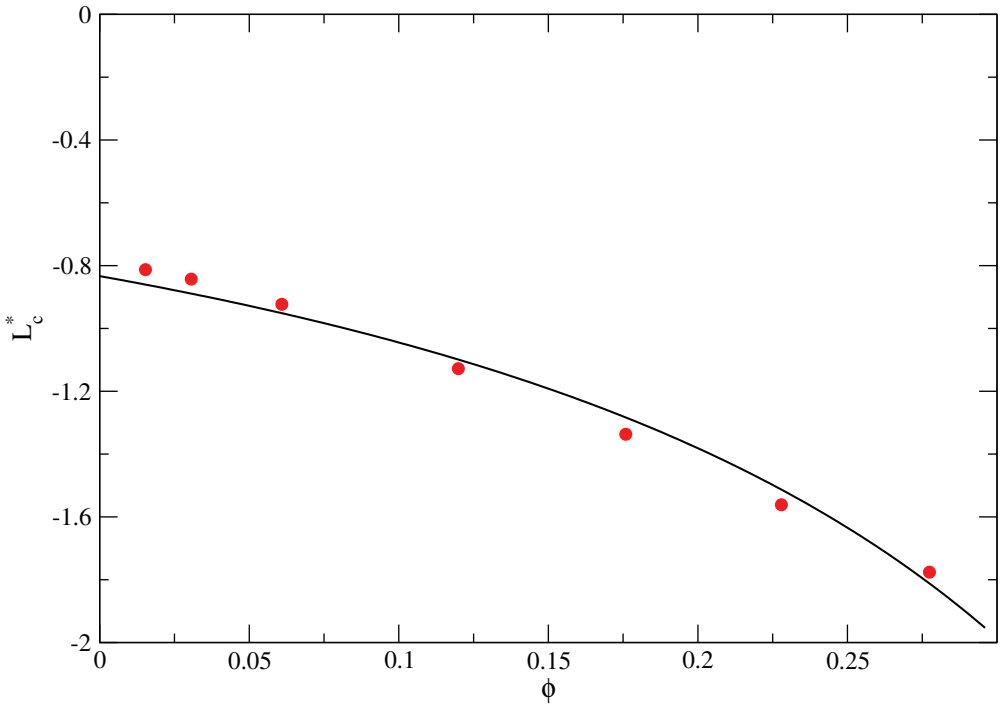

Figure 5.10: Values of the dimensionless torque L_c^* as a function of ϕ for which $\Theta = -5/3$ (*i.e.* $\Delta\eta_{eff} = 0$).

for $\phi = 40\%$ as a function of a non-dimensional value of the torque

$$L^* = \frac{L}{8\pi\eta R^3\dot{\gamma}}.$$

Here, we plot their values as a function of Θ. From equation (5.35), we obtain the following relation between L^* and Θ:

$$L^* = \frac{\Delta\eta^0_{eff}(\phi)}{5\phi}\Theta. \tag{5.37}$$

For dilute regimes ($\phi \ll 1$), it reads $L^* = \Theta/2$, but for higher values of ϕ the relationship (5.37) between the two dimensionless numbers depends on ϕ. For example when $\phi = 40\%$, it gives $L^* \approx 2.0\,\Theta$. Equation (5.35) could be generalized in the

following vectorial equation:

$$\mathbf{L} = -\frac{12\mathcal{V}}{5N}\left(\eta^0_{eff} - \eta\right)\left[\frac{1}{2}\overline{\mathbf{rot}\,\mathbf{V_0}} - <\boldsymbol{\omega}>\right]. \tag{5.38}$$

Note that expression (5.38) tends to the usual second Faxén law (5.9) for dilute regimes, *i.e.* when $\phi \ll 1$.

We can recover the expression (5.29) of the relative effective viscosity in presence of a torque for high concentrations. The xy-stress being given by

$$\sigma^R_{xy} = \frac{N\,L_z}{2\mathcal{V}} = \frac{6}{5}(\eta^0_{eff} - \eta) < \Omega >, \tag{5.39}$$

and by using

$$\eta_{eff} = \eta^0_{eff} + \eta^R_{eff} \tag{5.40}$$

with

$$\eta^R_{eff} = \frac{\sigma^R_{xy}}{\dot{\gamma}} \tag{5.41}$$

we obtain:

$$\eta_{eff} = \eta^0_{eff} + \frac{3}{5}(\eta^0_{eff} - \eta)\frac{< \Omega >}{\dot{\gamma}/2}, \tag{5.42}$$

which is equivalent to the expression (5.29).

5.6 Conclusions

In this chapter, we show that we can tune the effective viscosity of a sheared suspension of neutrally buoyant spherical particles if they are sensitive to an external torque that modifies their rotation. The competition between the two effects (shear flow and torque) is well described with the dimensionless number Θ representing the relative angular velocity of the particles divided by the vorticity of the shear flow. Enhancement and reduction of the shear-effective viscosity are found and depend on the applied torque intensity and sign. For a given value of the mean angular velocity of the particles ($< \omega_z >= -4/3\dot{\gamma}$) which is independent of the volume fraction, the contribution of the particles to the effective viscosity can be suppressed and the effective viscosity of the suspension becomes equal to the viscosity of the solvent. An empirical formula

is proposed for the effective viscosity of the suspension which fits remarkably well the data. We can recover this law by using an empirical second Faxén law adapted to more concentrated regime (up to 40%).

Chapter 6

Models and numerical simulations of *Chlamydomonas* micro-swimmer suspensions

In this chapter, we review two types of micro-swimmers, "pullers" and "pushers" and some low Reynolds numbers constrains. Then, we briefly introduce our experimental observations concerning the rheology of *Chlamydomonas* micro-swimmer suspensions. Namely, the increase of the effective viscosity of sheared suspensions of live unicellular motile micro-algae compared to the effective viscosity of suspensions containing the same volume fraction of dead cells and a shear thinning behavior [9]. Different possible mechanisms are considered which can be involved in this phenomena. We present our models and numerical simulations results which are compared to the experimental results and we explain the experimentally observed phenomena. Our model which converges to anisotropic distribution of the force dipoles provides a good agreement with the experimental results. The model is extendable for pusher type micro swimmer suspensions where the opposite effect, the decrease of the effective viscosity of active bacterial suspensions was observed experimentally [10].

Dans ce chapitre, nous examinons deux types de micro-nageurs, «tireurs» (pullers) et «pousseurs» (pushers) aux faibles nombres de Reynolds. Nous présentons brièvement nos observations expérimentales concernant la rhéologie de suspensions de *Chlamydomonas*. A savoir, l'augmentation de la viscosité des suspensions cisaillées constituées de micro-algues mobiles (vivantes) par rapport à la viscosité effective de suspensions contenant la même fraction volumique de cellules mortes. Nous étudions également le comportement rhéofluidifiant [9] de ces suspensions. Différents mécanismes possibles sont considérés comme pouvant être impliqués dans ce phénomène. Nous présentons nos modèles numériques et des résultats des simulations qui sont comparés aux résultats expérimentaux et expliquent les phénomènes observés expérimentalement. Notre modèle qui converge vers la distribution anisotrope des particules (forces dipolaires) prévoit un bon accord avec les résultats expérimentaux. Le modèle peut être étendu aux suspensions de type pousseurs où l'effet inverse est observé, c'est à dire la diminution de la viscosité des suspensions actives bactériennes observée expérimentalement [10].

6.1 Introduction

Within the last few years there has been growing interest of soft active systems physics. Examples of such systems represent suspensions of living self-propelled micro-organisms, swimming cells and artificial micro-swimmers [85, 86, 87, 88]. In active suspensions (or "active fluids") living organisms or particles continuously transform chemical energy of surrounding fluids or their stored energy into a mechanical work (locomotion or rotary motion). Because of this feature active suspensions represent a new type of condensed soft mater which have drastically different properties from suspensions of passive inclusions [1]. Typical examples of active suspensions are suspensions of micro-algae, bacterias and sperms [89, 7]. Study of such active systems has fundamental meaning [1] as well as relevance in various potential technological applications [90, 91, 92], in ecology [93] and medicine [94].

Depending on swimming mechanism of each type of micro-swimmers which results in hydrodynamic interactions between swimmers in suspensions, various interesting phenomena have been reported. Among them: complex rheological behavior of micro swimmer suspensions [1, 10, 9]; pattern formation in bacterial suspensions [91, 95]; complex motions, enhanced diffusion and spatial correlation in micro-swimmer suspensions [96, 97, 98, 99]; phototaxis and bioconvection in suspensions of phototactic micro-swimmers [100, 101], etc. In this work, we concentrate ourselves on the study of the rheology of active suspensions. So far only few experimental works have been performed to study the effect of swimming micro-organisms on the rheological properties of suspensions. In 2009 Sokolov & Aranson measured experimentally the effective viscosity of suspension of Bacillus subtilis [10]. They report strong decrease of the effective viscosity (up to a factor of 7). Then, we measured the effective viscosity of sheared suspensions of live unicellular motile micro-algae (*Chlamydomonas Reinhardtii*) and found it much bigger (about a factor of 2) than for suspensions containing the same volume fraction of dead cells [9]. Suspensions of live micro-algae also show a shear thinning behavior. Few theoretical and computational works have been done to explain those experimental observations [102, 103, 104, 105]. Saintillan used simple kinetic model to study the rheology of dilute active suspensions [102]. Heidenreich et al. used analytical approach to study nonlinear rheology of active suspensions [104]. Their results are consistent with previous analytical predictions of Hatwalne et al. [1] and Haines et al. [106]. The

models which takes into account the rod-like shape of Bacillus subtilis, and anisotropic orientation distribution of swimmers are able to describe successfully the decrease of the effective viscosity in bacterial ("pusher" type) suspension [102, 106]. Those models also predict increase of the effective viscosity in "puller" type suspensions. However, the increase of the effective viscosity for micro-algae suspensions based on supposition that swimmers are aligned in the flow is rather difficult, because *Chlamydomonas* has almost a spherical shape (see figure 6.2 a-b) dislike the bacillus subtilis.

In the next section, we review two types of micro-swimmers: "pullers" and "pushers" and the scallop theorem. In section 6.3, we briefly show our experimental result concerning the effective viscosity of micro-swimmer suspensions. Then we discuss our different models to explain the experimental observations and show results of our numerical simulations. We begin with a simple model where the swimmers are represented by isotropically distributed force dipoles (section 6.4). Then we consider a model where non-zero torque is applied by swimmers on the fluid (section 6.5). In section 6.6, we take into account the effect of flagella of *Chlamydomonas* by considering suspensions of objects consisting of three beads (one central big bead (for the body) and two small satellite beads (for flagella)). The last model which converge in anisotropic distribution of force dipole is presented in section 6.7. This model can be extended also for the pusher type micro-swimmer suspensions (some results are present in section 6.7.1). We make conclusion in section 6.8.

6.2 Two types of micro-swimmers

Micro-swimmers can be classified in two broad categories: "pullers" and "pushers" according to the force they exert on the surrounding fluid. Pullers pull the fluid towards them with their flagella along their moving axis and push the fluid perpendicularly (see figure 6.1 a). Pushers push the fluid back with their propellers along their moving axis and pull the fluid perpendicularly (see figure 6.1 b). Pullers are actuated by anterior flagella attached to the "head" of the swimmer with respect to the direction of its stroke averaged self-propelled motion. While pushers are actuated by posterior flagella fixed behind the body.

Figure 6.1 shows the velocity fields and streamlines induced by force dipole of a

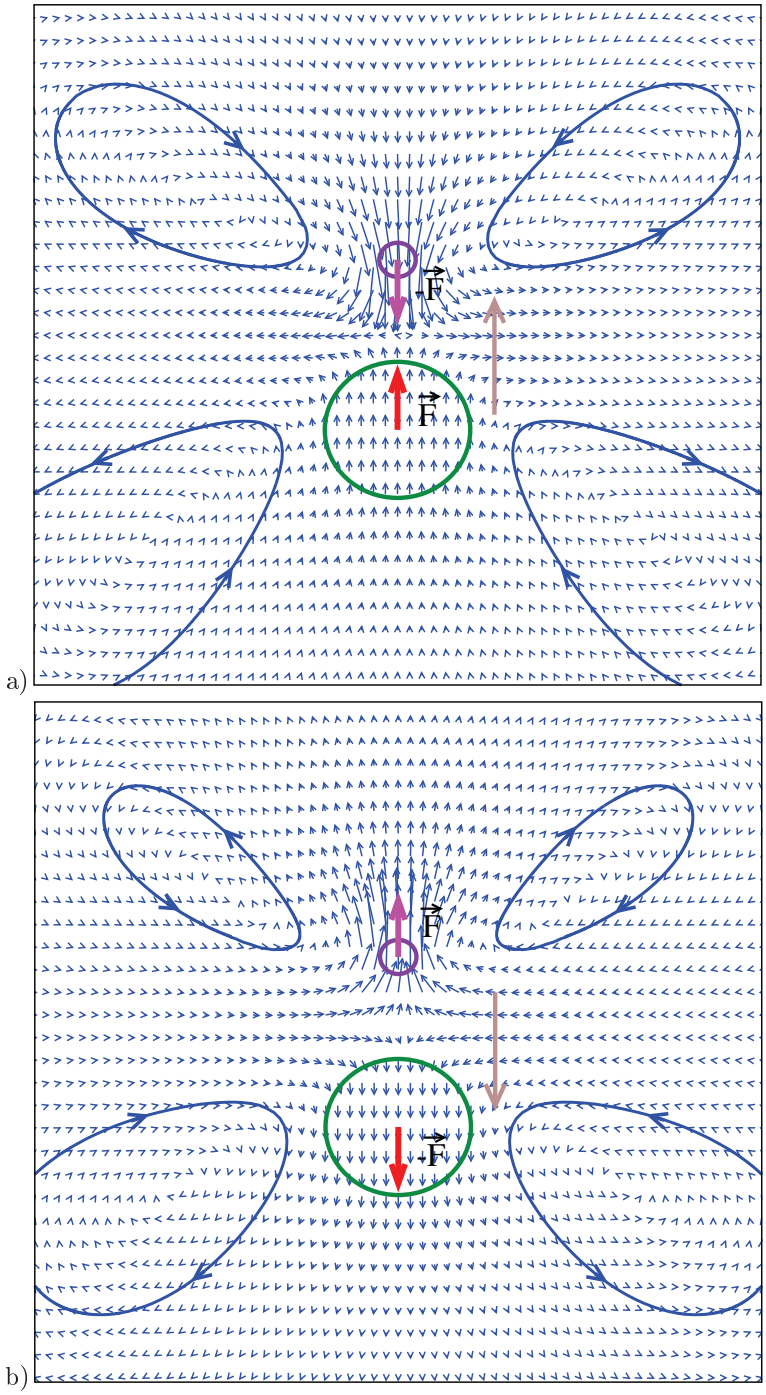

Figure 6.1: Velocity fields and streamlines at the middle crossing plane of two unequal beads with force dipole representing: a) the puller and b) the pusher.

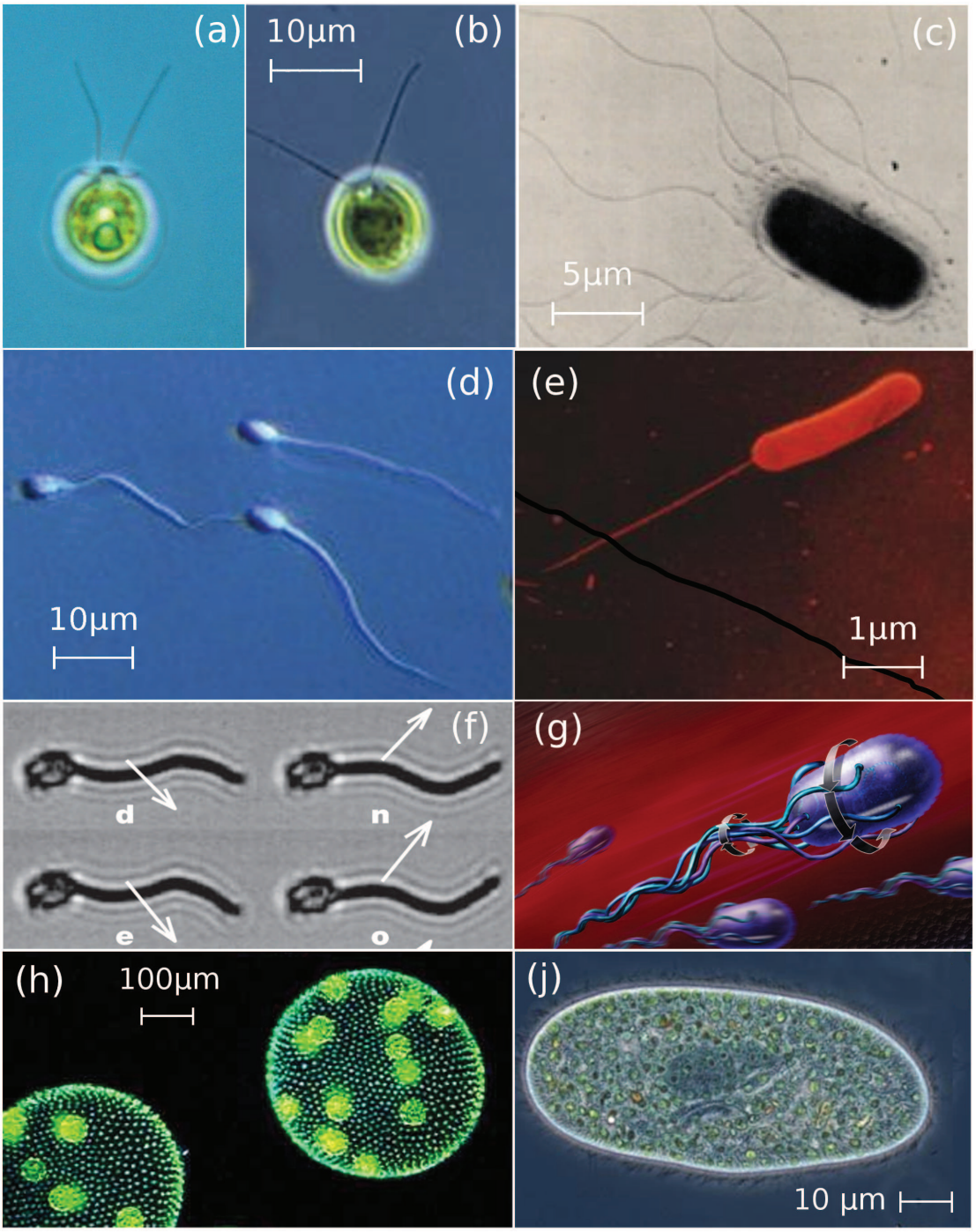

Figure 6.2: Micro-swimmers: a-b) *Chlamydomonas Reinhardtii*; c) Escherichia coli; d) human spermatozoa; e) bacillus subtilis; f) artificial swimmers [85]; g) schematic picture of an artificial micro-swimmers; h) Volvox multi-cellular algae and j) a ciliate.

single a) puller or b) pusher. The self-propulsion direction is indicated by brown arrows. Each swimmer is represented by two unequal beads with radii $R_1 = 6\delta$ (the body) and $R_2 = 2\delta$ (the flagella), here δ is the mesh size. The distance between the centers of beads is 15δ. Two equal and opposite forces F are applied at the centers of the beads.

One prototype of puller type micro-swimmers is *Chlamydomonas Reinhardtii* (CR), a 10 μm motile unicellular alga (see figure 6.2 a-b). Most of bacteria: Escherichia coli; bacillus subtilis, spermatozoa and artificial swimmers [85] are examples of pusher type micro swimmers (see figure 6.2 c-g).

Note that exist other swimming microorganisms, like the ciliates and multi-cellular algae Volvox which do not belong to those two categories of micro swimmers (figure 6.2 j-f).

6.2.1 Low Reynolds number constrains

At the small scales where micro-swimmers live, the viscous forces dominate over inertial forces. As a result there are some constrains on the locomotion of micro-swimmers. Those constrains was well explained in the Purcell's paper ''Life at low Reynolds number'' later known as "The scallop theorem" [7]. The scallop theorem explains that in very viscous fluids or at small scales (at low Reynolds number) locomotion cannot be achieved by sequence of shape which is reciprocal (time reversible). In his discussion Purcell invoked the example of scallop which is an inertial simple swimmer, swimming by sequence of fast opening and slow closing its shells.

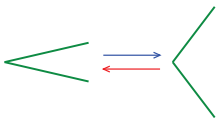

If a scallop swims in a low Reynolds number fluid, it would not achieve propulsion in the fluid (but only a back and fourth motion). Figure 6.3 shows a schematic sequence of a non-reciprocal motion of flagella that a green alga uses to swim at a low Reynolds number [107]. Every individual micro-swimmers at low Reynolds number need to deform itself in non-reciprocal way (not invariant under time reversal) to achieve a locomotion. However, it has been shown that two active particles together which perform a reciprocal motion can break the scallop theorem and swim collectively [108].

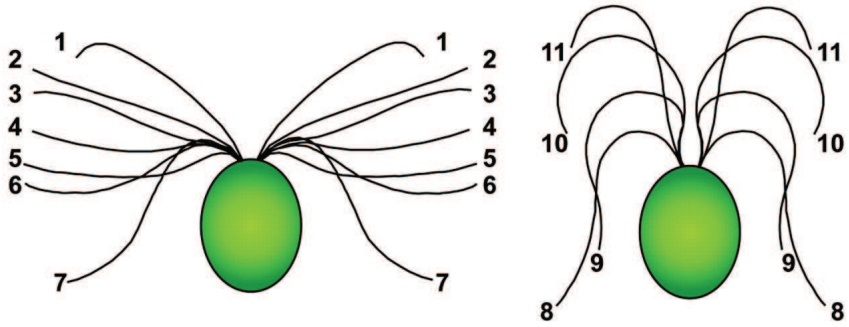

Figure 6.3: Schematic picture of non-reciprocal motion of green alga's flagella [107].

6.3 Effective viscosity of micro-swimmer suspensions: experimental study

In this section, we briefly show our experimental results concerning the rheological properties of active *Chlamydomonas* suspension [9].

We measured the effective viscosity of suspensions of puller-type micro-swimmer *Chlamydomonas reinhardtii*, a $10\,\mu m$ motile unicellular alga. They are spheroidal in shape with two anterior flagella (see figure 6.2 a-b) [107]. Their back-and-forth movement produces a jerky breast stroke with a mean speed of $40\,\mu m/s$ in a water-like viscous medium (figure 6.3). Rheological measurements show a clear increase in the effective viscosity compared to a dead cell suspension. Figure 6.4 shows the relative viscosity $(\eta_{eff} - \eta)/\eta$ of live and dead cell suspensions as a function of the volume fraction. In both cases, viscosity is an increasing function of the volume fraction as it is for passive beads. The effective viscosity of swimming cell suspensions is quantitatively larger than the viscosity of dead cell suspensions (up to a factor of 2 for a 15% volume fraction). Viscosity was measured at a given shear rate of $5\,s^{-1}$.

A shear thinning behavior was also observed. The effective viscosity of active suspensions decreases when increasing the shear rate. Figure 6.5 shows the effective viscosity of *Chlamydomonas* suspensions as a function of the shear rate. Data are shown for different volume fractions of the suspension (up to 25% concentration). The measurements at high enough shear rate (above $\sim 20\ Hz$) show that micro-swimmer suspensions behave

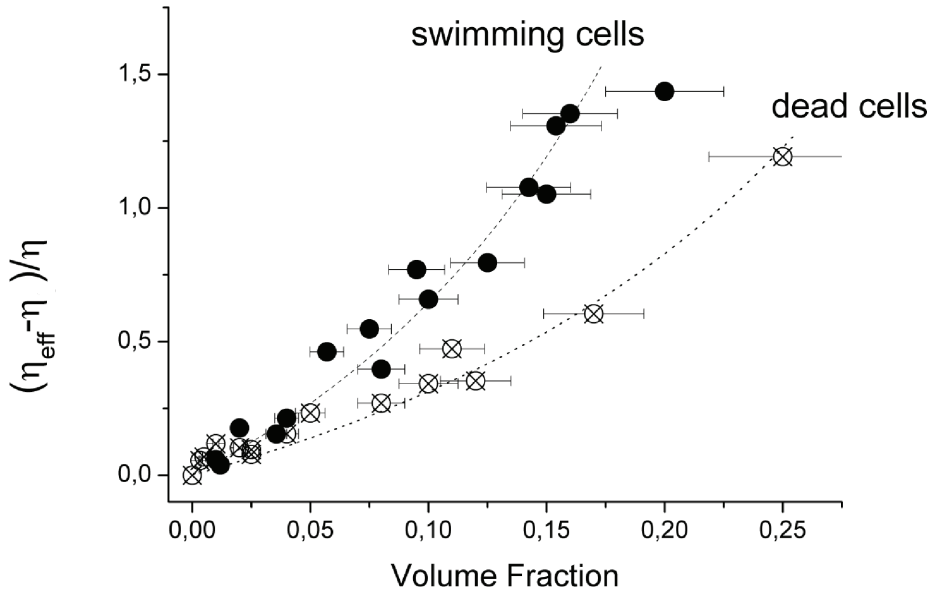

Figure 6.4: Reduced effective viscosity of green algae suspensions as a function of volume fraction

as passive particle suspension.

We also observed that swimming cells behave differently: they resist the flow rotation for most of the time and eventually flip very rapidly. Figures 6.6 a) and b) show picture sequences extracted from a fast-image film for a dead cell and a swimming *Chlamydomonas*, respectively. High frequency acquisition (500 Hz) allows us to determine whether or not an alga is swimming by looking at the beating of the flagella. Time between pictures is 20 ms. Cell diameter is about 10 μm. A dead cell in shear flow experiences tumbling around x axis (figures 6.6 a), whereas flagella of swimming cells beat at about 50 Hz. Here Oz is the direction of observation, yOz is the shear plane. Time sequences of cells subjected to a 10 s^{-1} shear rate is 50 Hz. The swimming cell spends about two thirds of the period in the xOy plane and flips during one third of the period whereas the dead cell rotates at a constant velocity close to $\dot{\gamma}/2$ (figures 6.6 b).

In following sections, we explore different models to understand the mechanism be-

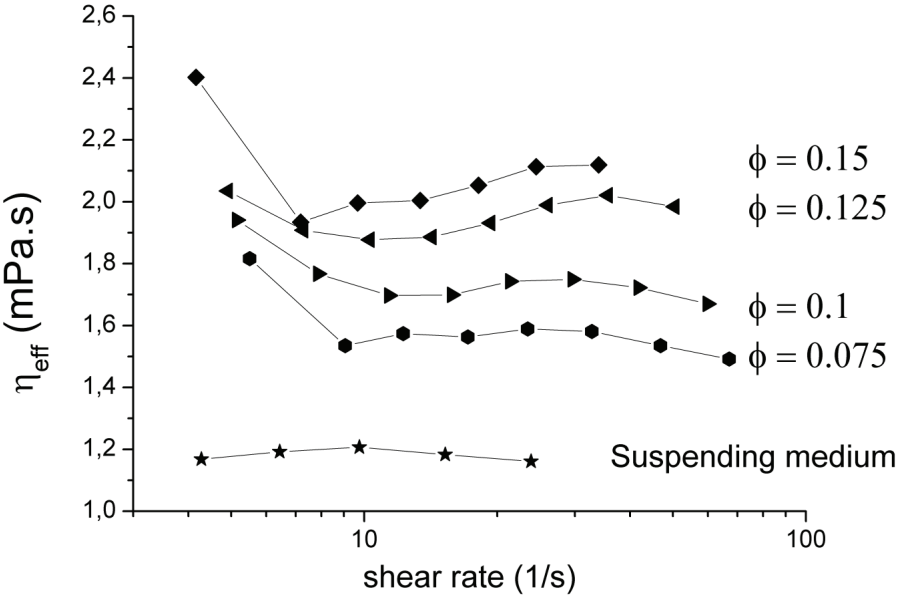

Figure 6.5: Effective viscosity of *Chlamydomonas* suspensions as a function of the shear rate.

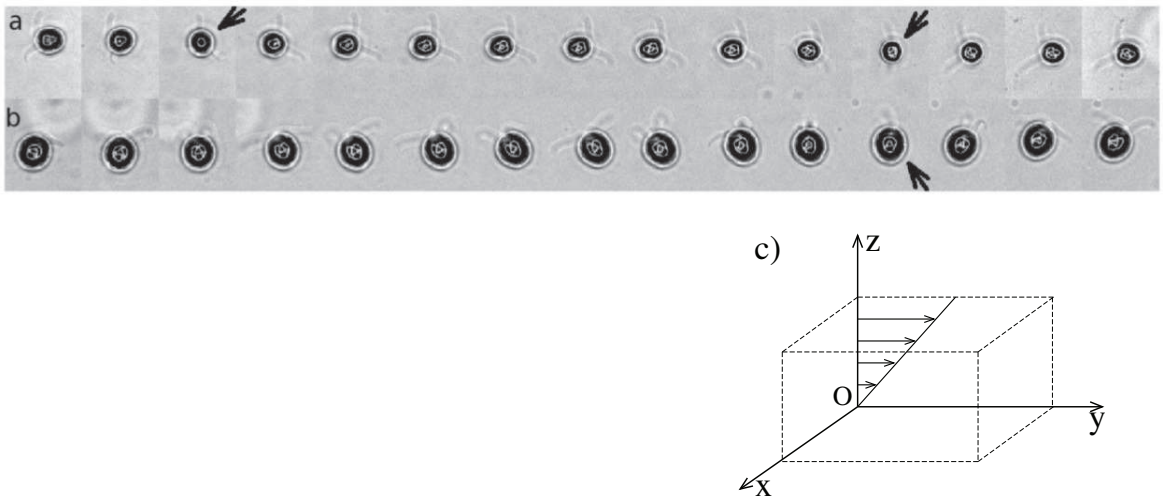

Figure 6.6: a) Dead and b) live *Chlamydomonas* in the same shear flow. c) Schematic view of the flow cell (Oz is the direction of observation).

hind those observed phenomena.

6.4 Simple model with the force dipole

Initially, we consider a simple model where a live self-propelled micro-alga is replaced by a rigid sphere with a force dipole (see figure 6.7 a). If the density of particles is equal to the density of fluid, gravity can be neglected and particles are force-free. When particle moves in a fluid the propulsive force must be equal to the viscous drag on the body. A force free particle can exert on the fluid a force dipole (or higher multipoles). Exact simulation of *Chlamydomonas* movement can be extremely difficult, since during their back-and-forth movement, flagella deform in a complex non-reciprocal manner (see figure 6.3). But flagella beating frequency is high enough (about $50\,Hz$) and the force exerted by *Chlamydomonas* on the surrounding fluid can be approximated by a force dipole, which is a time averaging of the instantaneous force distribution exerted by flagella during one period of their stroke. On figure 6.7, we show: a) schematic diagram of a force dipole used in this section; b) the velocity field exerted by this force dipole associated with rigid body on the fluid at rest; c) the streamlines calculated using our numerical velocity field and d) experimentally obtained streamlines by Drescher et al. [109]. The spiraling of streamlines near the elliptic points are numerical artifacts caused by direct integration of the discrete velocity fields.

To study the influence of the self-motility of micro-swimmers on the rheological properties of a fluid, we simulate suspensions of rigid spherical particles with those force dipoles (figure 6.8). Suspended mono-disperse spheres with a radius $R = 3\delta$, ($a = 2\delta$ and $\xi = 0.5$), are randomly and homogeneously distributed initially without any overlap between them in the simulations cell with dimensions $\ell_x = \ell_y = \ell_z = 60\delta$. Here δ is the mesh size. A randomly and isotropically distributed force dipole of amplitude F is associated with each particle. The shear flow with the velocity $\mathbf{v}(0,\, 0,\, \dot{\gamma}x)$ and fixed shear rate $\dot{\gamma}$ is imposed in the xOz plane while the periodic boundary conditions are used in y and z directions (figure 6.8). Figure 6.8 shows the diagonal view of the simulation cell with 100 active particles. The arrows indicate direction of the forces applied on the rigid body which is also the direction of self locomotion. The counter forces applied on the fluid are not shown for simplicity. The Fluid Particle Dynamics

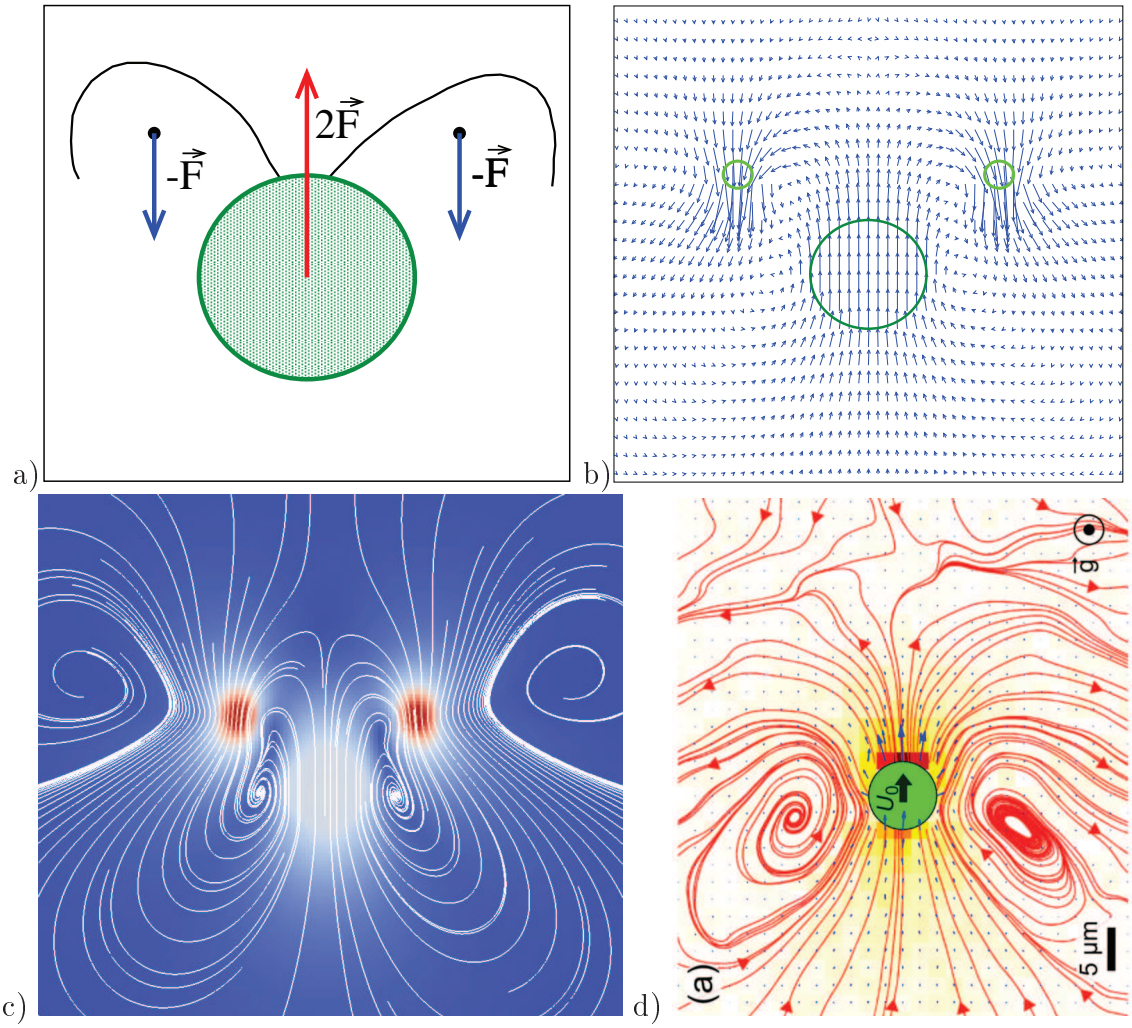

Figure 6.7: a) The schematic diagram of the force dipole used in this model. b) The velocity field. c) Numerically obtained streamlines and d) streamlines obtained experimentally by Drescher et al. [109].

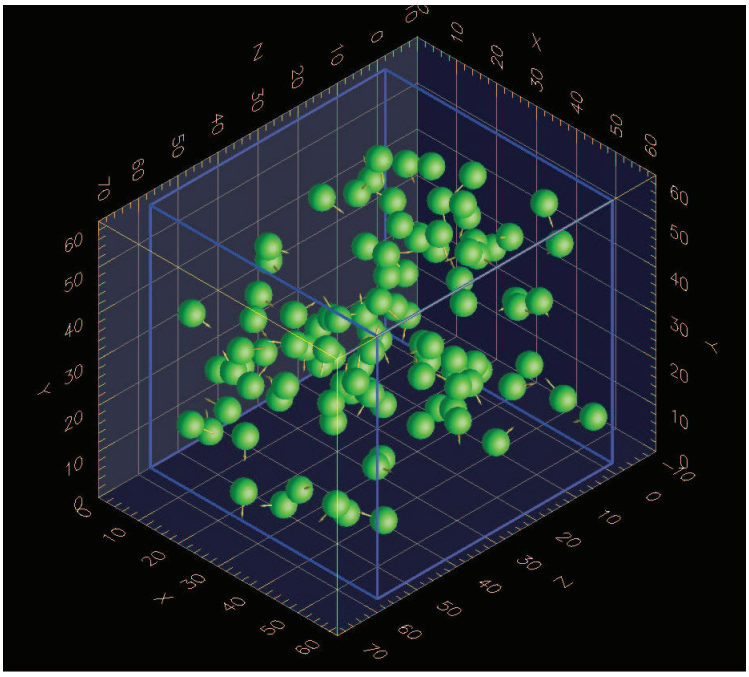

Figure 6.8: A view of 100 active particles in the simulation cell.

(considered in chapter 3) is used to simulate the dynamics of these active particles.

We simulate different numbers of suspended particles up to 20% concentration and calculate the effective viscosity of suspensions using the velocity field (see equation 5.22 in previous chapter). The results of our simulations compared to the effective viscosity of rigid spherical particle suspensions are show on figure 6.9. Full red circles are numerical results for active particle suspensions. Red line is just a guide for the eyes. Full green squares are the effective viscosity for the same suspensions without the force dipole ($F = 0$). The green solid line is Kreiger & Dougherty's semi-empirical law [78]. Dotted line is Einstein's effective viscosity [75] and dashed line represents the effective viscosity with the second order term of volume fraction [79]. The force dipole used in this model produces motility of particles in the fluid with the velocity of about $v \simeq 3.3 \times 10^{-5}\delta/dt$ for $F = 5$, where dt is the iteration time step, δ is the mesh size and F is the amplitude of the force applied on the particles and fluid (see figure 6.7 a). The suspensions of active particles reveal a ballistic regime (Mean square displacement (MSD) proportional of t^2, here t is the time) at small time scale and a diffusive regime

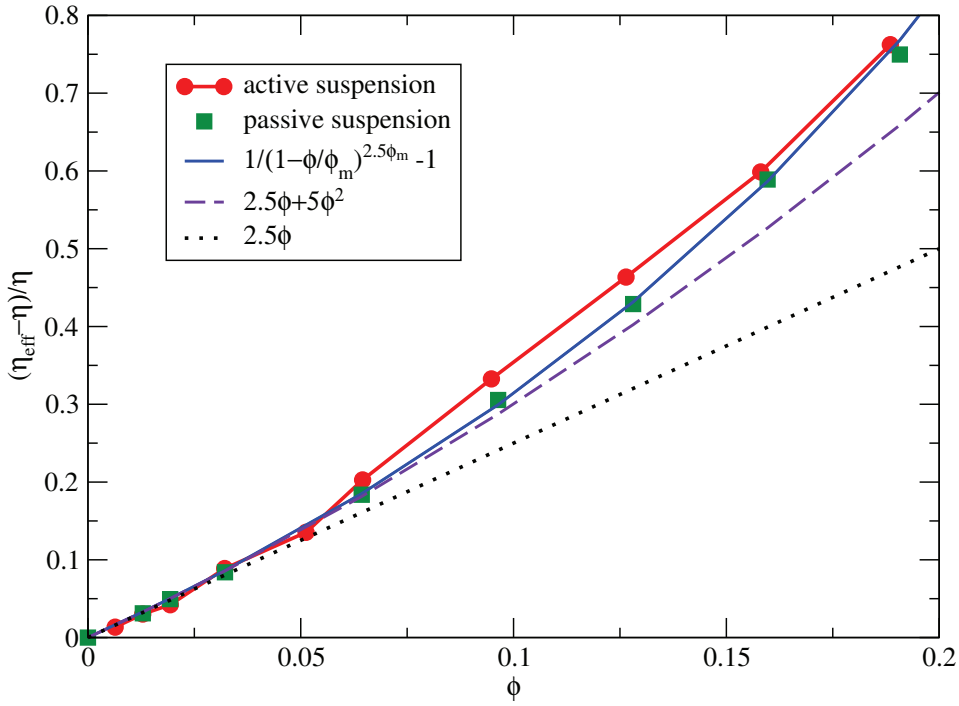

Figure 6.9: The reduced effective viscosity of active particles suspension as a function of volume fraction compared to viscosity of passive particles suspensions.

(MSD proportional to t) at a larger time scale [98]. However, the effective viscosity of active particle suspensions is very close to the one of passive suspensions, as we can see on figure 6.9 which differ from experimental observations (see figure 6.4). A similar result was obtained by Ishikawa and Pedley when they show no direct contribution of non-bottom-heavy squirmers to the bulk stress [67]. Within a numerical fluctuation the effective viscosity also does not change with shear rate. This is due to the fact that the spherical particles are oriented in all the directions. Thus, there is no mean contribution to the shear stress and then there is no variation in η_{eff} due to individual swimming.

6.5 Torque involved model

Next model was inspired by our experimental observation where it has been found that swimming *Chlamydomonas* resist the tumbling motion in the shear flow (figure 6.6).

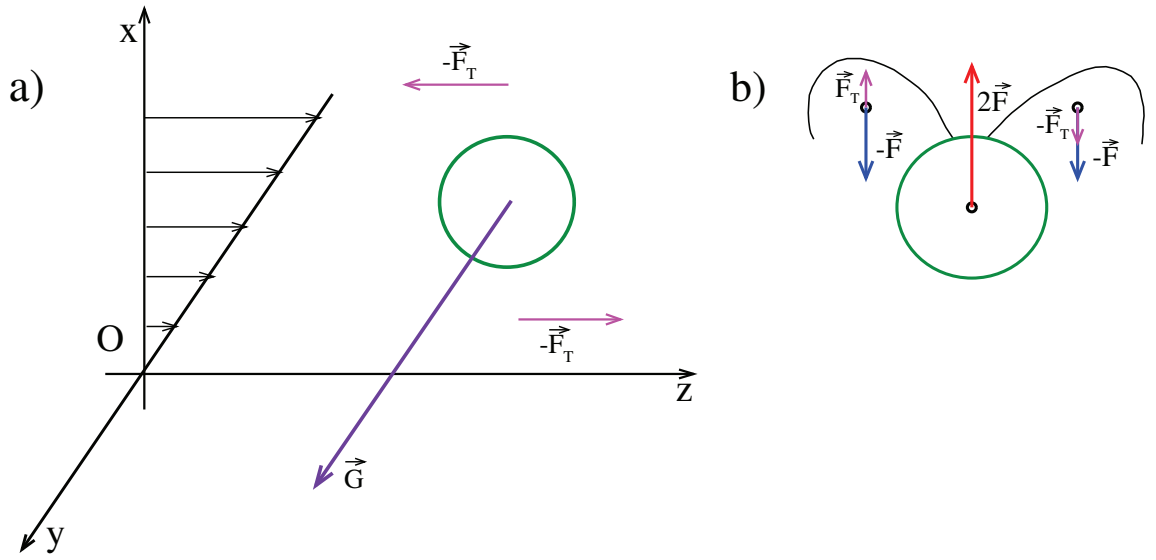

Figure 6.10: a) Schematic diagram of applied torque in a shear flow. b) The applied torque with a force dipole.

Within this model, we force the particles to maintain their initial random orientation in the flow. For this purpose, we applied a torque opposite to the one imposed by the shear flow on each particles. Figure 6.10 shows the schematic diagram of the torque applied to a single particle in the shear flow. In addition to the torque, isotropically distributed force dipole is associated with each particles, as we showed in the previous section (figure 6.10 b). For the simulations, we used FPD method. All the parameters of suspensions and numerical procedure used in this model are similar to the one described in previous models (section 6.4). The torque on each particles is added using two parallel and opposite forces $\mathbf{F}_T$ applied at the same points as outer parts of the force dipole acting on the fluid (see figure 6.10 b). The force dipole (the force $\mathbf{F}$) may have any orientation in space, while $\mathbf{F}_T$ is always in xOz plane, so that $\mathbf{F}_T$ is parallel to the projection of $\mathbf{F}$ on xOz plane. The amplitude of the force $\mathbf{F}_T$ is proportional to the angular velocity of the particle in the shear flow

$$F_T = -4\pi\eta(a+\xi)^2\omega_y,$$

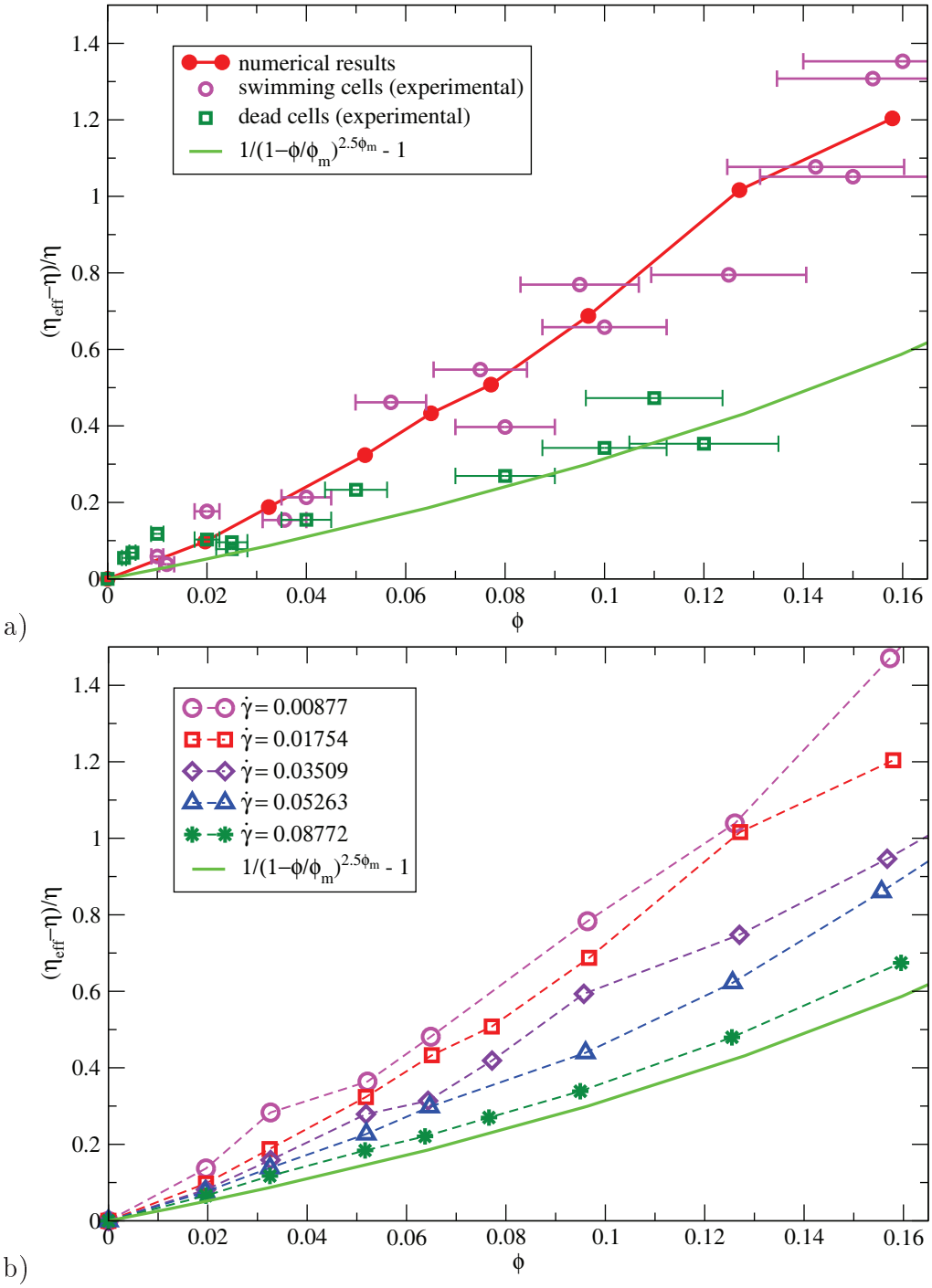

Figure 6.11: a) The reduced effective viscosity of active particles suspension sensitive to a torque as a function of volume fraction compared to viscosity of passive particles suspensions. b) The reduced effective viscosity for different shear rate.

where $a = 2\delta$ are $\xi = 0.5\delta$ are the radius of the particle and the fluid-particle interface thickness, respectively (the effective radius $R \simeq a+2\xi = 3\delta$); $\eta = 1$ is the fluid viscosity; ω_y is the vorticity calculated inside the particle around the y axis. At a given shear rate $\dot{\gamma}$, the applied torque produces $< \omega_y > \simeq 0$ (rotation of particles almost stopped using the counter torque), here the symbol $< . >$ denotes averaging on the set of particles. The active suspension with the torque shows a rheological signature very similar to the one observed experimentally. This results are consistent with our results concerning the shear viscosity in presence of an external torque show in chapter 5. The results are also in agreement with the work of Ishikawa and Pedley on the bottom-heavy squirmers [67].

If a fixed torque is applied on the particles by increasing $\dot{\gamma}$ the torque starts to be too weak to counter the rotation imposed by the shear flow and the particles become passive. So, an increase of the shear rate decreases the effective viscosity and a shear thinning effect is numerically observed consistently with the experiments (figure 6.5). Figure 6.11 a) shows the reduced effective viscosity of the active particle suspension with the torque as a function of the volume fraction. The numerical results (full red circles with solid red line) are compared to the experimental results [9] for active cell suspensions (magenta circles with the error bars) and with the experimental results for dead cells suspension (green squares with the error bars), fitted by Kreiger & Dougherty's semi-empirical low (light green line) [78]. On figure 6.11 b) the reduced effective viscosity as a function of ϕ is shows for different values of $\dot{\gamma}$.

In this model particles with the force dipole and the torque are still force-free, but not torque-free. The model can incorporate all essential points of the experimental observations (increase of the effective viscosity of active particle suspensions, shear thinning and the resistance of the swimmers to the tumbling motion imposed by the shear flow). However, there is not a well-founded reason to impose an external torque on the particles. Only candidate of the external torque on the *Chlamydomonas* is gravity if we take into the account that center of mass and the geometric center of *Chlamydomonas* is shifted [107]. Although, to our knowledge, there is not direct experimental evidence proving effects of gravity of the *Chlamydomonas* swimming (at least in our experiments). Besides that, the difference between *Chlamydomonas* center of mass and the geometric center cannot explain different rheological and mechanical behavior of alive and dead

cells.

6.6 Three beads model

In our previous models a *Chlamydomonas* was considered as a single spherical body. The effects of flagella was reflected only through the forces exerted by them. The drag of the flagella was not taken into account which could play an important role in maintaining its fixed orientation. In the model presented in this section, we modeled *Chlamydomonas* as an object consisting of three beads ($3B$), where one central bead represents the body of the *Chlamydomonas* and two smaller beads represent the flagella (we replace fiber-like flagella by a spherical bead only for purpose of simplicity). Each of the two small satellite beads with the effective radius $R = 2\delta$ ($a = \delta$; $\xi = 0.5\delta$) are connected to the central bead with effective radius $R = 4\delta$ ($a = 3\delta$; $\xi = 0.5\delta$) using three springs (see figure 6.12 a). Figure 6.12 shows: a) the exact scheme of the three-bead object with springs, brown dots indicate grid points (distance between two neighbor points is $\delta = 1$); b) the view of 30 "active" $3B$ objects in the simulation cell submitted to the shear flow (xz is the shear plane). The holder springs: CL and CR on figure 6.12 a) corresponds to flagella of *Chlamydomonas* which are flexible but cannot elongate too much. Therefore the holder springs are rather stronger than the two support springs of each small beads: A_LL, B_LL, A_RR and B_RR.

When a *Chlamydomonas* is "alive" the flagella are situated in front of the body, while in the case of "dead" cell, flagella are only binded to the body and follows freely the body as it rotates. In this model, live cells are considered as the $3B$ objects where springs are strong enough to maintain the small beads in front of the central bead in a given flow (here such objects are called "active"). For the passive objects, we remove support springs (blue lines on figure 6.12 a) by taking the spring constant equal to zero. Then the satellite beads can freely move in a vicinity of the central bead but cannot be separated from it.

We simulate the shear flow on $3B$ objects suspensions by using FPD method. The "active" object suspension shows rheological behavior very similar to the one observed in the experiments on green alga suspensions. Figure 6.13 a) shows the reduced effective viscosity as a function of ϕ. The numerical results for "active" object suspensions (full

a)

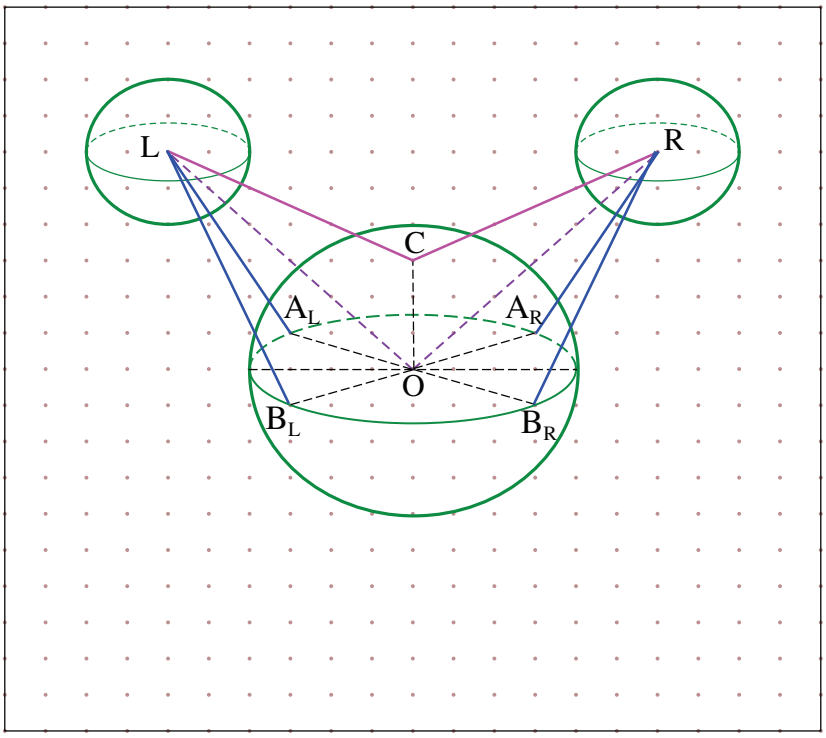

b)

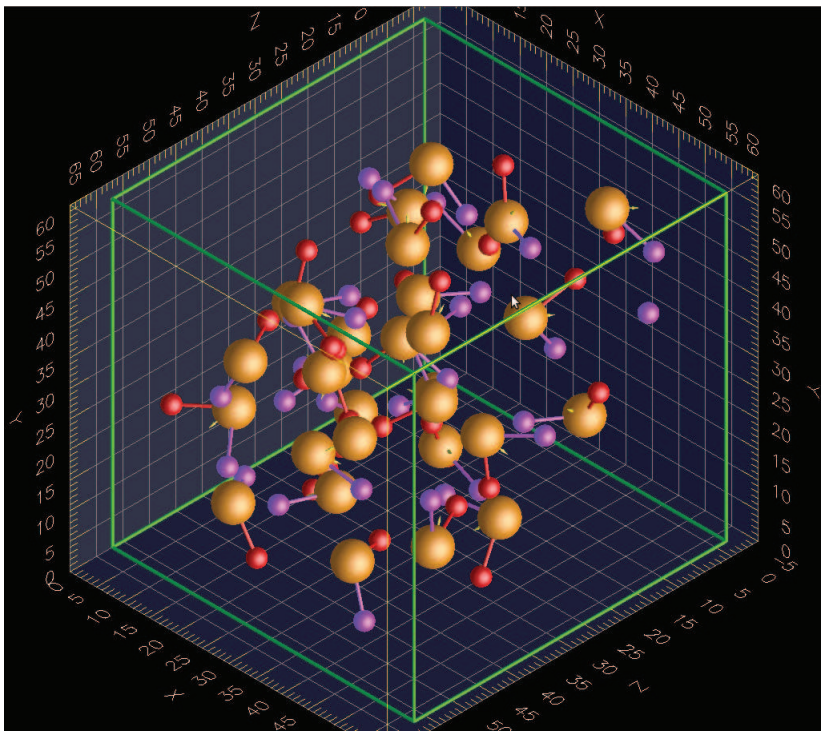

Figure 6.12: a) The exact scheme of the object consisting of three beads. b) View of 30 "active" $3B$ objects in the simulations cell.

red circle) and the numerical results for passive objects suspensions (full green squares) are fitted by Kreiger & Dougherty's semi-empirical law [78]:

$$\eta_{eff} = \frac{\eta}{(1-\phi/\phi_m)^{\alpha\phi_m}},$$

with $\alpha = 4$ (red line) and $\alpha = 2.5$ (green line), respectively. The numerical results are compared to the experimental measurements: magenta circle with error bars for swimming cells and green squares with error bars for dead cells.

For given spring constants, if we increase the shear rate the support springs become weak enough to maintain small beads in front of the central bead (the holder springs are much stronger compare to the support springs), therefore a shear thinning is observed. On figure 6.13 b) the effective viscosity of "active" objects suspensions are shown as a function of the Weissenberg number $Wi = \dot{\gamma}\tau$ for several volume fractions, here $\dot{\gamma}$ is the shear rate and τ is the relaxation time of an elongated $3B$ object. The numerical results are fitted by a power series (solid lines on figure 6.13 b). To calculate τ, we deviate the small beads from their equilibrium position in the "active" 3B object and calculate the $\widehat{LOR}$ angle (figure 6.12 a) as function of the simulation time while small beads return to their equilibrium position. Then, τ is calculated by exponential fitting of the relaxation curve (the $\widehat{LOR}$ angle as function of the time). In the shear flow, rotation of "active" $3B$ object is not uniform, unlike to the passive object and is similar to the Jeffery's rotation of an ellipsoidal body [54]. The $3B$ object spends relative longer time when beads are situated along the flow direction. As an elongated object the "active" $3B$ object somewhat resists the rotation imposed by the shear flow. So, the present model as well as the previous model (with torque) can explain the experimental observations. The shortcoming of this model is that it does not produce a swimmer. The "active" objects as well as the passive objects both are passive, since they do not actuate themselves through a fluid at rest.

6.7 Model with anisotropic distribution of force dipoles

The measurements of the effective viscosity of green-alga suspensions was made using a rheometer which creates a uniform shear flow at the micro-swimmer scale. It is well known that a shear flow can be decomposed into a extension/compression and a

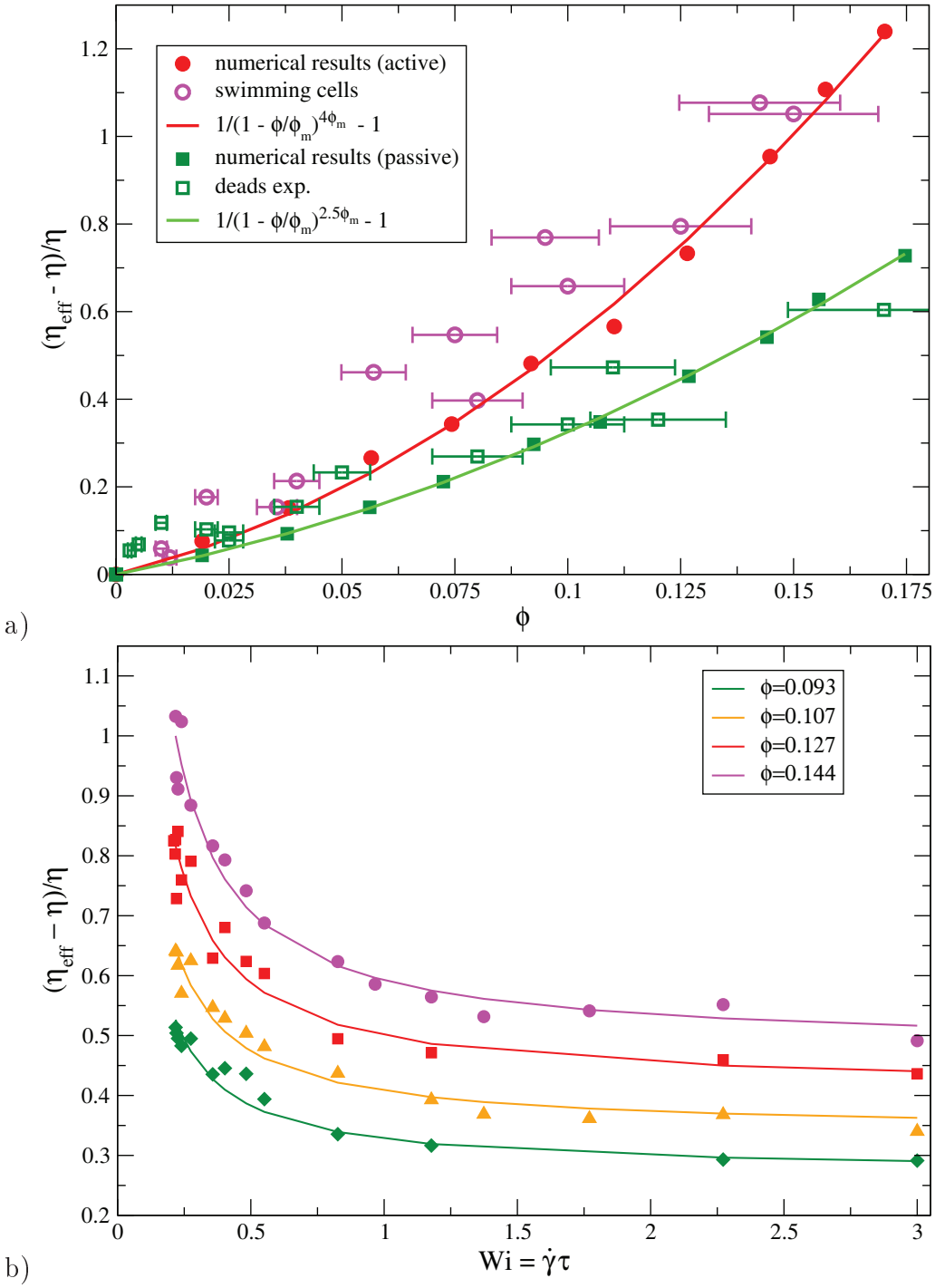

Figure 6.13: a) The reduced effective viscosity of "active" $3B$ objects suspension and passive particles suspensions as function of volume fraction. b) The reduced effective viscosity versus Weissenberg number for different values of volume fractions.

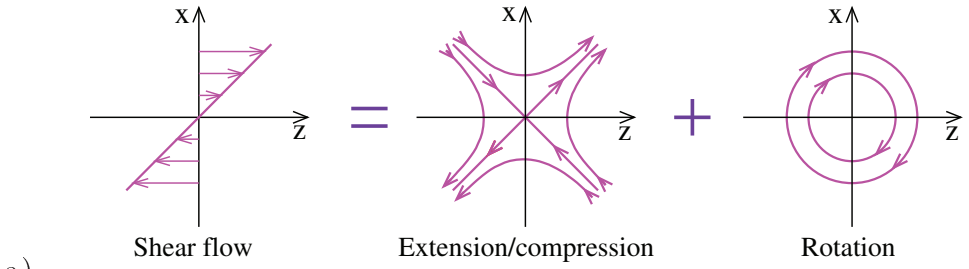

a)

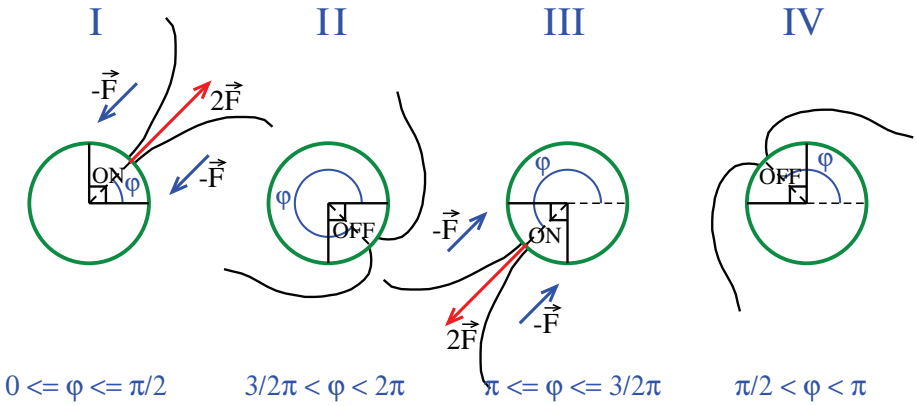

b)

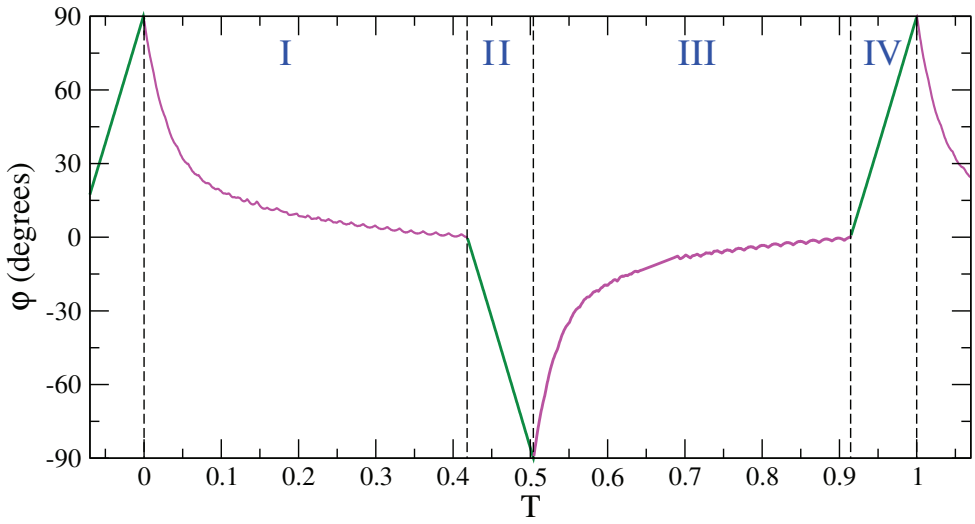

c)

Figure 6.14: a) A shear flow decomposed into the extension/compression and the rotation parts. b) Schematic picture of four situations of *Chlamydomonas* in the shear flow. c) The simulated orientation angle of the fastening point as a function of time.

solid rotation parts (see figure 6.14 a). If we place an object into the shear flow it will experience: the extension in the direction which is at 45° from the flow direction (in the shear plane), the compression along perpendicular direction to the extension direction and the rotation. Therefore, objects with a rod-like shape will orient preferentially along the extension direction in the shear flow. The *Chlamydomonas Reinhardtii* are almost spherical cells (figure 6.1 a-b), therefore they would not have a preferred orientation in the shear flow. However, *Chlamydomonas* has a pair of flagella which are about $10 - 12\ \mu m$ in length and $0.5\,\mu m$ in diameter [107]. *Chlamydomonas* moves through the fluid using rapid (about $50\,Hz$) strokes of these fiber-like flagella.

Our model presented in this section is based on an assumption: a *Chlamydomonas*, as a puller type micro-swimmer in a shear flow, can operate with its flagella when flagella are oriented along the extension direction rather than along the compression direction. Here φ is the angle between the vector which connects body center to the fastening point and horizontal axis (z on figure 6.14 a). On figure 6.14 b) it is shown the four situations of *Chlamydomonas* in a shear flow used in this model. (I) When the fastening point (the point where flagella are bind to the body) is in the first quarter ($0 \leq \varphi \leq \pi/2$) the extension force imposed by the shear flow on flagella helps to open them and *Chlamydomonas* effort is efficient for locomotion. (II) In the second quarter ($3/2\pi < \varphi < 2\pi$) the compression force pushes flagella close to the cell body, therefore *Chlamydomonas* need more effort to open flagella. (III) In the third quarter ($\pi \leq \varphi \leq 3/2\pi$) the extension force is acting on *Chlamydomonas* again and situation is similar to the situation in the first quarter. (IV) In the fourth quarter ($\pi/2 < \varphi < \pi$) situation is similar to the situation in the second quarter.

Based on those particular features of the *Chlamydomonas* swimming, we conclude that on average the amplitude of the force dipole exerted by *Chlamydomonas* on the fluid is bigger when flagella are directed along the extension direction than when flagella are directed along the compression direction. In our simulations for simplicity, we choose nonzero amplitude (ON) of the force dipole in the extension directions (I and III situations on figure 6.14 b) and zero amplitude (OFF) of the force dipole in the compression directions (II and IV situations on figure 6.14 b). In the beginning of simulations, orientations of the force dipoles are randomly and isotropically distributed in the shear plane. The particles are submitted to the shear flow which rotates them

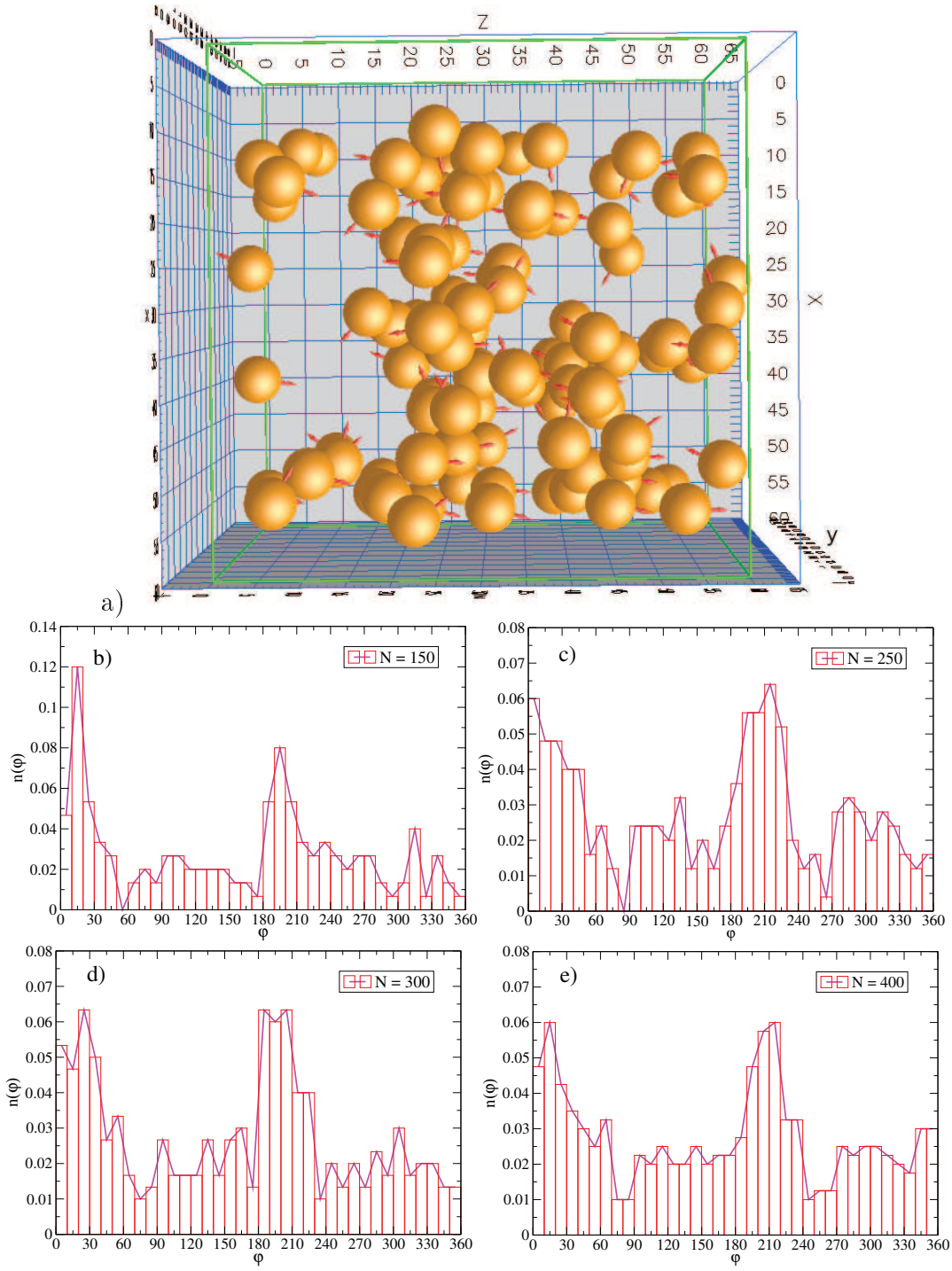

Figure 6.15: a) View of 100 active particles in the simulation box. Normalized number of particles having the orientation angle in the $[\varphi;\, \varphi + 10°]$ interval as a function of φ: b) $N = 150$, c) $N = 250$, d) $N = 300$ and e) $N = 400$.

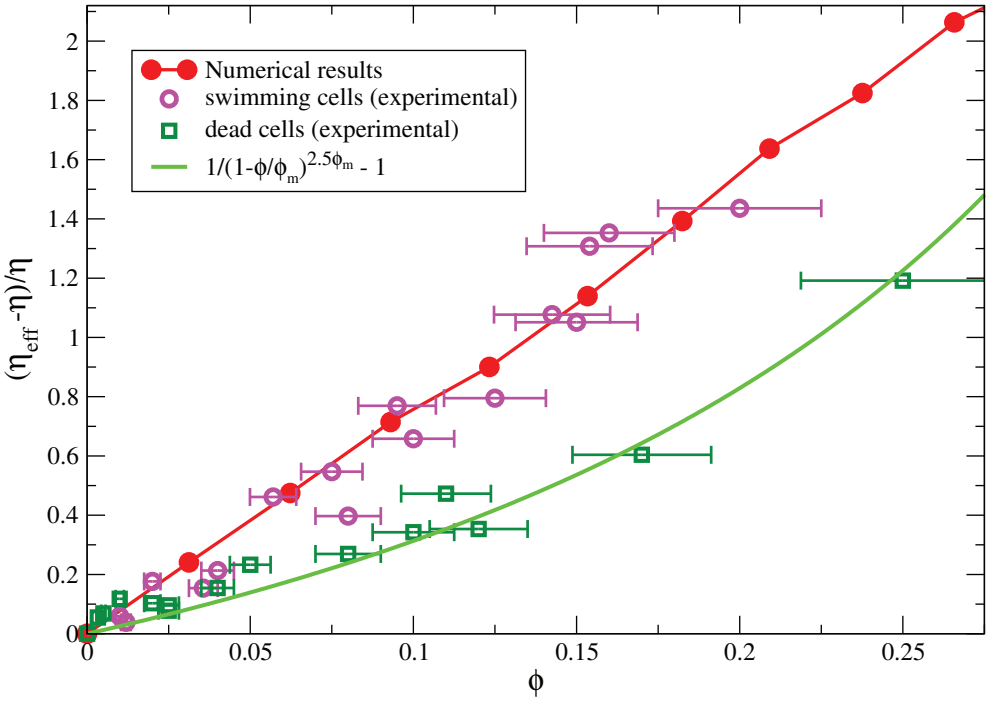

Figure 6.16: The reduced effective viscosity of active suspension with anisotropic distribution of force dipoles versus volume fraction.

clockwise with the angular velocity $\omega_y = -\dot{\gamma}/2$, where $\dot{\gamma}$ is the shear rate. The fastening point rotates with particle but force dipole is applied on particle only in first (I) and third (III) quarter and direction of force is parallel to the extension direction ($45°$ from the flow direction in the first (I) quarter and $135°$ from the flow direction in the third (III) quarter). Therefore, when the fastening point is approaching to the horizontal axis ($\varphi \to 0$) in the first quarter and ($\varphi \to \pi$) in the third quarter the force dipole reduces its rotation. Figure 6.14 c) shows the orientation angle of the fastening point (decompose into the $[-\pi/2;\ \pi/2]$ interval) as a function of its rotation period T. As we can see on figure 6.14 swimmer spends bigger time (about 83% of its period) in the direction of extension ((I) and (III) than in the compression direction (II) and (IV), where it rotates freely with angular velocity $\omega_y = -\dot{\gamma}/2$. So, if we look at the suspension after some time from the beginning of simulations, we will find an anisotropic distribution (see figure 6.15). Most particles will be oriented along extension direction. Figure 6.15 a) shows a view of 100 active particles in the simulation box after long enough time

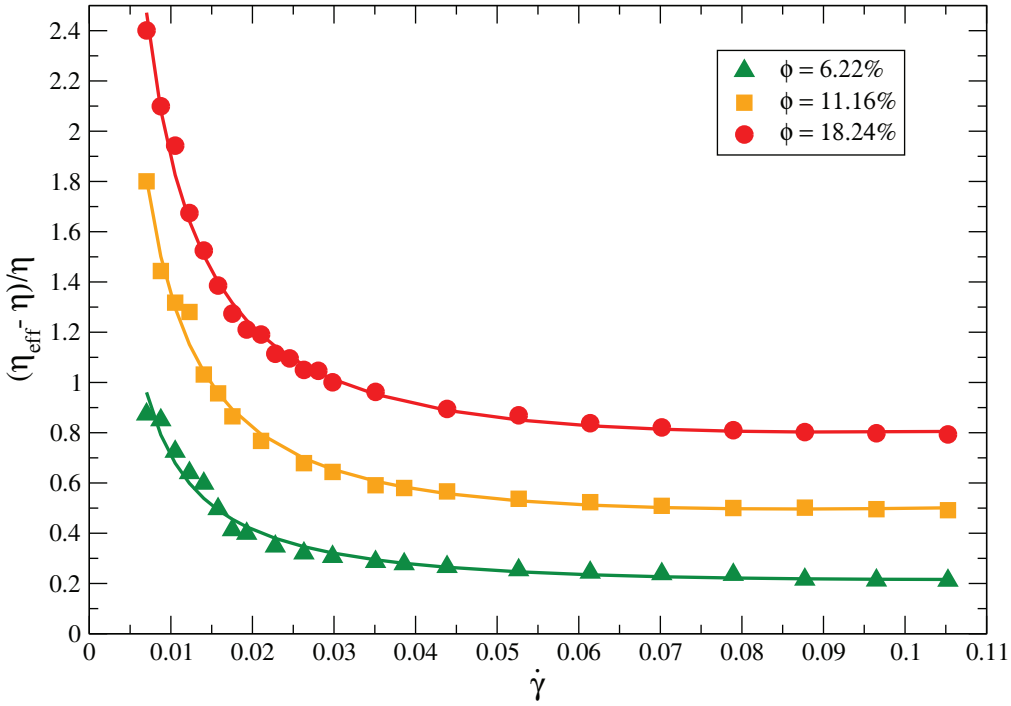

Figure 6.17: The reduced effective viscosity versus shear rate for different values of volume fractions.

from the beginning of simulation (the number of iterations is about 5×10^5) and b-e): $n(\varphi)$ number of particles having the orientation angle in the $[\varphi; \varphi + 10°]$ interval, normalized by the total number of particles N as a function of φ for four different values of N. The similar result was found by Saintillan [102], Haines et al. [106] for bacterial suspension, where they predict an anisotropic distribution and decrease of the effective viscosity in pusher type bacterial suspensions. The main difference between their models and our model is that, we deal with spherical objects and alignment of particles is a result of their swimming features in shear flow and not their shape or a hydrodynamic interaction between particles. In this model a collective effect is not necessary to obtain alignment of particles in the shear flow and it works for a single particle as well (although, hydrodynamic interaction between particles is fully included in our simulations using FPD method). Other details of the simulations are similar to the one used in previous models.

Figure 6.16 shows the reduced effective viscosity of active particle suspension calcu-

lated using the present model for different ϕ. The numerical results for active swimmer suspensions (red full circles with line) are compared to the experimental measurements (magenta circles with error bars for swimming cells and green squares with error bars for dead cells). The model also shows a shear thinning behavior of active particles suspension. Indeed, for a fixed force dipole, if the shear rate is increased, particles spend less time in (I) and (III) quarters (figure 6.14 b) where the force dipole is applied and behave as passive particles. Figure 6.17 shows simulated reduced effective viscosity as a function of $\dot{\gamma}$ for different volume fractions. Numerical points are fitted by a power series.

The present model (which is force free and torque free) successfully explains our experimental observations: the increase of the effective viscosity in swimming cell suspensions; the shear thinning effect and the resistance of an live swimmer to the shear imposed tumbling (see section 6.3). However, additional experiments are needed to study individual or collective dynamics of live *Chlamydomonas* under a shear flow and especially to analyze the effect of a shear flow on the flagella .

6.7.1 The effective viscosity of pusher type swimmers suspensions

We use this model which converges in anisotropic distribution of force dipoles for a pusher type swimmers suspension. For this purpose, we simply flip the sign of the force dipoles. The particle still spends longer time in the extension direction than in compression direction, because when the fastening point passes to the vertical axis ($\varphi = \pi/2$) in the first quarter and ($\varphi = 3/2\pi$) in the third quarter the force dipole exerts a torque on the body and reduces its rotation. The model for pusher type swimmers does not corresponds explicitly to any specific swimmers, but we calculate the effective viscosity using this model and found a decrease of the effective viscosity (even less than the solvent viscosity). The results are in qualitative agreement with experimental measurements of the effective viscosity of the bacterial suspension [10]. Figure 6.18 shows our numerical results concerning the reduced effective viscosity as a function of ϕ calculated for a pusher type swimmer suspension (full red circles). The solid red line presents the parabolic fitting of the simulations results. The results for pusher type swimmer suspensions are compared with Kreiger & Dougherty's law (dashed magenta line) for passive suspensions [78]. The obtained result is reminiscent

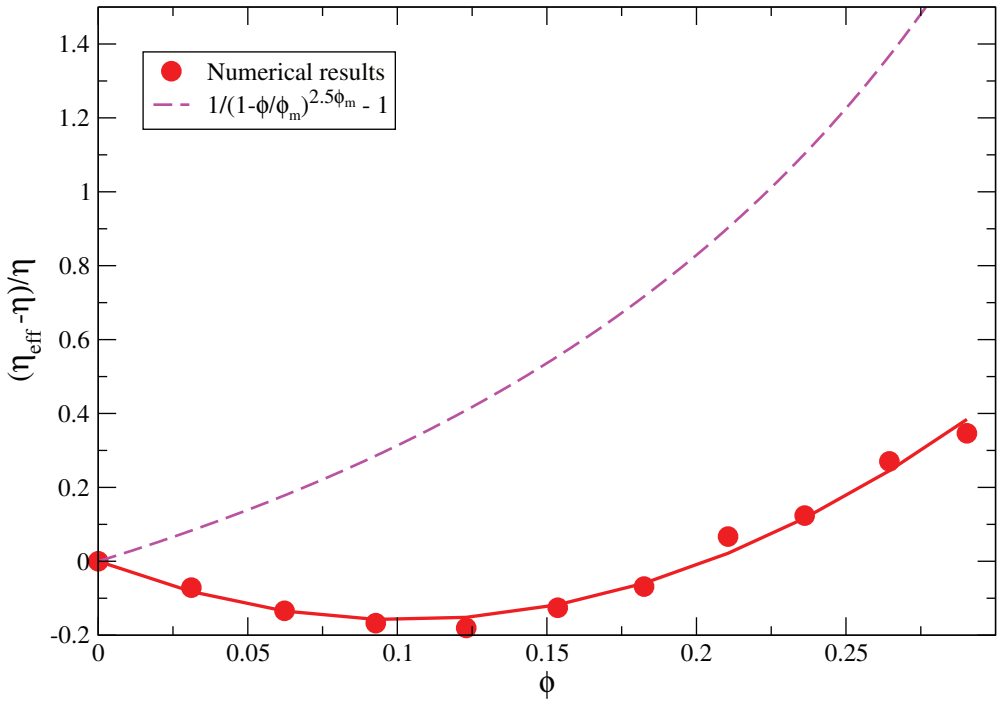

Figure 6.18: The reduced effective viscosity of a pusher type swimmers suspension with anisotropic distribution of force dipoles versus volume fraction.

to $\eta_{eff}(\phi)$ of Sokolov and Aranson experimental results [10].

6.8 Conclusion

In this chapter, we developed different models to numerically study the rheology of micro-swimmer suspensions. Namely, the effective viscosity of *Chlamydomonas* suspension. We begin with a general review of micro-swimmers in section 6.3 and discussed the low Reynolds number constrains formulated in the scallop theorem (subsection 6.2.1). In section 6.4, we briefly present some results of our experiments on *Chlamydomonas* suspensions, namely, the effective viscosity of swimming and dead cells for different volume fraction and shear rates, we also picture sequences of swimming cells and dead cells in the shear flow. In the next section (6.4), we present models and the results of numerical simulations, where micro-swimmers was simulated by spherical body with an isotropically distributed force dipoles. The model shows no noticeable contribution of

activity of swimmers on the rheological properties of the suspension. Then, we forced particles to reduce their shear imposed rotation by applying an external torque and found a quantitative agreement with the experimentally measured rheological properties of *Chlamydomonas* suspensions (section 6.5). In next section (6.6), we considered the effects of flagella by modeling the *Chlamydomonas* with three beads and found good agreement with the experimental measurements. However, the model did not produce a self-motility of particles. Finally, in section 6.7 by taking into account the swimming features of *Chlamydomonas* in the shear flow, we proposed a model which converges to anisotropic distribution of force dipole and incorporates all experimentally observed phenomena: increase of the effective viscosity in active *Chlamydomonas* suspensions; the shear thinning behavior and resistance of swimming cells to the tumbling motion imposed by the shear flow. We applied the model also on a pusher type swimmers suspensions and found a decrease of the effective viscosity which is in qualitative agreement with experimental observations [10].

In this chapter several models have been investigated which takes into account the different aspects of *Chlamydomonas* suspensions. However, the last model is perhaps closest to the real studying system.

Chapter 7

Conclusions and future prospects

7.1 Conclusions and major outcomes

In this section, we summarize our main results and contributions to the study of active fluids.

Contribution to the FPD method
In chapter 3 the Fluid Particle Dynamics numerical method was introduced. We made some improvement and extension to the FPD method. Namely, the method was adapted for any ellipsoidal shape of the suspended particles; the Successive Over Relaxation (SOR) method for solving the Poisson's equation has been optimized. In order to impose a shear flow, we can apply a shear rate or a shear stress. The periodic boundary conditions have been extended from one direction to two directions (in three dimensional simulations). We also presented several problems solved using FPD method compared to well known analytical results.

Effect of finite geometry on the dynamics of a sheared suspension
We investigated the effect of walls on the rotation of a spherical particle in a shear flow in two cases: when the particle is confined in the middle of two walls (moving in opposite direction) and when the particle is close to a single wall. We found that in both cases the angular velocity of the rotating spherical particle is smaller than the one imposed by the shear flow ($-\dot{\gamma}/2$, where $\dot{\gamma}$ is the shear rate). The effect is simple and

can be easily observed in microfluidic or biological applications. However, so far there are only a few works dealing with these effects. In addition, when a particle is confined so that rigid contact appears between the particle and the walls the angular velocity of particle should be increased up to $-\dot{\gamma}$. Previous simulations and calculations cannot reach the rigid contacts between particles and walls and predict only the decrease of the angular velocity in a confined geometry [55, 56, 18]. Our numerical results are in agreement with the previous results and seem to be able incorporate partially the rigid contacts when walls are very close.

We also found that in vicinity of a single wall the translational velocity of a particle is modified so that the difference between the velocity of the particle and the velocity of the wall is decreased.

Suspensions with a tunable effective viscosity

We numerically investigated sheared suspensions of non-colloidal spherical particles on which a torque is applied and show that (by changing the particles rotation) the effective viscosity of the suspension can be strongly modified. We introduce a dimensionless number Θ (representing the average relative angular velocity of the particles divided by the vorticity of the fluid generated by the shear flow) and show that the contribution of the particles to the effective viscosity can be suppressed for a given and unique value of Θ independently of the volume fraction ϕ. Based on our numerical simulations, we proposed the semi-empirical formula valid up to $\phi = 40\%$ concentration for the effective viscosity:

$$\Delta\eta_{eff}(\phi,\Theta) = \Delta\eta^0_{eff}(\phi)\left(1+\frac{3}{5}\Theta\right),$$

where $\Delta\eta_{eff}(\phi,\Theta)$ and $\Delta\eta^0_{eff}(\phi)$ are the reduced effective viscosity with and without an external torque, respectively. This expression is exact for dilute concentrations (when $\phi \ll 1$, a modified intrinsic viscosity for dilute suspension derived by Brenner [14] can be recovered) and empirical for more concentrated regime. We proposed also empirical second Faxén law [73] extended to semi dilute and more concentrated regimes.

Effective viscosity of micro swimmer suspensions

In chapter 6, we conducted numerical investigation of puller type micro swimmer suspensions. We explored several models. The models and numerical simulations was

encouraged by their consistency with experiments made on *Chlamydomonas* suspensions by S. Rafaï et al. [9].

The first model with isotropically distributed force dipoles show no contribution to the effective viscosity of suspensions. In the next model, the particles in the suspension are forced to maintain their initial orientation in the shear flow by using an external torque. This model incorporates the experimentally observed features of *Chlamydomonas* suspensions. However, we did not found an experimental evidence that an external torque is applied to the swimmers, since here gravity certainly plays no role. Then, we considered the effect of flagella (elongation of *Chlamydomonas* due to the presence of flagella) by constructing object with a three bead chain and found again an increased effective viscosity. The shear thinning behavior is also similar to the one obtained experimentally. The shortcoming of the model is the lack of motility of objects in the suspension. Finally, we proposed a model where the swimming features of *Chlamydomonas* in the shear flow rae taken into account and converge to an anisotropic distribution of swimmers into the shear flow. Some suppositions made in the model still need future experimental support. However, the model produces an increase of the effective viscosity in quantitative agreement with the experimental observation and also shear thinning behavior due to the resistance of swimmers to the tumbling motion imposed by the shear flow. The last model also produces reduced effective viscosity (even less then solvent viscosity) for a pusher type suspension which is also reminiscent to another experimental work [10].

7.2 Perspectives

In this work, we introduced the FPD method and applied it to specific problems. However, there are many areas for future research. In this section some of these are summarized as follows:

Biological active systems:

- Simulations of explicitly pusher type suspensions (bacterial suspension or spermatozoa suspension).

- Mechanics of biological locomotion of different types of swimmers at small length scale with modeling flagella as a bead chains.
- Diffusion and spatial correlation in different types of micro swimmer suspensions.
- The coupling of the flow and swimmers sensitive to gradients (taxis like phototaxis or chemotaxis).

Passive systems in various flows:

- Dynamics and rheology of suspension of ellipsoidal particles.
- Characterization, ordering and phase transition in concentrated suspension under an external field.
- Study dynamics and time-reversibility of Stokes flow for chains of beads in a shear flow or in a Poiseuille flow.

Combination of passive and active systems:

- A single sedimenting passive sphere (the probe) moving through an active suspension of micro-swimmers. The interaction between the passive sphere with the active medium could give a very interesting information concerning micro-rheology of the suspension. Some experiments are also planned in our team concerning this system.

We hope that the present work will pave the way for these future projects.

Chapter 8

Conclusions et perspectives

8.1 Conclusions et principaux résultats

Dans cette section, nous résumons nos principaux résultats et les contributions à l'étude des fluides actifs.

Contributions à la méthode FPD
Dans le chapitre 3, la méthode numérique de la Dynamique des Particules Fluides (FPD) a été introduite. Nous avons fait quelques améliorations et l'extension de la méthode. A savoir, la méthode a été adaptée pour toute forme ellipsoïdale des particules en suspension; la methode de sur-relaxation successives (SOR) a été optimisée et nous a permis de résoudre l'équation de Poisson concernant le calcul de la pression avec plus de rapidité. Dans le but d'imposer un flux de cisaillement, on peut appliquer un taux de cisaillement ou une contrainte de cisaillement. Les conditions aux limites périodiques ont été étendues aux deux directions de l'espace parallèles aux parois. Nous avons également testé plusieurs problèmes connus, solubles analytiquement, en utilisant la méthode FPD et avons comparé nos résultats numériques avec les résultats analytiques.

Effet de la géométrie finie sur la dynamique d'une suspension cisaillée
Nous avons étudié l'effet de la rotation d'une particule sphérique dans un écoulement de cisaillement dans deux cas: lorsque la particule est confinée dans le milieu entre deux parois (se déplaçant en sens inverse) et lorsque la particule est proche d'une seule paroi.

Nous avons constaté que dans les deux cas, la vitesse angulaire de rotation de la particule sphérique est plus petit que celui imposé par le cisaillement ($-\dot{\gamma}/2$, où $\dot{\gamma}$ est le taux de cisaillement). L'effet est simple et peut facilement être observé dans de nombreuses applications microfluidiques ou biologiques. Cependant, jusqu'ici il n'y a que peu de travaux traitant de ces effets. En outre, quand une particule est confinée mais que des contacts rigides apparaissent entre les particules et les parois, alors la vitesse angulaire de la particule est augmentée jusqu'à $-\dot{\gamma}$. Des simulations et des calculs précédents ne peuvent pas atteindre le contact rigide entre des particules et des murs et ne prévoient que la diminution de la vitesse angulaire dans une géométrie confinée [55, 56, 18]. Nos résultats numériques sont en accord avec les résultats précédents et semble pouvoir intégrer partiellement le contact rigide quand les parois sont très proches.

Nous avons également constaté que dans le voisinage d'une paroi unique, la vitesse de translation d'une particule est modifiée de sorte que la différence entre la vitesse de la particule et la vitesse de la paroi diminue.

Suspensions avec une viscosité effective ajustable

Nous avons étudiés numériquement des suspensions cisaillées de particules sphériques non-colloïdales sur lequel un couple est appliqué. Nous avons montré qu'en changeant la vitesse de rotation des particules grâce au couple externe, la viscosité effective de la suspension peut être fortement modifiée. Nous introduisons un nombre sans dimension Θ (représentant la vitesse relative moyenne angulaire des particules divisée par la vorticité du fluide générée par le cisaillement). Nous avons montré que la contribution des particules à la viscosité effective peut être supprimée pour une valeur unique de Θ indépendamment de la fraction volumique ϕ. A partir des résultats de nos simulations numériques, nous avons proposé la formule empirique de la viscosité effective en fonction de Θ et valable jusqu'à $\phi = 40\%$:

$$\Delta\eta_{eff}(\phi, \Theta) = \Delta\eta^0_{eff}(\phi)\left(1 + \frac{3}{5}\Theta\right),$$

où $\Delta\eta_{eff}(\phi, \Theta)$ et $\Delta\eta^0_{eff}(\phi)$ sont respectivement la viscosité effective avec et sans un couple externe. Cette expression est exacte en régime dilué et empirique pour les régimes plus concentrés (lorsque $\phi \ll 1$ (régime dilué), la viscosité intrinsèque dérivée par Brenner [14] peut être retrouvée). Nous avons également proposé une seconde

loi de Faxèn [73] empirique et étendue aux régimes semi-diluées et aux régimes plus concentrés.

Viscosité effective des suspensions de micro-nageurs

Au chapitre 6, nous avons étudié numériquement des suspensions de micro-nageurs de type puller. Nous avons exploré plusieurs modèles. Les modèles et les simulations numériques sont encouragées par leur cohérence avec les expériences faites sur des suspensions de *Chlamydomonas* par S. Rafaï et al. [9].

Le premier modèle avec des forces dipolaires distribuées isotropiquement ne montre pas de contribution à la viscosité effective des suspensions. Le modèle suivant, où les particules en suspension sont contraintes de maintenir leur orientation initiale dans le cisaillement (comme dans le chapitre précédent) en exerçant un couple artificiel externe. Cependant, nous n'avons pas trouvé de preuve expérimentale qu'un couple externe soit appliqué aux nageurs, car ici la pesanteur ne joue certainement aucun rôle. Ensuite, nous avons examiné l'effet de drag sur les flagelles (allongement de *Chlamydomonas* due à la présence de flagelles) en construisant des objets à trois sphères. Ce modèle permet également d'augmenter la viscosité, il permet aussi de retrouver le comportement rhéofluidifiant similaire à celui obtenu expérimentalement. L'inconvénient de ce modèle est l'absence de mobilité des objets dans la suspension. Enfin, nous avons proposé un modèle où les caractéristiques de la nage des *Chlamydomonas* dans le cisaillement ont été prises en compte et converge vers une distribution anisotrope des nageurs dans l'écoulement de cisaillement. Certaines suppositions faites dans le modèle ont encore besoin de confirmations expérimentales. Cependant, le modèle produit une augmentation de la viscosité effective en accord quantitatif avec les observations expérimentales. Il reproduit également le comportement sous cisaillement des nageurs qui ont un mouvement de tumbling ralenti. Ce dernier modèle produit aussi une viscosité pour la suspension même inférieure à la viscosité du solvant dans le cas d'une suspension de type pusher qui est également qualitativement proche d'un autre travail expérimental [10].

8.2 Perspectives

Dans ce travail, nous avons introduit la méthode FPD et nous l'avons appliquée à des

problèmes spécifiques. Cependant, de nombreux domaines de recherches peuvent encore être explorés dans un futur proche. Dressons en une liste succinte:

Systèmes biologiques actifs:

- Simulation de suspensions de type pushers (suspensions bactériennes ou suspension de spermatozoïdes).
- Mécanique de la locomotion biologique des différents types de nageurs à l'échelle microscopique avec des flagelles modélisés à l'aide d'une chaîne de perles.
- Diffusion et corrélation spatiale des nageurs dans la suspension.
- Le couplage entre un écoulement et des nageurs sensibles aux gradients (tactisme, comme le phototactisme ou le chimiotactisme).

Les systèmes passifs dans les différents écoulements:

- Dynamique et rhéologie de suspensions de particules ellipsoïdales.
- Charactérisation d'auto-organisation et de transition de phase en suspension concentrée sous un champ externe.
- Dynamique de chaînes de perles dans des écoulement de Stokes (cisaillement de Couette ou écoulement de Poiseuille).

Combinaison de systèmes passifs et actifs:

- Une seule sphère passive en sédimentation (constituant la sonde) se déplaçant dans une suspension active de micro-nageurs. L'interaction entre la sphère passive avec le milieu actif pourrait donner une information très intéressante concernant la micro-rhéologie de la suspension. Des expériences sont également *prévues* dans notre équipe concernant ce système.

Nous espérons que le présent travail permettra d'ouvrir la voie à ces futurs projets.

Bibliography

[1] Y. Hatwalne, S. Ramaswamy, M. Rao, and R. A. Simha, "Rheology of active-particle suspensions," *Phys. Rev. Lett.*, vol. 92, p. 118101, Mar 2004.

[2] G. S. Beavers and D. D. Joseph, "Novel weissenberg effects," *J. Fluid Mech.*, vol. 81, pp. 265–272, 1977.

[3] T. J. Pedley, *The Fluid Mechanics of Large Blood Vessels*. Cambridge University Press, 2008.

[4] H. A. Barnes, "Shear thickening ("dilatancy") in suspensions of nonaggregating solid particles dispersed in newtonian liquids," *J. Rheol.*, vol. 33, p. 329, 1989.

[5] D. J. Evans and G. P. Morriss, "Shear thickening and turbulence in simple fluids," *Phys. Rev. Lett.*, vol. 56, pp. 2172–2175, May 1986.

[6] E. Lauga and T. R. Powers, "The hydrodynamics of swimming microorganisms," *Rep. Prog. Phys.*, vol. 72, p. 096601, 2009.

[7] E. M. Purcell, "Life at low reynolds number," *Am. J. Phys.*, vol. 45, p. 3, 1977.

[8] E. Lauga, "Life around the scallop theorem," *Soft Matter*, vol. 7, pp. 3060–3065, 2011.

[9] S. Rafaï, L. Jibuti, and P. Peyla, "Effective viscosity of microswimmer suspensions," *Phys. Rev. Lett.*, vol. 104, p. 098102, Mar 2010.

[10] A. Sokolov and I. S. Aranson, "Reduction of viscosity in suspension of swimming bacteria," *Phys. Rev. Lett.*, vol. 103, p. 148101, Sep 2009.

[11] K. P. Tana, R. Stanway, and W. A. Bullough, "Dynamic velocity response of an electro-rheological (er) clutch for robotic applications mechanics of advanced materials and structures," *Mech. Adv. Mater. Struct.*, vol. 13, pp. 1–12, 2006.

[12] S. Lima, S.-M. Parka, and K.-I. Kim, "Ai vibration control of high-speed rotor systems using electrorheological fluid," *J. Sound Vib.*, vol. 284, pp. 685–703, 2005.

[13] S. A. Phani and K. Venkatraman, "Damping characteristics of electro-rheological fluid sandwich beams," *Acta Mech.*, vol. 180, pp. 195–201, 2005.

[14] H. Brenner, "Rheology of a dilute suspension of dipolar spherical particles in an external field," *J. of Coll. and Interf. Sc.*, vol. 32, pp. 141–158, 1970.

[15] Y. Davit and P. Peyla, "Intriguing viscosity effects in confined suspensions: A numerical study," *Eur. Phys. Lett.*, vol. 83, p. 64001, 2008.

[16] P. Peyla, "Rheology and dynamics of a deformable object in a microfluidic configuration: A numerical study," *Eur. Phys. Lett.*, vol. 80, pp. 34001–p1, 2007.

[17] K. Yeo and M. R. Maxey, "Rheology and ordering transitions of non-brownian suspensions in a confined shear flow: Effects of external torques," *Phys. Rev. E*, vol. 81, p. 062501, Jun 2010.

[18] A. S. Sangani, A. Acrivos, and P. Peyla, "Roles of particle-wall and particle-particle interactions in highly confined suspensions of spherical particles being sheared at low reynolds numbers," *Phys. Fluids*, vol. 23, p. 083302, 2011.

[19] M. D. Carbajal-Tinoco, F. Castro-Román, and J. L. Arauz-Lara, "Static properties of confined colloidal suspensions," *Phys. Rev. E*, vol. 53, pp. 3745–3749, Apr 1996.

[20] I. Pagonabarraga, M. H. J. Hagen, C. P. Lowe, and D. Frenkel, "Short-time dynamics of colloidal suspensions in confined geometries," *Phys. Rev. E*, vol. 59, pp. 4458–4469, Apr 1999.

[21] L. Marshall, C. F, Zukoski, and J. W. Goodwin, "Effects of electric fields on the rheology of non-aqueous concentrated," *J. Chem. Soc., Faraday Trans.*, vol. 85, pp. 2785–2795, 1989.

[22] R. E. Rosensweig, R. Kaiser, and G. Miskolczy, "Viscosity of magnetic fluid in a magnetic field," *J. of coll. and Interf. Sc.*, vol. 29, pp. 680–686, 1969.

[23] L. Jibuti, S. Rafaï, and P. Peyla, "Suspensions with a tunable effective viscosity. a numerical study." (to be published).

[24] A. Hasmy, R. Jullien, and R. Botet, "Kinetics of cluster-cluster colloidal aggregation," *Phys. Rev. Lett.*, vol. 75, p. 3777, Nov 1995.

[25] D. A. Weitz and M. Y. Lin, "Dynamic scaling of cluster-mass distributions in kinetic colloid aggregation," *Phys. Rev. Lett.*, vol. 57, pp. 2037–2040, Oct 1986.

[26] D. J. Robinson and J. C. Earnshaw, "Experimental study of colloidal aggregation in two dimensions. ii. kinetic aspects," *Phys. Rev. A*, vol. 46, pp. 2055–2064, Aug 1992.

[27] A. Vincze, A. Agod, J. Kertesz, M. ZrÃnyi, and Z. Horvolgyi, "Aggregation kinetics in two dimensions: Real experiments and computer simulations," *J. Chem. Phys.*, vol. 114, p. 520, 2001.

[28] H. Tanaka, Y. Nishikawa, and T. Koyama, "Network-forming phase separation of colloidal suspensions," *J. Phys. Condens. Matter*, vol. 17, p. 143, 2005.

[29] H. Tanaka, "Viscoelastic model of phase separation," *Phys. Rev. E*, vol. 56, pp. 4451–4462, Oct 1997.

[30] R. P. Sear, "Phase separation in mixtures of colloids and long ideal polymer coils," *Phys. Rev. Lett.*, vol. 86, pp. 4696–4699, May 2001.

[31] P. D. Olmsted and C.-Y. D. Lu, "Phase separation of rigid-rod suspensions in shear flow," *Phys. Rev. E*, vol. 60, pp. 4397–4415, Oct 1999.

[32] T. Koyama, T. Araki, and H. Tanaka, "Fracture phase separation," *Phys. Rev. Lett.*, vol. 102, p. 065701, Feb 2009.

[33] J.-M. Jin, K. Parbhakar, L. H. Dao, and K. H. Lee, "Gel formation by reversible cluster-cluster aggregation," *Phys. Rev. E*, vol. 54, p. 997, Jul 1996.

[34] M. Kroon, W. L. Vos, and G. H. Wegdam, "Structure and formation of a gel of colloidal disks," *Phys. Rev. E*, vol. 57, pp. 1962–1970, Feb 1998.

[35] Y. He, B. J. Ackerson, W. van Megen, S. M. Underwood, and K. Schätzel, "Dynamics of crystallization in hard-sphere suspensions," *Phys. Rev. E*, vol. 54, pp. 5286–5297, Nov 1996.

[36] S. Butler and P. Harrowell, "Kinetics of crystallization in a shearing colloidal suspension," *Phys. Rev. E*, vol. 52, pp. 6424–6430, Dec 1995.

[37] S. I. Henderson and W. van Megen, "Metastability and crystallization in suspensions of mixtures of hard spheres," *Phys. Rev. Lett.*, vol. 80, pp. 877–880, Jan 1998.

[38] J. L. Harland and W. van Megen, "Crystallization kinetics of suspensions of hard colloidal spheres," *Phys. Rev. E*, vol. 55, pp. 3054–3067, Mar 1997.

[39] E. H. A. de Hoog, W. K. Kegel, A. van Blaaderen, and H. N. W. Lekkerkerker, "Direct observation of crystallization and aggregation in a phase-separating colloid-polymer suspension," *Phys. Rev. E*, vol. 64, p. 021407, Jul 2001.

[40] H. Tanaka and T. Araki, "Simulation method of colloidal suspensions with hydrodynamic interactions: Fluid particle dynamics," *Phys. Rev. Lett.*, vol. 85, pp. 1338–1341, Aug 2000.

[41] R. J. Phillips, J. F. Brady, and G. Bossis, "Hydrodynamic transport properties of hard-sphere dispersions. i. suspensions of freely mobile particles," *Phys. Fluids*, vol. 31, p. 3473, 1988.

[42] J. Kromkamp, D. van den Ende, D. Kandhai, R. van der Sman, and R. Boom, "Lattice boltzmann simulation of 2d and 3d non-brownian suspensions in couette flow," *Chem. Eng. Sci.*, vol. 61, pp. 858–873, 2006.

[43] B. Maury, "Numerical analysis of a finite element/volume penalty method," *SIAM J. Numer. Anal.*, vol. 47, pp. 1126–1148, 2009.

[44] S. Succi, *The Lattice Boltzmann Equation For Fluid Dynamics and Beyond*. Oxford University Press, New York, 2001.

[45] S. Osher and R. Fedkiw, *Level Set Methods and Dynamic Implicit Surfaces*. Springer, 2003.

[46] A. J. Chorin, "Numerical solution of the navier-stokes equations," *Math. Comp.*, vol. 22, p. 745, 1968.

[47] R. Temam, "Sur l'approximation de la solution des equations de navier-stokes par la methode des pas fractionnaires," *Arch. Rational Mech. Anal.*, vol. 33, p. 377, 1969.

[48] M. Fortin, R. Peyret, and R. Temam, "Resolution numerique des equations de navier-stokes pour un fluide incompressible," *J. Mecanique*, vol. 10, p. 357, 1971.

[49] F. H. Harlow and J. E. Welch, "Numerical calculation of time-dependent viscous incompressible flow of fluid with free surface," *Phys. Fluids*, vol. 8, pp. 2182–2189, 1965.

[50] P. N. Swarztrauber, R. A. Sweet, and J. C. Adams, *FISHPACK: Efficient FORTRAN Subprograms for the Solution of Elliptic Partial Differential Equations*. National Center for Atmospheric Research, Scientific Computing Division, P.O. Box 3000, Boulder, CO 80307-3000., 1999.

[51] L. D. Landau and E. M. Lifshitz, *FLUID MECHANICS*. Pergamon, 2nd edition, 1987.

[52] D. R. Mikulencak and J. F. Morris, "Stationary shear flow around fixed and free bodies at finite reynolds," *J. Fluid Mech.*, vol. 520, pp. 215–242, 2004.

[53] W. Bartok and S. G. Mason, "Particle motions in sheared suspensions: V. rigid rods and collision doublets of spheres," *J. Colloid Sci.*, vol. 12, pp. 243–262, 1957.

[54] G. B. Jeffery, "The motion of ellipsoidal particles immersed in a viscous fluid," *Proc. R. Soc. London*, vol. 102, pp. 161–179, 1922.

[55] J. Bikard, P. Menard, E. Peuvrel-Disdier, and T. Budtova, "3d numerical simulation of the behaviour of a spherical particle suspended in a newtonian fluid and submitted to a simple shear," *Comp. Mater. Sci.*, vol. 37, pp. 517–525, 2006.

[56] G. D'Avino, G. Cicale, M. Hulsen, F. Greco, and P. Maffettone, "Effects of confinement on the motion of a single sphere in a sheared viscoelastic liquid," *J. Non-Newtonian Fluid Mech.*, vol. 157, pp. 101–107, 2009.

[57] A. J. Goldman, R. G. Cox, and H. Brenner, "Slow viscous motion of a sphere parallel to a plane wall–ii couette flow," *Chem. Eng. Sci.*, vol. 22, pp. 653–660, 1967.

[58] C. L. Darabaner and S. G. Mason, "Particle motions in sheared suspensions xxii: Interactions of rigid spheres (experimental)," *Rheol. Acta*, vol. 6, pp. 273–284, 1967.

[59] C. Pomchaitawarda, I. Manas-Zloczowera, and D. L. Feke, "Investigation of the dispersion of carbon black agglomerates of various sizes in simple-shear flow," *Chem. Eng. Sci.*, vol. 58, pp. 1859–1865, 2003.

[60] R. Taborda, J. Antunes, and F. Marques, "2-d rotation behavior of a rigid ellipse in confined viscous simple shear: numerical experiments using fem," *Tectonophysics*, vol. 379, pp. 127–137, 2004.

[61] F. O. Marques, R. M. Taborda, and J. V. Antunes, "2d rotation of rigid inclusions in confined bulk simple shear flow: a numerical study," *Journal of Structural Geology*, vol. 27, pp. 2171–2180, 2005.

[62] S. W. Horwatt, Manas-Zloczower, and D. Feke, "Dispersion behavior of heterogeneous agglomerates at supercritical stresses," *Chem. Eng. Sci.*, vol. 47, pp. 1849–1855, 1992.

[63] B. Kaoui, J. Harting, and C. Misbah, "Two-dimensional vesicle dynamics under shear flow: Effect of confinement," *Phys. Rev. E*, vol. 83, p. 066319, Jun 2011.

[64] W. B. Russel, A. Saville, and W. R. Schowalter, "Colloidal dispersions," *Cambridge University Press*, vol. 525, p. 70, 1989.

[65] E. Lemaire, L. Lobry, N. Pannacci, and F. Peters, "Viscosity of an electro-rheological suspension with internal rotations," *J. Rheol.*, vol. 52, pp. 769–785, 2008.

[66] J. C. Bacri, R. Perzynski, M. I. Shliomis, and G. I. Burde, ""negative-viscosity" effect in a magnetic fluid," *Phys. Rev. Lett.*, vol. 75, pp. 2128–2131, Sep 1995.

[67] T. Ishikawa and T. J. Pedley, "The rheology of a semi-dilute suspension of swmming model micro-organisms," *J. Fluid Mech.*, vol. 588, pp. 399–435, 2007.

[68] M. Marchioro, M. Tanksley, and A. Prosperetti, "Flow of spatially non-uniform suspensions: Part i: Phenomenology," *Int. J. Multiphase Flow*, vol. 26, pp. 783–831, 2000.

[69] M. Marchioro, M. Tanksley, W. Wang, and A. Prosperetti, "Flow of spatially non-uniform suspensions: Part ii: Systematic derivation of closure relations," *Int. J. Multiphase Flow*, vol. 27, pp. 237–276, 2001.

[70] W. Wang and A. Prosperetti, "Flow of spatially non-uniform suspensions. part iii: Closure relations for porous media and spinning particles," *Int. J. Multiphase Flow*, vol. 27, pp. 1627–1653, 2001.

[71] K. Ichiki and A. Prosperetti, "Faxen-like relations for a nonuniform suspension," *Phys. of Fluids*, vol. 16, pp. 2483–2496, 2004.

[72] S. Feng, A. L. Graham, J. R. Abbott, and H. Brenner, "Antisymmetric stresses in suspensions: vortex viscosity and energy dissipation," *J. Fluid Mech.*, vol. 563, pp. 97–122, 2006.

[73] J. Happel and H. Brenner, *Low Reynolds Number Hydrodynamics*. Martinus Nijhoff Publishers, The Hague, 1983.

[74] A. Einstein, "Eine neue bestimmung der molekul-dimensionen," *Ann. Phys. (Leipzig)*, vol. 19, pp. 289–306, 1906.

[75] A. Einstein, "Berichtigung zu meiner arbeit: "eine neue bestimmung der molekul-dimensionen"," *Ann. Phys. (Leipzig)*, vol. 34, pp. 591–592, 1911.

[76] G. K. Batchelor and J. T. Green, "The determination of the bulk stress in a suspension of spherical particles to order c2," *J. Fluid Mech.*, vol. 56, pp. 401–427, 1972.

[77] B. Cichocki and B. U. Felderhof, "Short-time diffusion coefficients and high frequency viscosity of dilute suspensions of spherical brownian particles," *J. Chem. Phys.*, vol. 89, pp. 1049–1055, 1988.

[78] I. M. Kreiger and T. J. Dougherty, "A mechanism for non-newtonian flow in suspensions of rigid spheres," *Trans. Soc. Rheol.*, vol. 3, pp. 137–152, 1959.

[79] G. K. Batchelor, "The stress system in a suspension of force-free particles," *J. Fluid Mech.*, vol. 41, pp. 545–570, 1970.

[80] D. W. Condiff and J. S. Dahler, "Fluid mechanical aspects of antisymmetric stress," *The Physics of Fluids*, vol. 7, pp. 842–854, 1964.

[81] D. G. Thomas, "Transport characteristics of suspension: Viii. a note of the viscosity of newtonian suspensions of uniform spherical particles," *J. Colloid Sci.*, vol. 20, pp. 267–277, 1965.

[82] A. Sierou and J. F. Brady, "Rheology and microstructure in concentrated noncolloidal suspensions," *J. Rheol.*, vol. 46, pp. 1031–1057, 2002.

[83] F. Gadala-Maria, *The rheology of concentrated suspensions*. PhD thesis, Stanford University, 1979.

[84] A. J. C. Ladd, "Hydrodynamic transport coefficients of random dispersions of hard spheres," *J. Chem. Phys.*, vol. 93, pp. 3484–3494, 1990.

[85] R. Dreyfus, J. Baudry, M. L. Roper, M. Fermigier, H. A. Stone, and J. Bibette, "Microscopic artificial swimmers," *Nature*, vol. 437, pp. 862–865, 2005.

[86] E. E. Keaveny and M. R. Maxey, "Spiral swimming of an artificial microswimmer," *J. Fluid Mech.*, vol. 598, pp. 293–319, 2008.

[87] J. S. Rathore and N. N. Sharma, "Engineering nanorobots: Chronology of modeling flagellar propulsion," *Journal of Nanotechnology in Engineering and Medicine*, vol. 1, p. 031001, 2010.

[88] F. Y. Ogrin, P. G. Petrov, and C. P. Winlove, "Ferromagnetic microswimmers," *Phys. Rev. Lett.*, vol. 100, p. 218102, May 2008.

[89] C. Brennen and H. Winet, "Fluid mechanics of propulsion by cilia and flagella," *Ann. Rev. Fluid Mech.*, vol. 9, pp. 339–398, 1977.

[90] M. J. Kim and K. S. Breuer, "Use of bacterial carpets to enhance mixing in microfluidic systems," *J. Fluids Eng.*, vol. 129, pp. 319–324, 2007.

[91] C. Dombrowski, L. Cisneros, S. Chatkaew, R. E. Goldstein, and J. O. Kessler, "Self-concentration and large-scale coherence in bacterial dynamics," *Phys. Rev. Lett.*, vol. 93, p. 098103, Aug 2004.

[92] N. Darnton, L. Turner, K. Breuer, and H. C. Berg, "Moving fluid with bacterial carpets," *Biophys. J.*, vol. 86, pp. 1863–1870, 2004.

[93] W. M. Durham, J. O. Kessler, and R. Stocker, "Disruption of vertical motility by shear triggers formation of thin phytoplankton layers," *Science*, vol. 323, p. 5917, 2009.

[94] M. R. Parsek and P. K. Singh, "Bacterial biofilms: An emerging link to disease pathogenesis," *Annu. Rev. Microbiol.*, vol. 57, pp. 677–701, 2003.

[95] G. Soni, B. J. Ali, Y. Hatwalne, and G. Shivashankar, "Single particle tracking of correlated bacterial dynamics," *Biophys. J.*, vol. 84, pp. 2634–2637, 2003.

[96] P. T. Underhill, J. P. Hernandez-Ortiz, and M. D. Graham, "Diffusion and spatial correlations in suspensions of swimming particles," *Phys. Rev. Lett.*, vol. 100, p. 248101, Jun 2008.

[97] G. Miño, T. E. Mallouk, T. Darnige, M. Hoyos, J. Dauchet, J. Dunstan, R. Soto, Y. Wang, A. Rousselet, and E. Clement, "Enhanced diffusion due to active swimmers at a solid surface," *Phys. Rev. Lett.*, vol. 106, p. 048102, Jan 2011.

[98] M. Garcia, S. Berti, P. Peyla, and S. Rafaï, "Random walk of a swimmer in a low-reynolds-number medium," *Phys. Rev. E*, vol. 83, p. 035301, Mar 2011.

[99] X.-L. Wu and A. Libchaber, "Particle diffusion in a quasi-two-dimensional bacterial bath," *Phys. Rev. Lett.*, vol. 84, pp. 3017–3020, Mar 2000.

[100] R. V. Vincent and N. A. Hill, "Bioconvection in a suspension of phototactic algae," *J. Fluid Mech.*, vol. 327, pp. 343–371, 1996.

[101] C. Torney and Z. Neufeld, "Phototactic clustering of swimming microorganisms in a turbulent velocity field," *Phys. Rev. Lett.*, vol. 101, p. 078105, Aug 2008.

[102] D. Saintillan, "Extensional rheology of active suspensions," *Phys. Rev. E*, vol. 81, p. 056307, May 2010.

[103] B. M. Haines, *Effective Viscosity of Dilute Bacterial Suspensions*. PhD thesis, The Pennsylvania State University, 2011.

[104] S. Heidenreich, S. Hess, and S. H. L. Klapp, "Nonlinear rheology of active particle suspensions: Insights from an analytical approach," *Phys. Rev. E*, vol. 83, p. 011907, Jan 2011.

[105] Z. Cui, "Weakly sheared active suspensions: Hydrodynamics, stability, and rheology," *Phys. Rev. E*, vol. 83, p. 031911, Mar 2011.

[106] B. M. Haines, I. S. Aranson, L. Berlyand, and D. A. Karpeev, "Effective viscosity of dilute bacterial suspensions: a two-dimensional model," *Phys. Biol.*, vol. 5, p. 046003, 2008.

[107] D. Stern, E. H. Harris, and G. Witman, *The Chlamydomonas Sourcebook*. Academic Press: second edition, 2008.

[108] E. Lauga and D. Bartolo, "No many-scallop theorem: Collective locomotion of reciprocal swimmers," *Phys. Rev. E*, vol. 78, p. 030901, Sep 2008.

[109] K. Drescher, R. E. Goldstein, N. Michel, M. Polin, and I. Tuval, "Direct measurement of the flow field around swimming microorganisms," *Phys. Rev. Lett.*, vol. 105, p. 168101, Oct 2010.